Measurement and modelling of the stiffness, deformation and constitutive behaviour of biomedical textile implants

by

Chuzhen Shan

A thesis submitted in partial fulfillment of the requirements for the

Master's degree in engineering

Department of Mechanical Engineering

Faculty of Engineering

University of Ottawa

© Chuzhen Shan, Ottawa, Canada, 2020

Acknowledgements

I would like to thank my supervisor, Dr. François Robitaille for his patient guidance for the past two years. I appreciate not only the knowledge he passed to me, but also his encouragement which gave me great confidence to overcome difficulties. His passion for his job moved me and triggered my interest in this project. I would like to thank my colleagues Phillip and Jacob for providing help in lab and putting up with my questions.

To my friend Fabian, the days we spent together were unforgettable. Thank you for your humor and optimism that brought me much pleasure.

Lastly, a great thank you to my parents and grandparents. Without their support and understanding, I would never be here and realize the value of life.

Abstract

Composite materials and technical textiles are increasingly used in biomedical applications. In the past few decades, research on artificial biomedical scaffolds manufactured from technical textiles have attracted much attention. Among many types of technical textiles, those made from PET fibres are most commonly used to repair knee ligaments due to their advantages including biocompatibility, biodegradability and suitable mechanical properties. The woven structure of a textile influences its the mechanical properties in many aspects, such as its tensile behaviour and shear behaviour, both of which being the main deformation modes that knee ligaments must sustain within human bodies. The aim of this thesis is to analyze the tensile and shear behaviours of three types of PET implantable artificial textile ligaments provided by manufacturer Neoligaments®.

The first part of the work consists in applying tensile and shear loads on the three types of artificial textile ligaments and deriving the value of tensile stiffness and shear stiffness. Then, the experimental results were analyzed, and they were compared with the behaviour of real knee ligaments in order to assess whether the artificial textile ligaments provide adequate behaviour and stiffness.

The second part of the work introduces early work done towards modelling the mechanical behaviour of the artificial textile ligaments. Finite element models were constructed from geometric models of the textiles built using textile modelling software TexGen. After applying

tensile loads in ANSYS, stresses, strains and deformations in the models were analyzed. Based on the results, tensile stiffness of the models could be calculated. Although some limitations to the models lead to differences between these results and experimental values, the work enabled the identification of features of the models to be maintained in future work, and of features to be improved, towards the analysis of the mechanical properties of technical textiles and other non-linear, non-rigid structures.

Keywords: Technical textiles; Artificial textile ligaments; Tensile testing; Shear testing; Stiffness; Finite element analysis

Table of contents

List of figures

List of tables

Nomenclature

A	Cross-sectional area of fibres that sustain loads (cm^2)
A'	Cross-section area of one single yarn
E	Elastic stiffness (MPa)
F	Load (N)
Fn	Normalized shear forces
Fs	Shear force
L	Original length of sample (mm)
L'	Coupon length (mm)
L_{fabric}	Width of square central section of fabric
L_{frame}	Length of a pivoted link
m	Mass of coupon (g)
m_{yarn}	Mass of a single yarn (g)
P_{warp}	Proportion of warp yarns within a coupon
V	Volume of all warp fibres in coupon (cm^3)
V_{fibre}	Volume of the fibres within a single yarn (m^3)
V_{yarn}	Volume of a single yarn (m^3)
$vf_{fibre-sample}$	Volume fraction of fibres in an original sample
$vf_{fibre-yarn}$	Volume fraction of fibres in a single yarn
$vf_{yarn-sample}$	Volume fraction of yarns in an original sample
W_{fabric}	Width of coupon

γ	Shear angle (°)
ΔL	Extension of sample (mm)
Δl	Distance between initial and final positions of a corner
$\mathcal{E}$	Strain
θ	Half angle between neighbouring pivoted links of shear apparatus after deformation
ρ	Density of PET fibres (g/cm^3)
σ	Stress (MPa)

Abbreviations

ACL	anterior cruciate ligament
ALL	anterolateral ligament
CCL	collagen–chitosan scaffolds
CS	chondroitin sulfate
GAG	sugar ammonia glycan
HMSC	human mesenchymal stem cells
LCL	lateral collateral ligament
MCL	medial collateral ligament
MPFL	medial patellofemoral ligament
PCL	polycaprolactone
PCL	posterior cruciate ligament
PET	polyethylene terephthalate
PGA	polyglycolic acid
PLA	polylactic acid
PLGA	PGA/PLA copolymer
PT	patellar tendon
SBBS	silk-based biomaterials

Chapter 1 - Introduction

1.1 Background

Composite materials have been used increasingly in biomedical applications in recent decades, where both biochemical properties and mechanical properties of selected materials are favourable and important. As scaffolds implanted in human bodies, the materials must have the following properties: biocompatibility, which means that the implants would not cause immune rejection; biodegradability, which means that the implants can be degraded by cells and body fluids gradually and suitable mechanical properties which means that the scaffolds can sustain certain loads and support broken tissues around them. Based on these three points, textile structures and composite materials have often arisen as the most suitable choices, and they have met with much successes. Textile structures and composite materials used as implants are generally divided into two groups, based on material sources: synthetic high molecular weight polymers and natural biomaterials. PET fibres as one of the synthetic high molecular weight polymers, not only meet the above requirements, but they also have advantage in high strengths, stiffnesses and excellent cell adhesion, which make them highly suitable for use as ligaments and tendons [1, 2].

Textiles structures are commonly used as biomedical implants and scaffolds. The mechanical properties of textiles made from the same types of materials can be adjusted easily by changing the textile structures and weave patterns in order to cater to different needs. Apart from this,

openings in textile structures allow cell and nutriment transportation, which promotes cell ingrowth and tissue healing. Woven textiles can sustain relative high in-plane loads such as tensile loads and in-plane shear loads, both of which are primary in-service deformation modes of knee ligaments in human bodies. Studies of the mechanical properties of real knee ligaments are sufficiently detailed especially regarding their tensile behaviour. Some scientists also manufactured artificial scaffolds to replace ligaments and tendons based on braided or knitted fabrics, with an emphasis on improving their mechanical properties by adjusting patterns or adding coatings of other materials [3, 4]. However, published research work describing tensile and shear behaviour of woven textiles used as knee ligament replacements are very limited; very few researches described the shear behaviour of knee ligament scaffolds and no publications discussing the topic could be found.

Finite element analysis (FEA) is a wildly used way to replicate and analyze physical models. The technique was used initially in aerospace, mainly to solve linear structural problems. With the development of technology, linear theory has been found to be wanting in terms of meeting requirements for the design of structures subjected to large strains and displacements. When analyzing composite materials such as reinforced rubbers or technical textiles for example, non-linear behaviours such as creep and relaxation should be taken into consideration. Besides, large displacements that occur in a physical model are also considered as non-linear cases. More recently, finite element analysis was also used to replicate and analyze non-linear behaviours. When analyzing such problems the material properties and constitutive behavior of each element in a model are of great importance.

This thesis explores the mechanical behaviour of artificial implantable textile ligaments manufactured by Neoligaments®, a company designing and manufacturing such implantable structures for the sports medicine and orthopaedic markets. The main goal of the thesis is to quantify the tensile and shear stiffness of three types of PET textiles that used as biomedical scaffolds for knee ligaments. The thesis also explore the FEA analysis of the tensile behaviour of the same types of structures.

1.2 Objectives

The main goals of this thesis were to measure the tensile and in-plane shear properties of three types of biomedical PET textiles and compare experimental results with simulation results. Specific objectives are listed below:

- Measuring the tensile and in-plane shear properties of the three kinds of samples;
- Analysing the stress-strain curves and calculating stiffness values under tensile and in-plane shear loads;
- Determining whether the three samples show mechanical behaviour that is generally comparable with that of real knee ligaments;
- Creating geometrics models of the samples in TexGen;
- Applying loads on the geometric models and analysing stresses, strains and deformations obtained through finite element analysis;
- Comparing the results of the models to experimental results in order to assess model characteristics to maintain, and characteristics to be developed in future work.

1.3 Organization of the thesis

This thesis is organised in 6 chapters. Chapter 1 provides the research background and explains the research objectives and contributions of this work.

Chapter 2 presents a through literature review that is mainly divided into four parts. Firstly, the types of textiles, their features and their advantages and disadvantages are introduced in detail. Secondly, the types of textile fibres are introduced. Thirdly, some human organs and tissues which can be replaced by textile scaffolds are detailed from the aspects of components and mechanical properties. The last part introduces some advanced successful surgeries to replace animal and human tissues with different types of textiles.

Chapter 3 describe the experimental equipment, sample preparation and experimental methods. The structure of the samples and fixtures used are detailed, along with the test methods.

Chapter 4 presents the analysis of tensile test results. By converting load-extension curves into stress-strain curves, values of the tensile stiffness of the three samples at different stress levels are calculated and compared.

Chapter 5 presents the analysis of shear test results. The load-extension curves were converted into curves depicting the relationship between normalized shear force and shear angle. Values of shear stiffness of the three samples under different shear loads are also calculated and

compared.

Chapter 6 presents a series of procedures related to the finite element simulations and modeling. The chapter begins with the introduction of textile modeling software TexGen and finite element analysis software ANSYS. Then several cases analysed in ANSYS are detailed including the set of parameters used, along with results. Based on those results, values of the tensile stiffness of the models under different levels of tensile stress were calculated and compared with the experimental results presented in Chapter 4 to investigate the influence of the set of parameters and comment on the accuracy of the models.

1.4 Contributions

The most important contributions of this thesis is the tensile and shear stiffness measured and calculated for three types of biomedical implant samples provided by Neoligaments®. As mentioned previously, research works discussing the tensile and shear behaviour of textile implants are very few in the current scientific literature. This thesis does not only feature measured data, but also transformed experimental results into more intuitional and comparable curves. Tensile and shear stiffness values are calculated and compared with those of real knee ligaments, providing sufficient support for the samples to be used in reality.

Another contribution is the modeling of samples and analysis of tensile behaviour based on finite element analysis. Whilst the geometric modeling of textiles made from solid or continuous yarns is common, there is little work published about the mechanical modeling of textiles made from solid or continuous yarns of non-linear materials. This thesis presents an attempt to model and analyze the non-linear tensile behaviour of textiles using models that feature solid or continuous yarns, instead of yarns that are made from discontinuous assemblies of aligned individual fibres. The concept and methods used for replicating non-linear behaviour in these models are detailed. Finally, this work constitutes the first open study where the tensile and shear stiffness of three productions Neoligaments® implantable artificial textile ligaments are probed and simulated using finite element analysis.

Chapter 2 – Literature Review

In this Chapter, textile types, fibre types used in manufacturing biomedical textiles, and biomedical applications of different types of textiles are introduced. The mechanical and biological properties of natural tissues replaced by textile implants and scaffolds are also discussed, especially as applicable to the knee, in order to quantify and compare the general mechanical behaviour the implants and scaffolds should meet.

2.1 Textile types

Different types of textiles can be identified based on differences in yarn interlacing, which influences the mechanical properties of the textiles such as their density, tensile stiffness and shear strength, for example. Three prevalent types of textiles known as weaves, braids, and knits are introduced.

2.1.1 Weaves

Weaving processes are classified as producing either 2D weaves or 3D weaves. A 2D biaxial weave is constructed from two sets of warp and weft yarns which interlace. Figure 2.1 shows three types of 2D biaxial weaves. Unlike conventional biaxial weaves, tri-axial weaves are constructed from three sets of yarns, one directional weft set and two directional warp sets [5]. The three sets of yarns are typically separated by 60˚angles thus tri-axial weave show excellent

resistance to shear, tear and bursting. Different weaving patterns influence diverse characteristics of the woven fabrics, such as their morphology, density, flexibility, porosity and mechanical properties. Woven fabrics offer advantages for many applications. Compared with knitted fabrics, woven structures are more flexible and they can deform more overall. Besides, they typically feature smaller inter-yarn holes than braided fabrics, which enables control over cell penetration and tissue ingrowth [6]. Regular two-dimensional woven structures show better compliance to forces in the through-thickness direction.

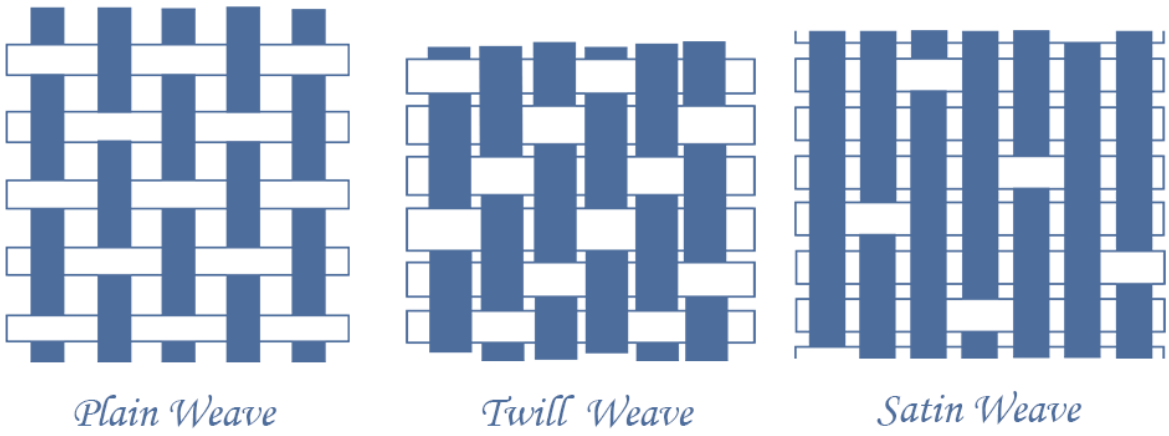

Figure 2.1 Different 2D weaving patterns: plain, twill and satin weave [7]

In the past few decades, 3D woven structures were developed and used as biological scaffolds. Such 3D woven structures are built by connecting 2D structures layer by layer, or by interlocking all layers. 3D woven fabrics perform better in withstanding out-of-plane forces [8, 9, 10]. Moutos *et al*. [11] used chondrocyte-laden agarose gel to reinforce a 3D woven scaffold used as articular cartilage and manufactured by interlacing 2D layers made from PCL fibres, as shown is Figure 2.2. This scaffold was used in cartilage, and performed well.

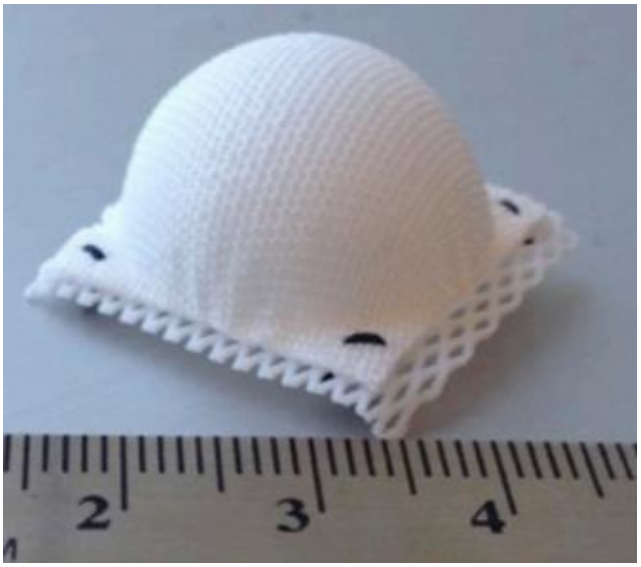

Figure 2.2 Hemispherical-shaped 3D woven PCL scaffold [11]

2.1.2 Braids

Braiding is a textile manufacturing process, where textiles are formed by intertwining three or more yarns as shown in Figure 2.3. 2D braiding allows the manufacturing of general tubular shapes. The interlacing patterns of some 2D braids are identical to those of some 2D weaves. For example, a diamond braid is equivalent to a plain weave, and a tri-axial braid is equivalent to a tri-axial weave. According to research [12, 13], the most significant advantage of braids compared with other textile types is that braided structures can sustain higher axial and radial loads [6]. Because of their unique architecture and excellent radial strength, scaffolds made by braiding are widely used as connective tissues, blood vessels and nerve conduits amongst other applications. However, the small size of inter-yarn gaps and high density of yarns limit cell penetration and infiltration into the scaffolds. To solve these problems, cell-laden fibers are usually braided into scaffolds, resulting in scaffolds integrated with cells [8, 10].

3D braided textiles feature yarns that run through the braid in all three directions, formed by intertwining three orthogonal sets of yarns [14]. Compared with 2D braids, 3D braids offer better strength, better stiffness and better specific properties relative to their mass. Figure 2.4 shows an application of a 3D braided textile used as implant scaffolds for knee ligaments.

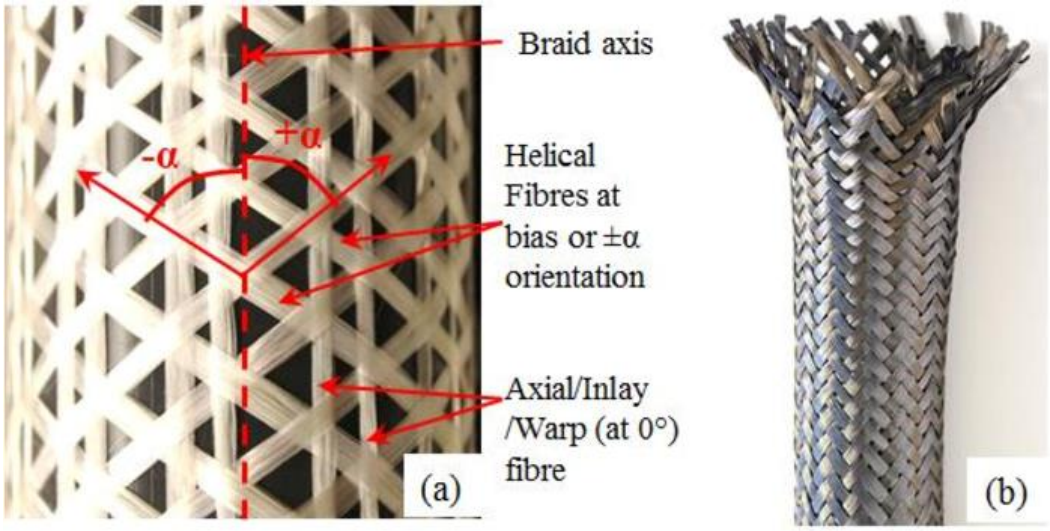

Figure 2.3 2D braiding, intertwining three or more fibre strands [15]

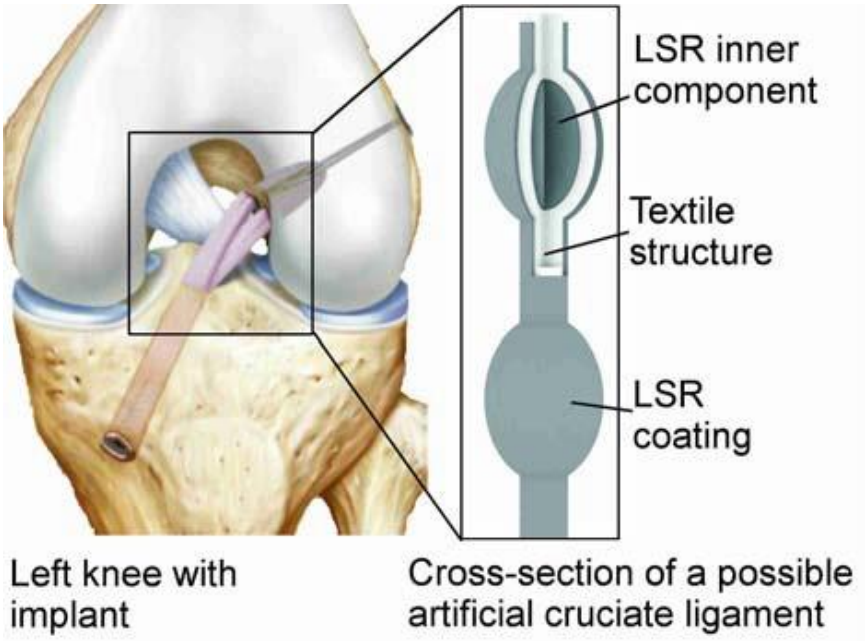

Figure 2.4 3D braided textile used as implant scaffold for knee ligament [16]

2.1.3 Knits

In knitting, yarns or threads are intertwined in a repeating array of connected loops, in 2D or in 3D. The two most common knitting methods, warp knitting and weft knitting, are illustrated in Figure 2.5. Compared with woven and braided structures, 2D knitted fabrics provide a higher across-plane mechanical properties but they are weaker in the in-plane direction [8]. The mechanical properties of knitted fabrics are highly adjustable; they can be modified by changing the types of yarns and the knitting patterns. Owing to the adjustability of knitted fabrics and relative firmness of knitted scaffolds, knitted structures are wildly used well beyond medical gauzes and surgical meshes, in regenerative medicine, performing as scaffolds for ligaments, skin, bones and cartilage [10]. For example, knitted structures can be used as artificial aorta as shown in Figure 2.6.

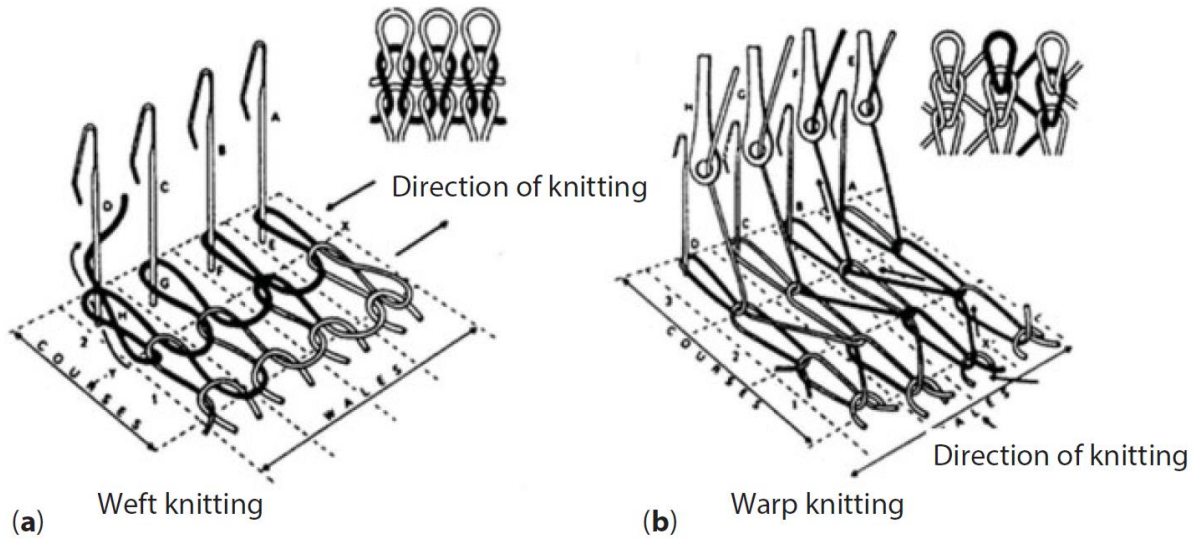

Figure 2.5 Two methods of knitting: (a) weft knitting; (b) warp knitting [6]

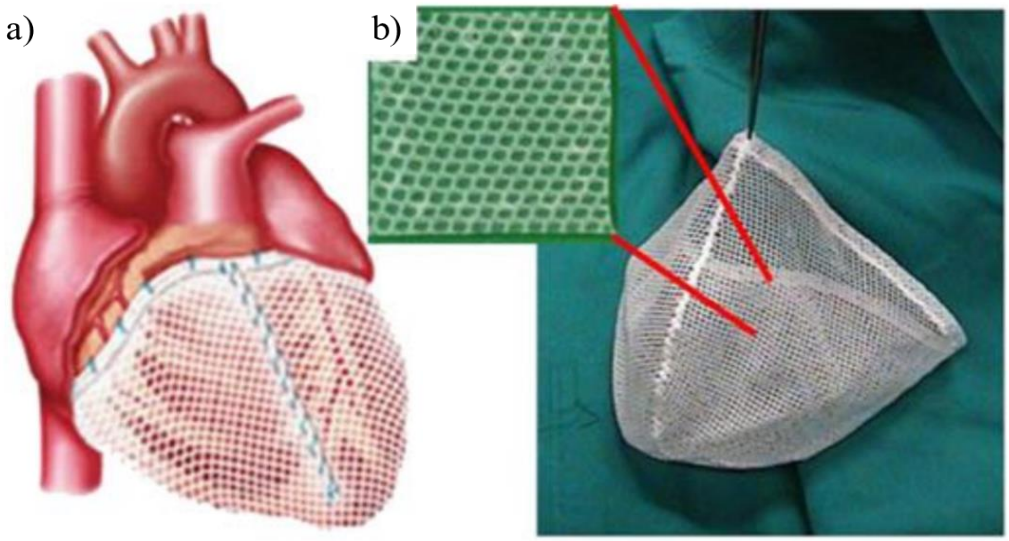

Figure 2.6 Knitted heart valve: a) after being sutured to the heart; b) before [17]

2.2 Fibre types

Fibre materials used for biomedical implants and scaffolds are generally divided into two groups, based on the source of the materials: synthetic high molecular weight polymers, and natural biomaterials. In terms of synthetic high molecular weight polymers, polyglycolic acid (PGA), polylactic acid (PLA) and PGA/PLA copolymers (PLGA) are most commonly used. On the other hand, the choice of natural fibre biomaterials is extensive, including collagen, fibrin, gelatin, sugar ammonia glycan (GAG), alginate and others [18]. Some of these materials are discussed in the following sections.

2.2.1 Polylactic acid, plyglycolic acid, and their copolymers

Polylactic acid (PLA) and polyglycolic acid (PGA) polymers are widely used for biomedical scaffold fibres because of their biocompatibility, biodegradability, non-toxicity, non-immunogenicity and non-inflammatory properties towards the human body [19]. Figure 2.7 shows the schematic of hierarchical structure of the nano-HA / collagen / PLA composite used as bone scaffold. One of the most attractive property of these fibres is that their degradation once implanted in the human body is very slow. Here, degradation refers to a change in structure accompanied by a reduction in stiffness and strength, due to a series of chemical reactions. Conversely, biodegradable implants can be absorbed in-situ, hence they do not need to be removed through additional surgery. However, if a scaffold degrades too rapidly, it cannot support sufficient load as the biological tissue heals. Thus, the degradation rate of PLA and PGA can be adapted to the biological tissue healing rate, making the transfer of loads from implants to biological tissues more gradual.

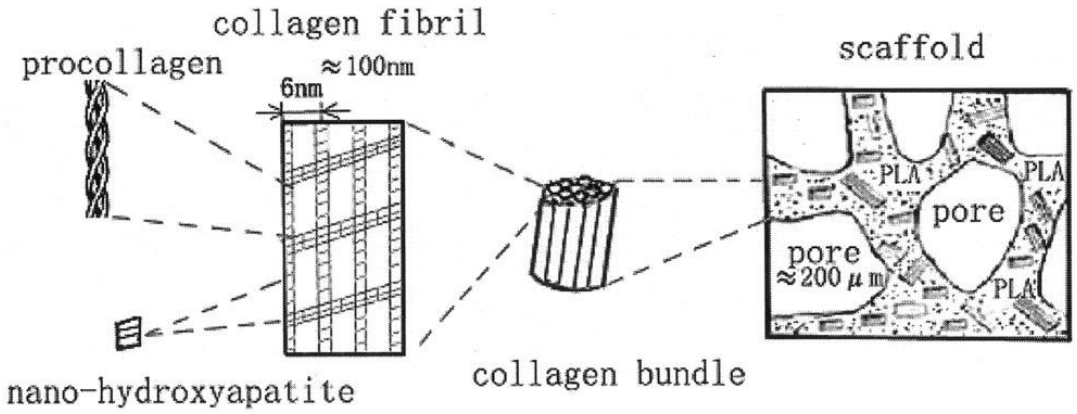

Figure 2.7 Schematic of hierarchical structure of the

nano-HA / collagen / PLA composite [20]

Poly (lactic-co-glycolic acid) (PLGA) is a copolymer of PLA and PGA. The properties of any given grade of PLGA, such as its degradation speed and tensile strength, are deeply influenced by the ratio of PLA to PGA in the copolymer. For example, a PLGA with a ratio of PLA to PGA of 70:30 has higher tensile strength than a PLGA with a ratio of 50:50. In terms of applications, in the past decades PLGA has been used for absorbable sutures. It was also introduced to the tissue engineering area [21].

2.2.2 Silk-based biomaterials (SBBS)

The most remarkable advantages offered by SBBS are high mechanical properties, ease of processing, controllable degradability, and biocompatibility. Based on the above, SBBS are commonly used for extracorporeal implants, soft tissue repair, healthcare/hygiene products and related needs.

Silkworm silk and spider silk have gained most attention. Silkworm silk fibres consist of at least two irregular cross-sectional shaped fibroin protein microfilaments, coated with sericin and a protein coating as shown in Figure 2.8 a). Conversely, the core-shell structure of spider silk fibres is a multilayer arrangement with spidroin, skin, glycoprotein and lipid layers forming a cylindrical shape. This is shown in Figure 2.8 b). Compared with silkworm silk, spider silk has excellent tensile strength and good elasticity. Nevertheless, spider silk fibres have not been commercialized, and the production of spider silk is much lower than that of silkworm silk.

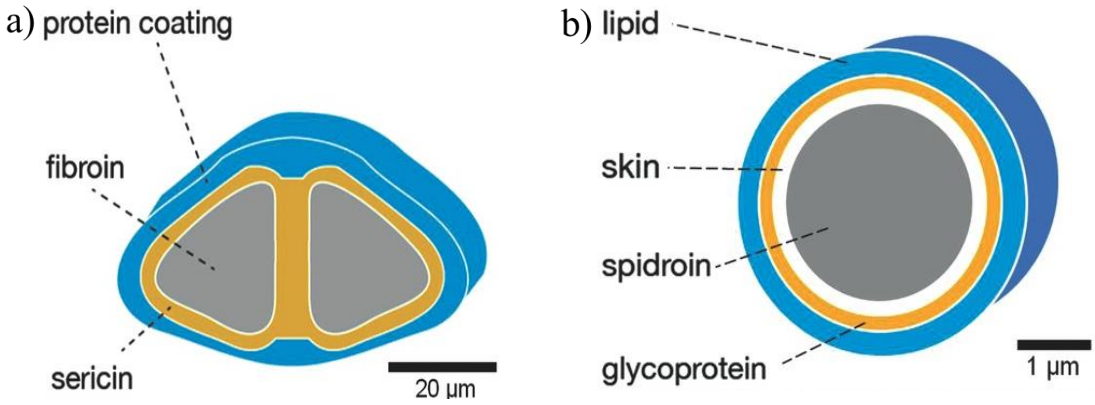

Figure 2.8 Cross-section diagrams of a) silkworm silk fibres; b) spider silk fibres [22]

Mechanical properties of silk fibres, along with those of some other common polymer fibres, are shown in Table 2.1. The table shows that silk fibres perform well in terms of balancing modulus, tensile breaking strength and elongation.

Table 2.1 Comparison of physical and mechanical properties of silk and other fibres [22]

Fiber	Density [g/cm^3]	Tenacity cN/denier [MPa]	Breaking strain [%]	Initial modulus N/tex [GPa]	Relative bending Rigidity
Raw silk	1.34	4.2(507)	20–24	7.02 (9–10)	5.2
De-gummed silk	1.27	(610–690)	4–16	/(15–17)	–
Spider silk	1.31	(875–972)	17–18	/(11–13)	–
Cellulose, rayon	1.50	2.6 (351)	18	6.12 (9.2)	4.1
Nylon	1. 14	7.5 (770)	25	3.15 (3.6)	2.8
Polyester	1.38	6.3 (782)	16	11.7 (16.2)	8.5
Polypropylene	0.91	7.0 (573)	18	7.20 (6.6)	7.9
Polyurethane	1.20	0.4(43)	500	0.01 (.012)	0.01
Aramid (para)	1.44	27.5 (3564)	2.4	88.2 (127)	61.3
Steel cord	7.85	3.0 (2120)	8	24.5 (192)	3.1
Spectra 1000	0.97	36 (3142)	3.3	112 (109)	115.5
PBO	1.56	40 (5616)	2.5	183 (286)	117.3

In terms of applications, biomedical SBBS fibres have been used in many contexts. Because of their biodegradable nature and the fact that they exhibit sufficient mechanical strength, elasticity, toughness and structural integrity, silk fibres have been used for artificial ligaments and tendons, artificial skin, sutures, vascular implants and other applicatons. Besides, according to published work [22], silk fibres can promote neuronal outgrowth, hence non-woven SBBS nerve scaffolds are also widely used and show good mechanical properties in- vitro and in-vivo. Figure 2.9 shows an artificial nerve tube prototype sample made from silk-based fibres.

Figure 2.9 Prototype sample of artificial nerve tube made from silk-based fibres [22]

2.2.3 Collagen-based materials

Collagen is mainly found in connective tissue; it is a major component of ligaments. Collagen exhibits fairly high tensile strength as a result of its unique triple-helix molecular

structure. As such, it has been extracted from animal tissues for producing biomaterials, for many years. Compared with other materials used in biomedical applications, collagen offers many remarkable advantages. Firstly, collagens promote cellular growth in many cases, which can accelerate tissue healing. Secondly, compared with other types of proteins, collagens hardly cause immune rejection, which is crucially important for implanted scaffolds. Thirdly, collagens are biodegradable based on their protein nature. Further more, they can stimulate platelet adhesion and thus have a hemostatic effect.

In tissue engineering, collagen-based materials are wildly used including as skin substitutes, vascular grafts, cartilages, bones, tendons and ligament replacements [23]. Zhang *et al*. [24] fabricated GO-collagen (GO-COL) scaffold crosslinked by 1-ethyl-3-(3-dimethylaminopropyl) carbodiimide hydrochloride (EDC) for bone regeneration. The covalent binding schematic of GO-collagen composite scaffold is shown in Figure 2.10.

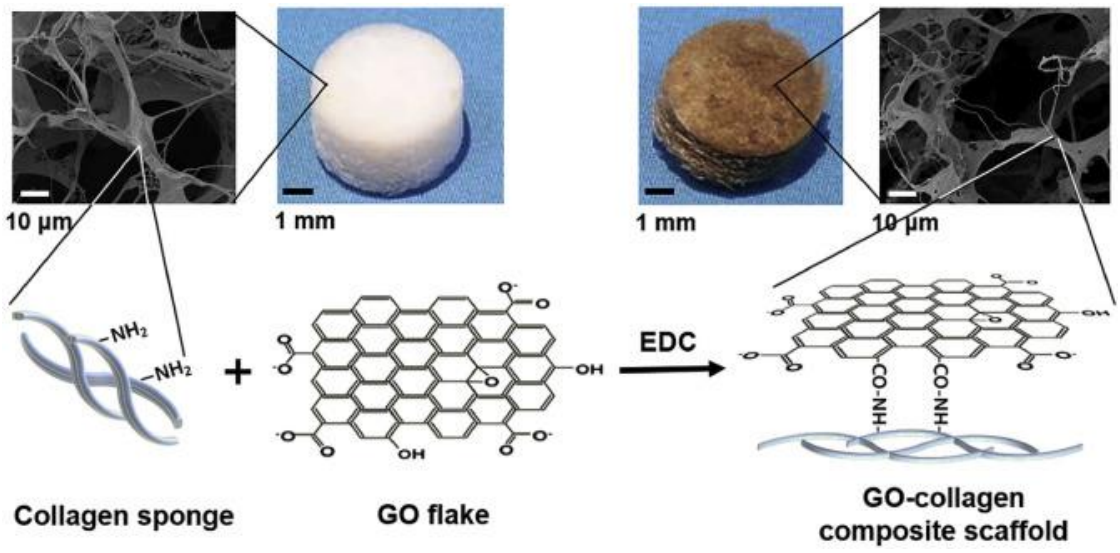

Figure 2.10 Covalent binding schematic of GO-collagen composite scaffold [24]

2.3 Properties of natural tissues and textiles implants

In this section, the properties and functions of different natural tissues including tendons and ligaments, aortic valves, nerve tubes and articular cartilages are introduced. The properties required of the textiles used for replacing these natural tissues are also discussed.

2.3.1 Tendons and ligaments

Tendons connect bones and muscles; ligaments connect different bones. Tendons and ligaments have similar components, with approximately 80% of extracellular matrix and 20% of cells [25]. Morphologically speaking, they both feature a complex hierarchical structure consisting of collagen fibrils, which are aligned axially with tendons or ligaments. The structure is shown in Figure 2.11.

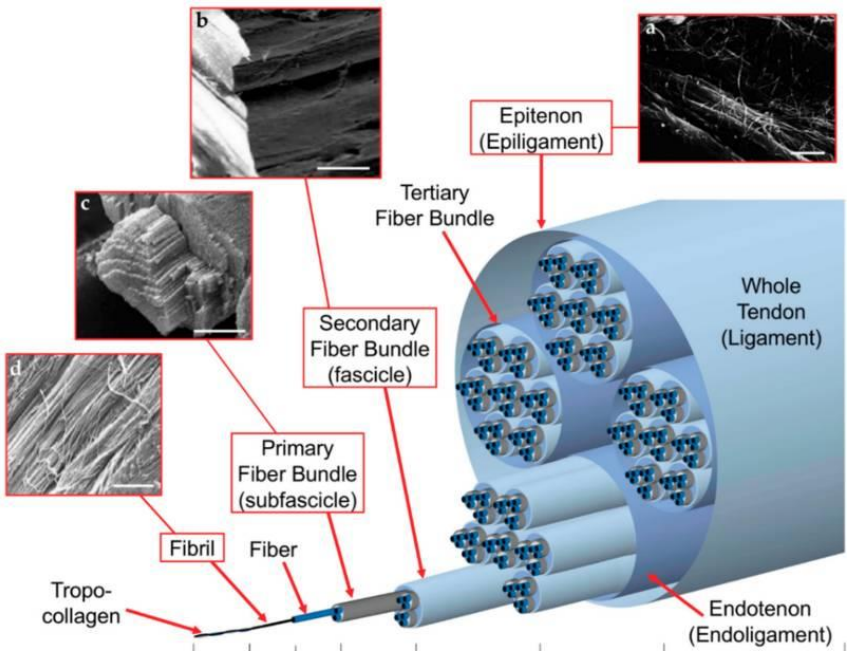

Figure 2.11 Hierarchical arrangement of fibre bundles in tendons and ligaments [25]

Tendons and ligaments exhibit typical non-linear mechanical properties, which result from this rope-like hierarchical structure. When load is applied on them, the crimped collagen fibres begin to align with each other under small initial strains. This initial behavior under small strain is called the toe region of the curve. Generally speaking, the toe region is fairly small for tendons at around 2% strain, while the range varies significantly for different kinds of ligaments at 4% to 40%. After this initial strain, stiffness goes into a linear behaviour, during which tendons and ligaments exhibit near-perfect elastic recovery. Beyond this linear part, the fibres begin to slide until the tendons or ligaments break. Typical stress-strain curve are shown in Figure 2.12.

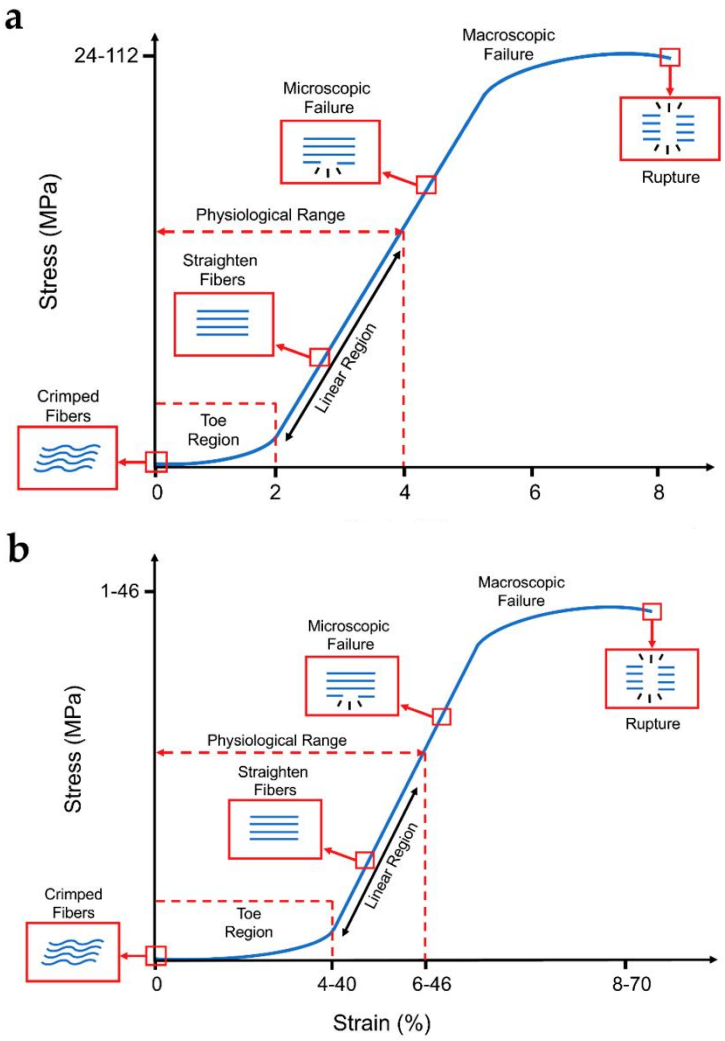

Figure 2.12 Typical stress–strain curves for: a) tendons; b) ligaments [25]

Man-made scaffolds should show the following properties as they aim to replace tendons and ligaments. The first property is biocompatibility, which promotes cells growth and infiltration, and won't cause immune rejection [26]. The second property is biodegradability. The scaffold should be degraded progressively by cells and body fluids [27]. The third property is suitable mechanical behaviour. Scaffolds are meant to provide appropriate stiffness within the range of strains applied to the tendons or ligaments being replaced. However, to prevent damage to the surrounding tissues, the scaffolds should be less stiff than the host tendons or ligaments. Besides, a degree of ductility before failure is required to prevent an abrupt failure caused by overload. The fourth property sought is that the morphology of the scaffold should be similar to that of the tendons or ligaments being replaced, in order to help with tissue regeneration. The last property is appropriate porosity, which permits cell migration, growth and infiltration.

Cooper *et al.* [4] used artificial textiles manufactured using 3D braiding technology to replace the anterior cruciate ligament (ACL). The porous scaffolds fabricated using 3D braiding showed optimal pore diameters ranging from 175 to 233μm for ligament tissue ingrowth, Figure 2.13.

Sahoo *et al.* [3] developed three groups of hybrid scaffolds based on knitted biodegradable polyester fabrics for tendon and ligament tissue engineering. The authors coated the hybrid scaffolds with a thin film of poly (ε-caprolactone) (group I), type 1 collagen (group II) and poly (d, l-lactide-co-glycolide) nanofibres (group III) and went on to compare mechanical properties,

cell seeding efficiency and cell proliferation rates. SEM pictures of the three samples and scaffolds with no coating are shown in Figure 2.14.

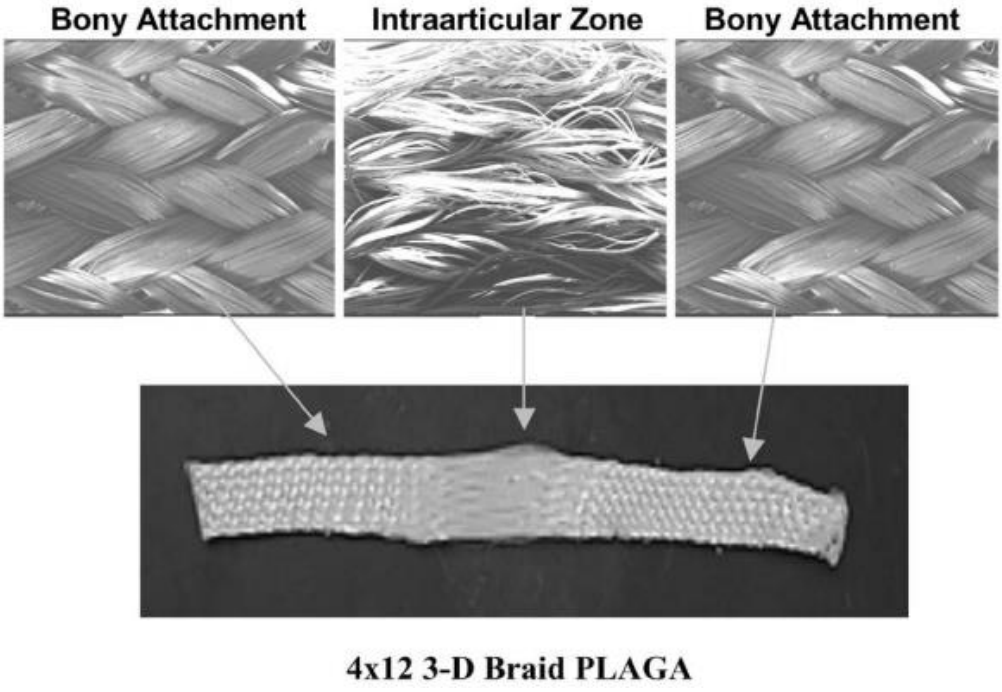

Figure 2.13 General methods of ligament scaffold design for 3D braiding [4]

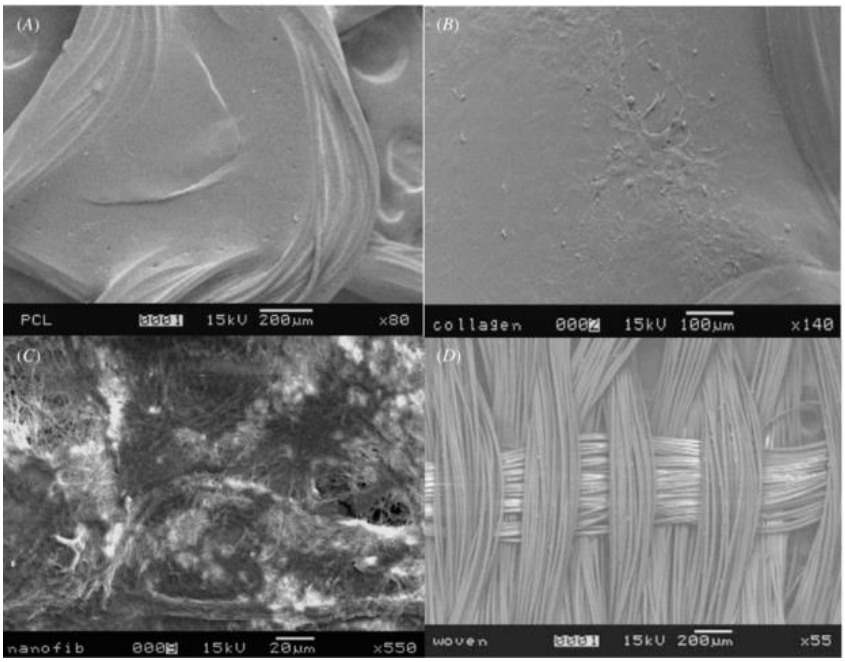

Figure 2.14 SEM micrographs of a) group I; b) group II;

c) group III; d) woven scaffolds [3]

Among diverse tendons and ligaments, the mechanical properties of knee ligaments are most related to the work presented in the following chapters. The mechanical properties of different knee ligaments such as anterior cruciate ligament (ACL), posterior cruciate ligament (PCL), medial collateral ligament (MCL) and lateral collateral ligament (LCL) differ markedly [28]. Knee ligaments function primarily in tension, which attracts the most attention. Smeets *et al.* [29] measured the tensile strength of MCL, LCL, MPFL (medial patellofemoral ligament), and ALL (anterolateral ligament) from fresh frozen human cadaveric knees. The four samples were subjected to uniaxial tensile testing to failure. Figure 2.15 shows stress-strain curves of the four specimens. An apparent toe region can be seen under low loads. The results show that among them, MCL shows the highest elastic modulus which is 441.8±117.2 MPa, while ALL shows the lowest elastic modulus which is 46.4±20.1 MPa.

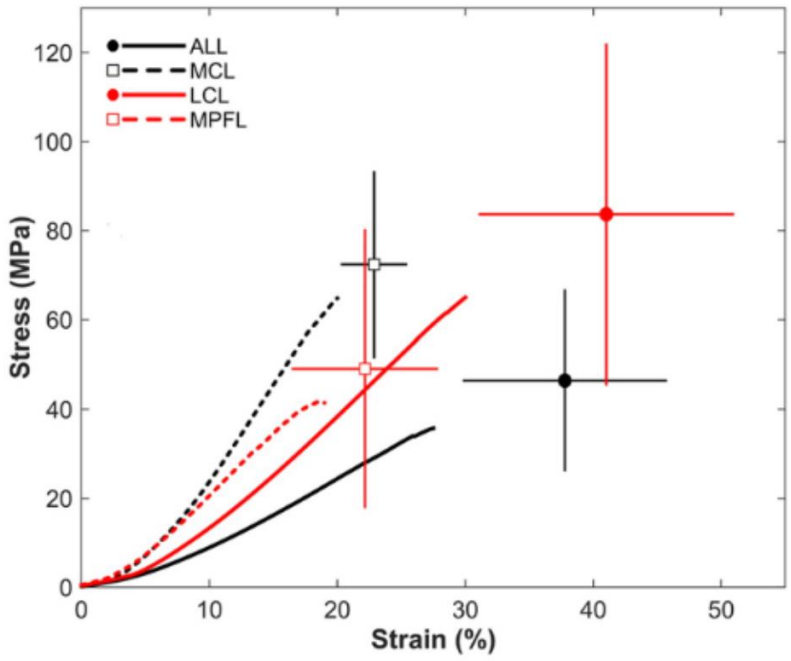

Figure 2.15 Stress-strain curves for ALL, MCL, LCL, and MPFL [29]

Other types of loads including shear, transverse and compressive loads are also applied on knee ligaments. Weiss *et al.* [30] performed shear tests on human MCLs using two clamps as shown in Figure 2.16. The reaction force-shear angle curve is shown in Figure 2.17, showing that under shear load, the behaviour of MCL ligament is higher non-linear.

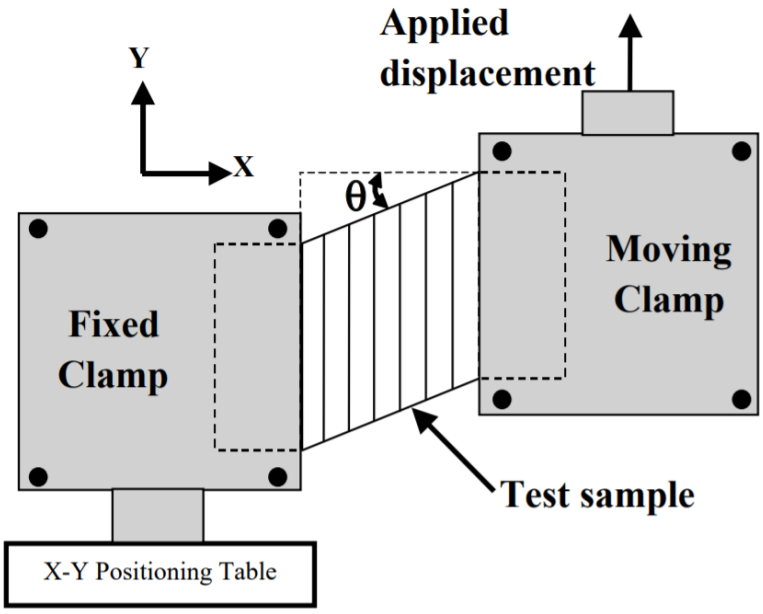

Figure 2.16 Schematic diagram of shear test as used by Weiss *et al.* [30]

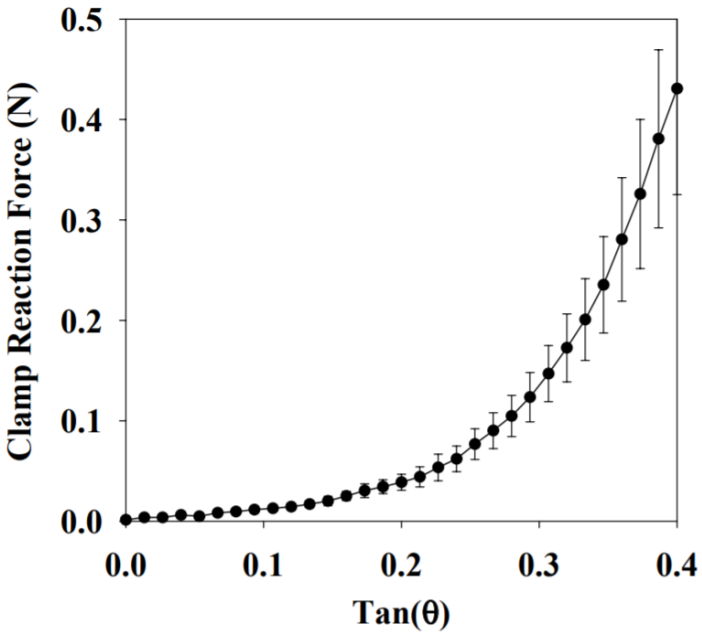

Figure 2.17 Relationship between clamp reaction force and shear angle [30]

What's more, some properties such as Young's modulus and ultimate strength were observed to be time-dependent according to research. Instead of varying the strain rate in tensile testing, Ristaniemi *et al.*[31] applied sinusoidal loads tests on ACL, PCL, MCL, LCL and patellar tendon (PT) from the same set of skeletally mature knees. Dynamic Young's modulus of the five ligaments under different loading frequencies are shown in Table 2.2.

Table 2.2 Dynamic Young's modulus of five knee ligaments

under different loading frequencies [31]

	E_{dyn} (MPa)		
	0.1 Hz	0.5 Hz	1 Hz
ACL	163.94 ± 73.98*	168.73 ± 76.84*	171.14 ± 78.43*
LCL	181.66 ± 135.26*	187.80 ± 140.20*	190.08 ± 142.14*
MCL	288.51 ± 102.56	296.60 ± 105.48	298.56 ± 105.96
PCL	214.26 ± 126.21°	220.15 ± 130.55	222.37 ± 130.26
PT	115.77 ± 93.03°**	119.38 ± 97.18**	120.45 ± 99.14**

Figure 2.18 presents results of ultimate tensile tests. Under 10 MPa, the curves show the similar trends as the tensile test results presented in this work. This will be discussed in Chapter 4.

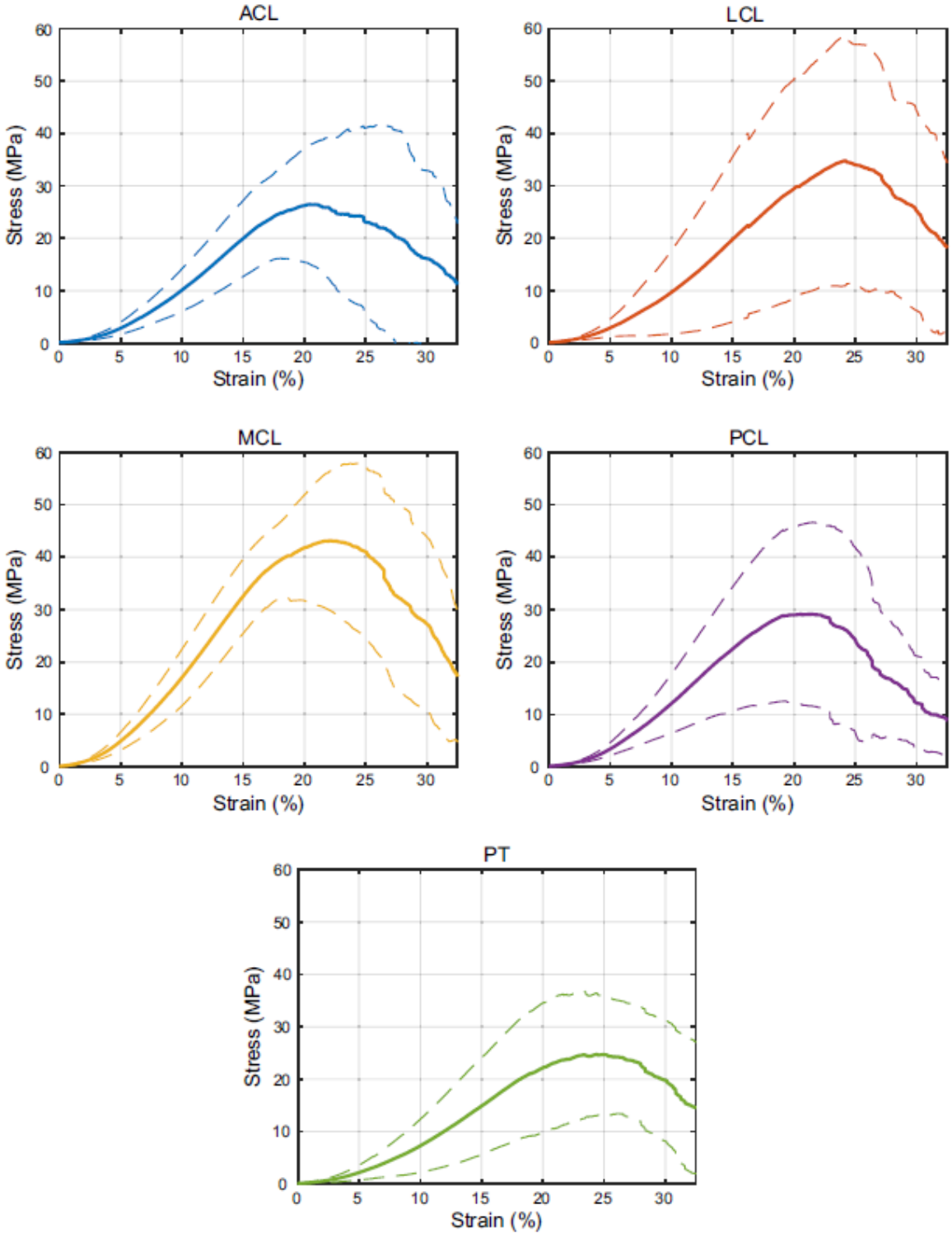

Figure 2.18 Ultimate tensile testing results for

ACL, LCL, MCL PCL and PT ligaments [31]

2.3.2 Aortic valves

Aortic valve cusps exhibit highly non-linear and anisotropic behavior, with strong in-plane coupling [32]. The complex loads carried by heart valve leaflets can be decoupled into in-plane deformation modes (i.e. shear and tensile stresses) and flexural deformation modes [33]. Furthermore, a heart valve leaflet must be able to resist rapidly changing internal forces.

In manufacturing a functional heart valve leaflet, a scaffold should have the following features [34]:

1) mimic the elasticity and anisotropic mechanical properties of natural heart valve leaflets;
2) feature aligned fibres forming a fibrous structure, similar to the microstructure of natural tissues;
3) offer elasticity and flexibility similar to those of natural tissues;
4) show controllable degradation speed and support tissue regeneration.

Breuer *et al.* [35] used a woven mesh made of PGLA fibres to make scaffolds for lamb heart valve leaflets as shown in Figure 2.19. The porous scaffolds initially functioned as a cell delivery system, transporting a large number of cells into an organism. Moreover, they provided space for cells to grow.

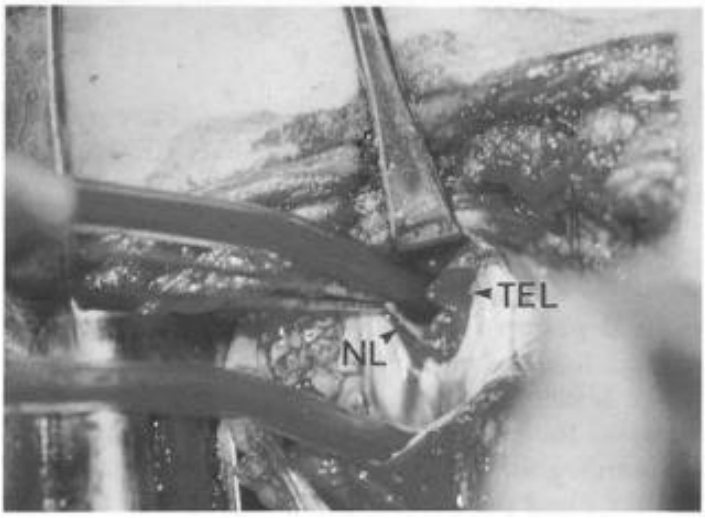

Figure 2.19 Implanted tissue engineered leaflet: NL = native leaflet;

TEL = tissue engineered leaflet [35]

2.3.3 Nerve tubes

The design of nerve repair conduits aims at facilitating a neurotrophic environment that allows proper growth and reconnection of regenerating, damaged axons with the distal end of the damaged nerve [36]. To fabricate a functional nerve tube which can enhance the rate of nerve regeneration, a nerve conduit should be degradable, durable to avoid collapse, able to prevent inflammatory reactions and also prevent infiltration of cells which hinders nerve regeneration. What's more, the ideal nerve tube should also avoid obvious swelling caused by body fluids absorption during nerve regeneration [37].

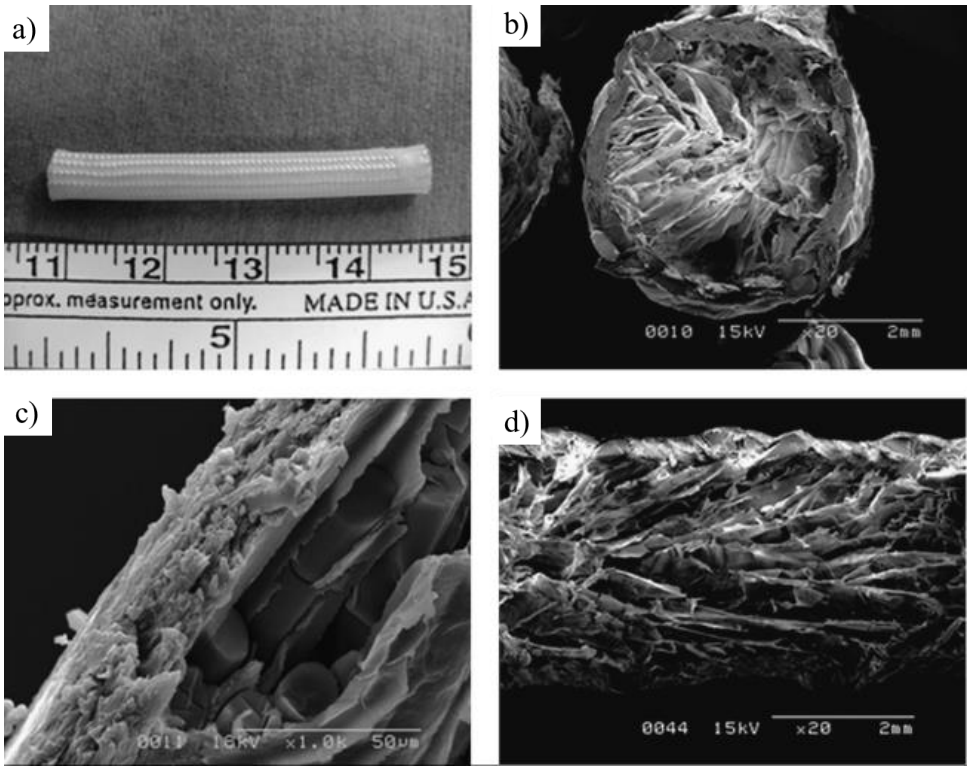

Figure 2.20 a) Macroscopic view; b) cross section; c) view of wall;

d) internal surface of the PLLA/PGA-c-tube [38]

Braiding is a potentially successful method for constructing nerve conduits, offering advantages such as the capability to form tubular structures, a high flexibility, a high radial compressive strength, and an ability for dimensional stability [6]. Ichihara *et al.*[38] braided PLLA and PGA fibres, and coated them with collagen to form novel nerve guide tubes for repairing long peripheral nerve injuries in canine models.

2.3.4 Articular cartilage

Articular cartilage is a type of connective tissue covering the extremities of long bones,

which provides a smooth surface that helps support loads up to several times the body weight, as well as dissipating energy. Cartilage is a complex, non-linear, anisotropic and fluid/solid biphasic material which can function as frictionless bearing surface, for decades. The ability to support high loads is dependent on the ability of the tissue to generate high interstitial fluid pressures, as more than 95% of the stress is carried by the fluid phase [39]. Materials used for cartilage replacement should offer high load-bearing ability, high strain to failure, high interlaminar toughness and anti-wear properties. Regarding the third point, hydrogel is usually infused into a woven fabric which provides a fluid phase and enhances mechanical properties at the same time [40].

Moutos *et al*. [11] created a 3D weaving scaffold consolidated with a cell-supporting hydrogel (agarose or fibrin) to form a composite scaffold for the functional tissue engineering of articular cartilage. The structure of the 3D scaffold and the surface appearance is shown in Figure 2.21. In comparison to 2D weaving, 3D woven structures can eliminate fibre crimp and lead to specific fibre spacing and volume fraction in each axis. Besides, the author's findings showed that porous 3D scaffolds have properties including anisotropy, viscoelasticity and tension-compression non-linearity, which are similar to those of native articular cartilage.

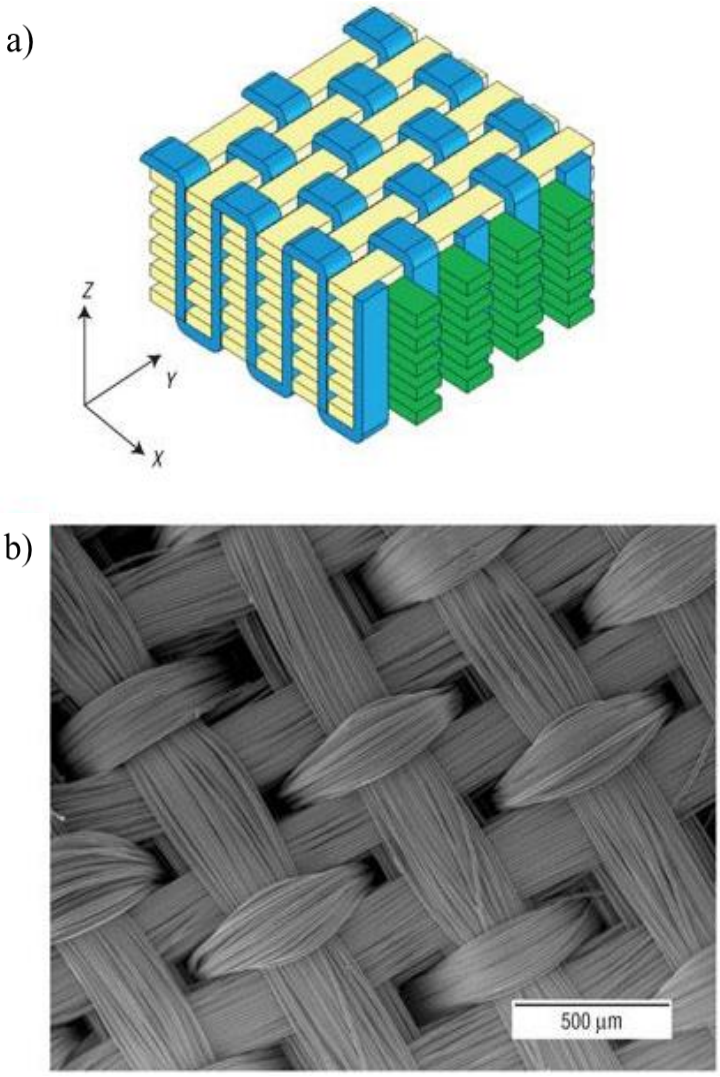

Figure 2.21 a) Structure of 3D woven used in articular cartilage;

b) surface viewed under scanning electron microscope [11]

Dai *et al.*[41] developed hybrid structures of 3D scaffolds with a knitted mesh for articular cartilage tissue engineering. The authors combined type 1 collagen which facilitated cell seeding and tissue formation, and synthetic PLGA knitted mesh which served as a skeleton scaffold. They fabricated 3 different scaffolds by controlling the way that the collagen sponge

formed, as illustrated in Figure 2.22.

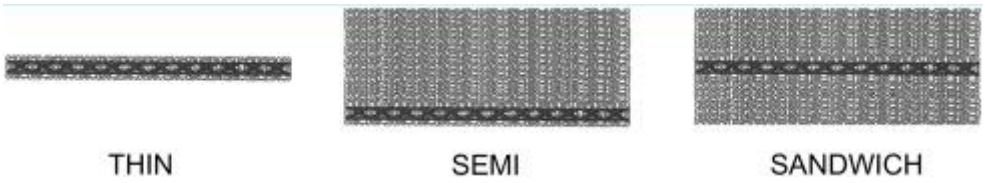

Figure 2.22 Three structural designs for PLGA/collagen hybrid scaffold. Black: PLGA knitted mesh; Gray: type I collagen sponge [41]

2.4 Advanced applications

The above sections described established applications of textiles in the biomedical area. In this section, some advanced applications introduced in recent years are presented.

2.4.1 Applications of woven textiles

Han *et al.* [42] used 3D woven silk fabric-reinforced silk nanofibrous scaffolds for dermal tissue engineering. Although the porous silk scaffolds showed advantages in terms of biocompatibility, biodegradability and low inflammatory reactions, the mechanical properties of silk were not sufficient for use as suture. In order to improve mechanical properties, degummed woven silk fabrics were used for reinforcing silk scaffolds, which significantly improved their ultimate tensile strength, elongation at break and suture retention strength. Microstructures before and after reinforcement are compared in Figure 2.23.

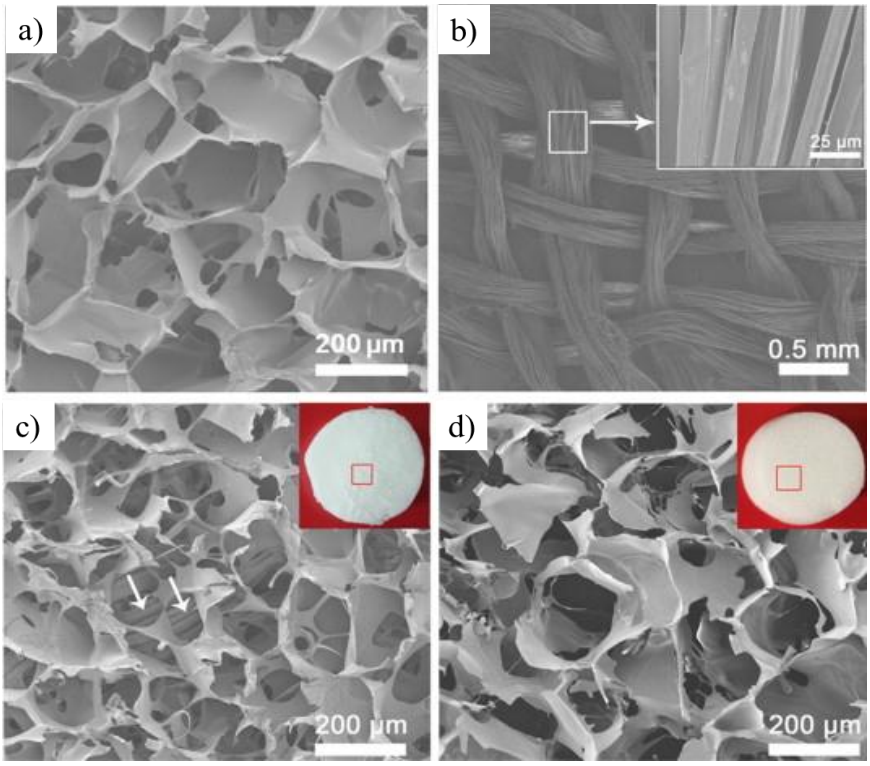

Figure 2.23 SEM image of a) silk scaffolds; b) degummed woven fabrics;

c) silk scaffolds near woven fabrics (arrows indicate the woven fabrics);

d) silk scaffolds away from woven fabrics [42]

2.4.2 Applications of braided textiles

Lou *et al.* [43] wrapped 316L stainless steel yarn and poly (lactic acid) yarn together, forming a composite yarn, and braided this composite yarn layer by layer onto a 3D bone scaffold. The introduction of 316L stainless steel not only enhanced the mechanical strength of the scaffold, but it also provided electrical conductivity to deposit hydroxyapatite, a material with strong osteoconductivity. By changing the gear ratio of the braiding machine, textiles with different braid angles were fabricated. Figure 2.24 shows how the tension strength was influenced by

the gear ratio.

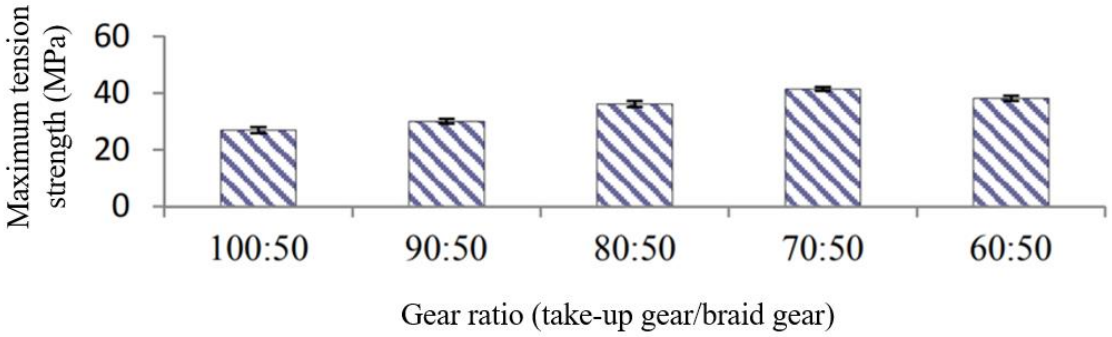

Figure 2.24 Maximum tension strength of the composite textile with different braiding gear ratios [43]

2.4.3 Applications of knitted textiles

Wang *et al.*[44] used knitted mesh-reinforced collagen–chitosan hybrid scaffolds for dermal tissue engineering. In order to improve mechanical properties, the authors used poly (l-lactide-co-glycolide) knitting mesh (PLGA) with relative fixed loops to incorporate into collagen–chitosan scaffolds (CCS) and obtain a hybrid scaffold. SEM images of the samples are shown in Figure 2.25. Further work showed that a higher scaffold mechanical strength can maintain the 3D microstructure, which plays a synergetic role in tissue regeneration and vascularization.

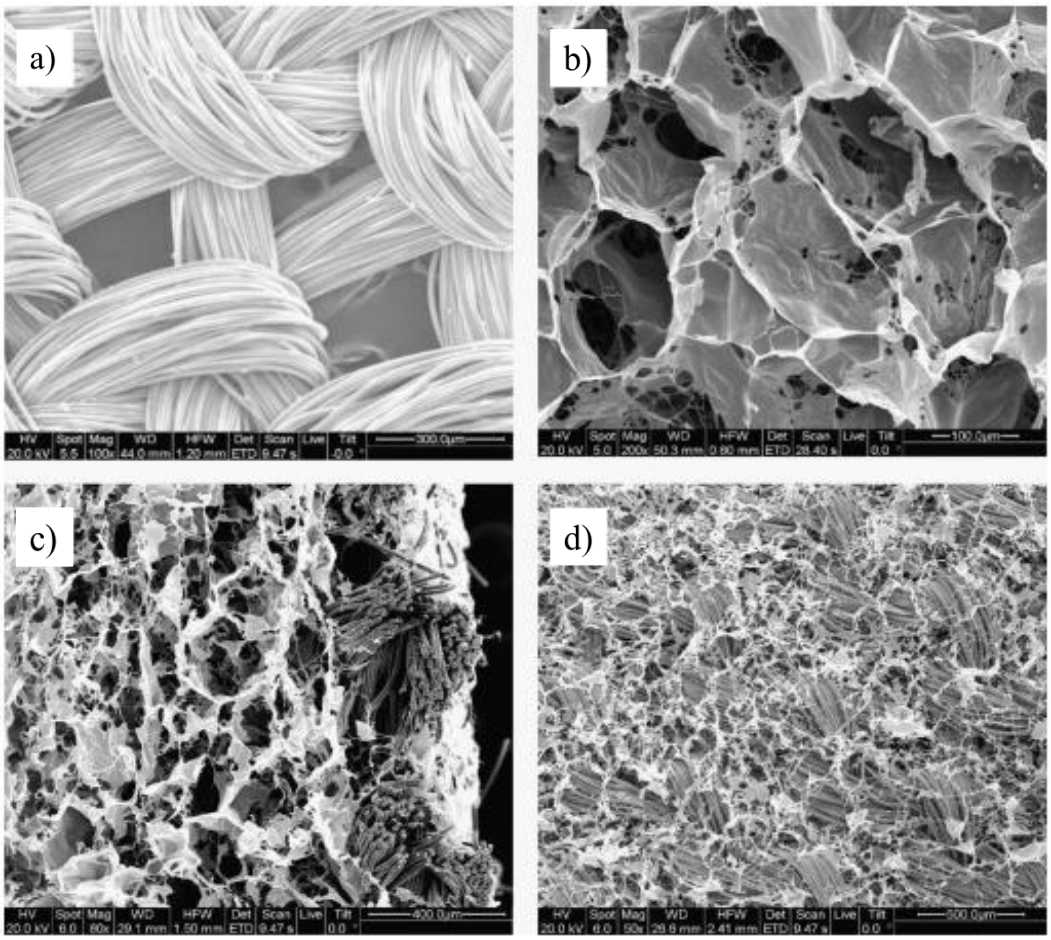

Figure 2.25 SEM images of: a) PLGAm; b) collagen–chitosan scaffold;

c) the cross-sectioned; d) the lower surfaces of PLGAm/CCS [44]

Rentch *et al.* [45] evaluated an embroidered polycaprolactone-co-lactide (PCL) scaffold for applications in bone tissue engineering. The surface of the PCL scaffolds was hydrolyzed with NaOH and coated with collagen I (coll I) and chondroitin sulfate (CS), which could induce the osteogenic differentiation of human mesenchymal stem cells (hMSC). The appearance and microstructure of the scaffold are shown in Figure 2.26.

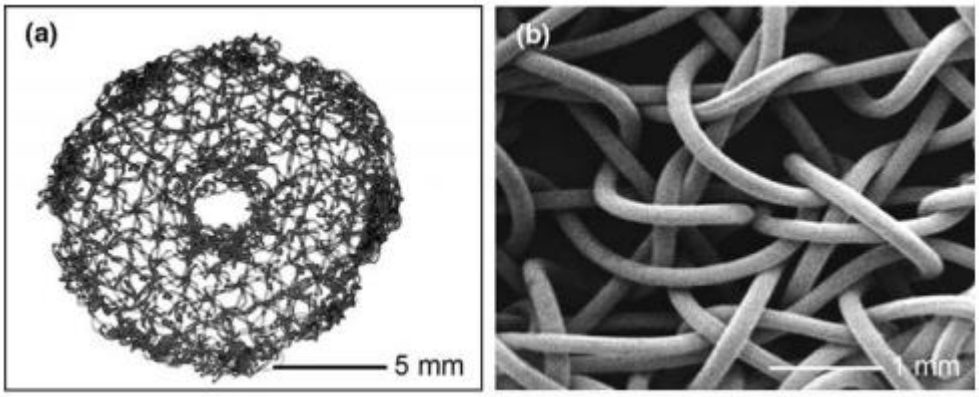

Figure 2.26 a) Photograph of embroidered PCL scaffold;

b) SEM micrograph of non-coated PCL scaffold [45]

Chapter 3 – Experimental Methods

Tensile and shear tests were performed on artificial textile knee ligaments, using an Instron 4482 universal testing frame. Original samples supplied by Neoligaments® were cut into shorter test coupons and mounted in tensile and in-plane shear testing fixtures, respectively. By recording the displacement imposed on the fixtures and the magnitude of the load applied as measured by a 10 N load cell, the constitutive behaviour of the coupons could be determined. In the following sections, the samples are described. Then, the apparatus and methods used for tensile tests and for in-plane shear tests are introduced, including dimensions of the samples and coupons, construction of the fixtures, as well as test procedures.

3.1 Samples

Three types of artificial textile knee ligaments were tested in tension and in-plane shear. All textile ligaments were non-absorbable implantable woven tapes made from thermoplastic polyethylene terephthalate fibres (PET), provided by Neoligaments®. Table 3.1 shows basic information on the three types of textile ligaments tested. The series numbers in the table refer to identification numbers used in this thesis, X being a sequential number. The masses of the ligaments were measured using a Sartorius micrometric balance, precise to ± 0.001g. The three textile ligaments are shown in Figure 3.1.

Table 3.1 Details of Neoligaments® original samples

Designation	Order code	Width (mm)	Length (mm)	Mass (g)	Series
20 × 800mm CTP	100-1012	20	800	2.1694	10x
7 × 800mm CTP	100-1057	7	800	0.8273	20x
Ortho-Tape-600mm	100-1026	3	600	1.2418	30x

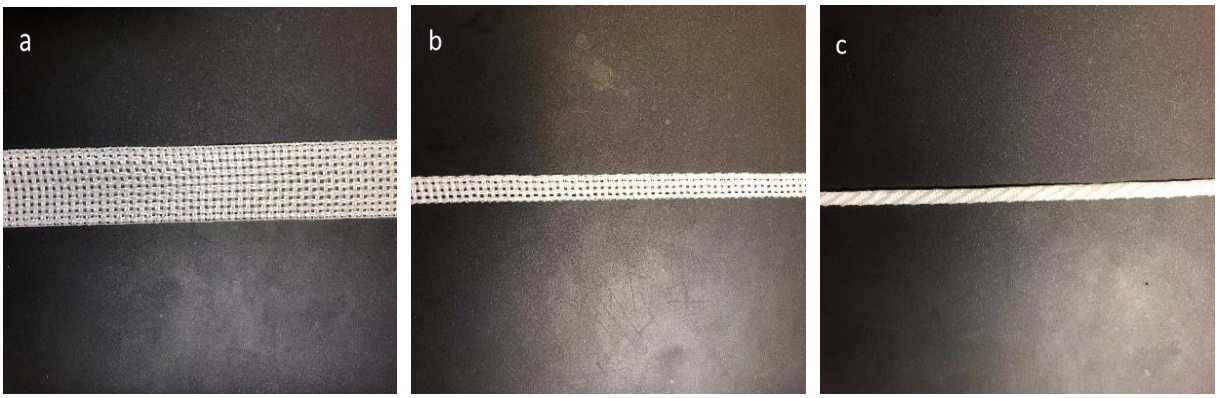

Figure 3.1 General appearance of textile ligaments: a) 20 × 800mm CTP (series 10x); b) 7× 800mm CTP (series 20x); c) Ortho-Tape-600mm (series 30x)

Series 10x and 20x ligaments are open weave structures acting as scaffolds that allow tissue ingrowth. Series 30x ligaments are dense weaves providing high strength and stiffness, with a narrower width of approximately 3mm.

3.1.1 Textile structures

The textile structures of the artificial ligaments are described in more details in this section;

dimensions of the structures are also provided.

Figure 3.2 shows the weave pattern for series 10x. In this weave pattern, yarns are aligned in groups of three, both along the warp and the weft. Openings separate neighbouring parallel groups of three yarns along both directions. The width of the openings is generally comparable with the width of a group of three parallel yarns. The initial length of artificial ligament 20× 800 CTP as provided by Neoligaments® was approximately equal to the length of the warp yarns, in the sense that the warp yarns ran along the full length of the ligament. On the other hand, weft yarns ran across warp yarns to create the weaving pattern. In Figure 3.2 b), three closely adjacent weft yarns are numbered 1, 2 and 3 from left to right. At the lateral edges of the textile ligament 10x, weft yarns 1 and 3 separate in a total of four half yarns. Two of these half yarns merge together and turn back into the structure to form weft yarn 2, while the other two merge into adjacent groups of weft yarns. The ends of the artificial ligament are heat-set as shown in Figure 3.2 c) to prevent detachment and to make it easier to go through human tissues upon surgery.

The following Figures 3.3 to 3.5 show the interlacing pattern in better detail, along with representative dimensions of the yarns and textile structure. The images confirm that the same type of yarn was used along the warp and weft of the textile ligaments. Table 3.2 shows averages and standard deviations of the dimensions mentioned above. In Table 3.2, the values of yarn width are calculated with 18 measurements while the values of openings are calculated with 9 measurements. One should bear in mind that such measurements are representative as

opposed to exact, given variability and the highly deformable nature of textiles both at the level of the textile structures and of the yarns making up these textile structures.

Table 3.2 Averages and standard deviations of dimensions, ligament series 10x

	Average (mm)	Standard deviation (mm)
Yarn width (weft)	0.6639	0.0654
Yarn width (warp)	0.5239	0.0809
Opening along weft	1.0921	0.0622
Opening along warp	0.7944	0.1058

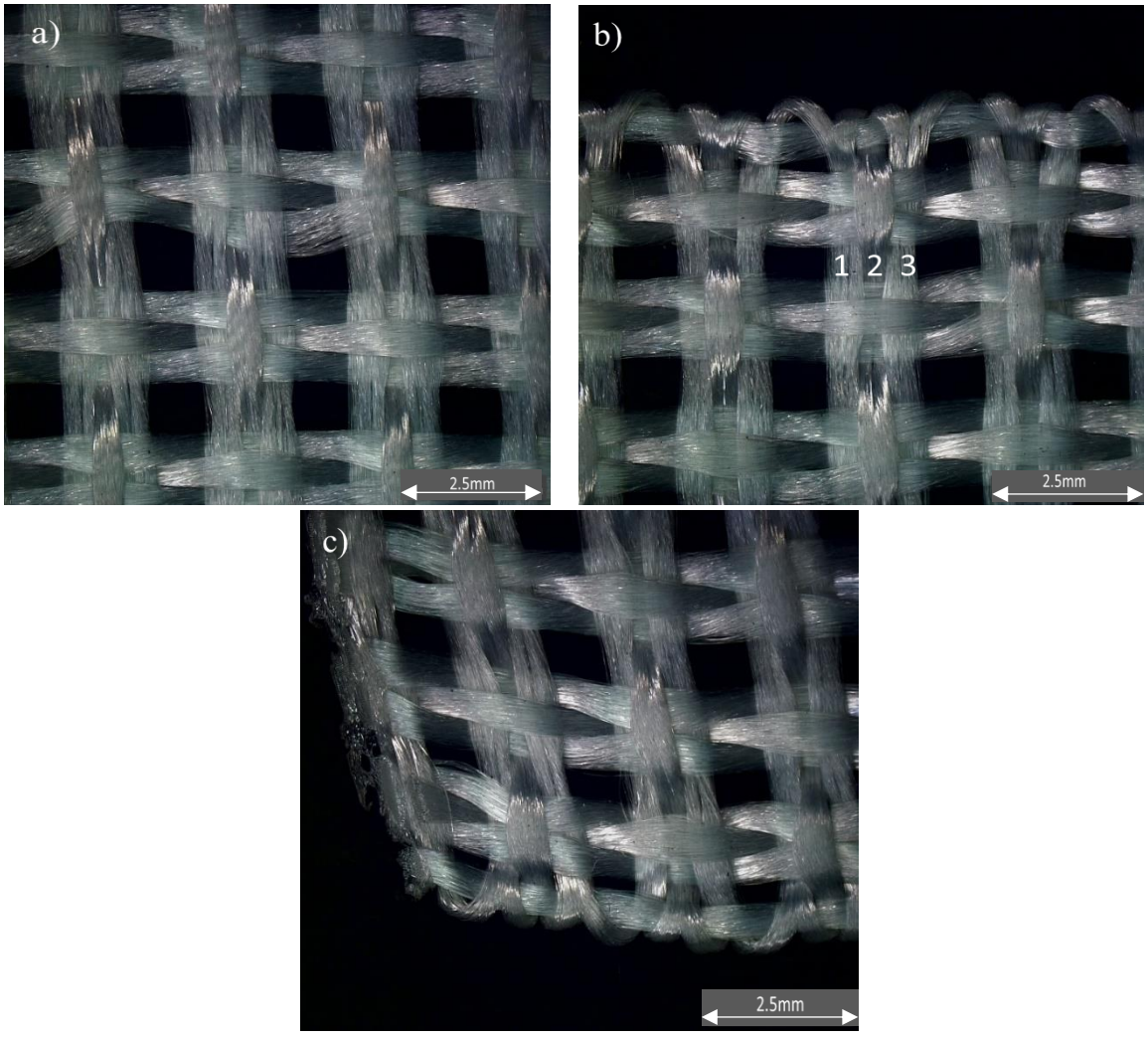

Figure 3.2 Weave pattern, artificial ligament series 10x: a) continuous structure; b) side of textile ligament; c) heat-set end of textile ligament

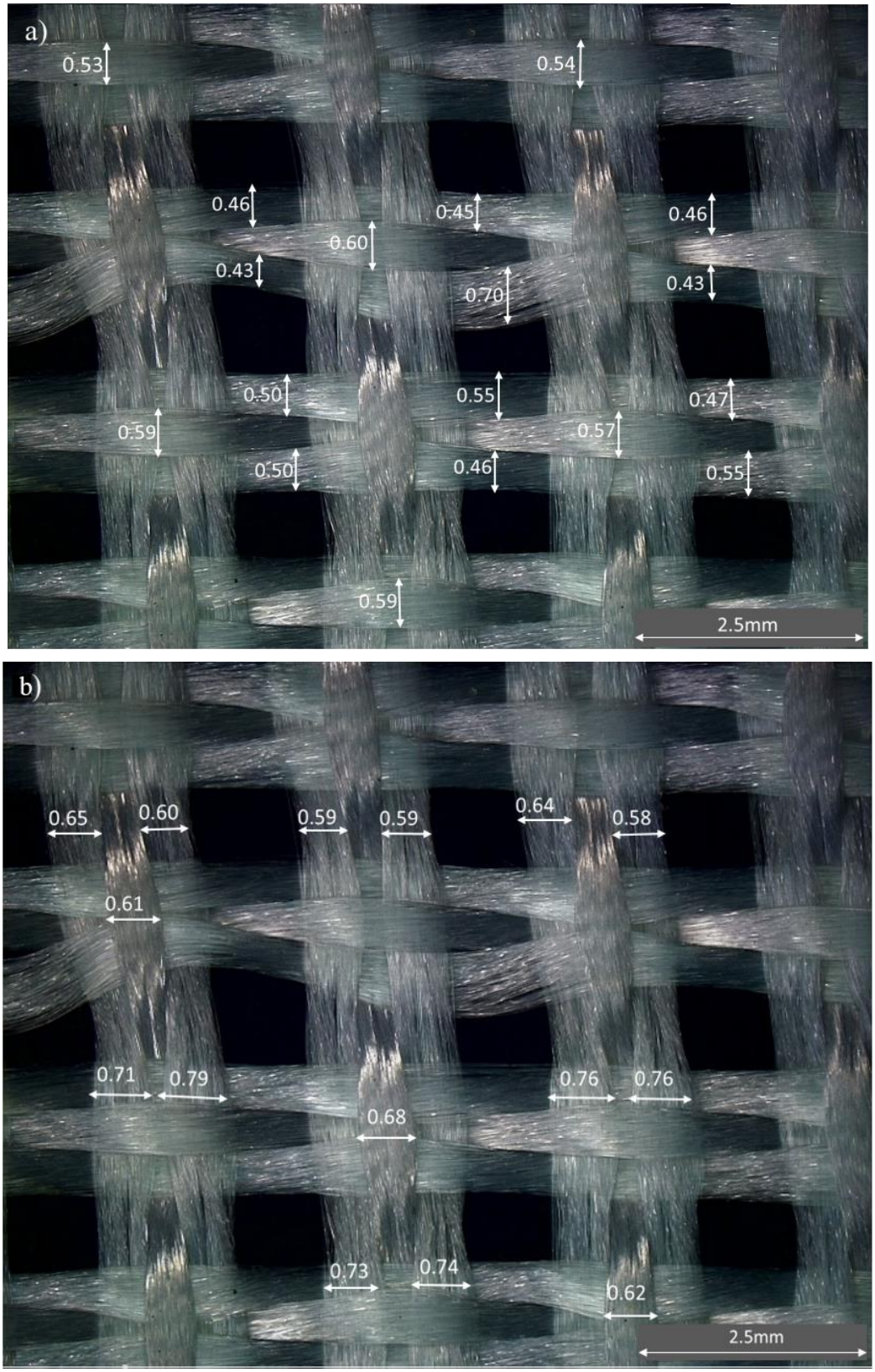

Figure 3.3 Weave pattern, series 10x, with representative yarn dimensions (mm):

a) warp yarns; b) weft yarns

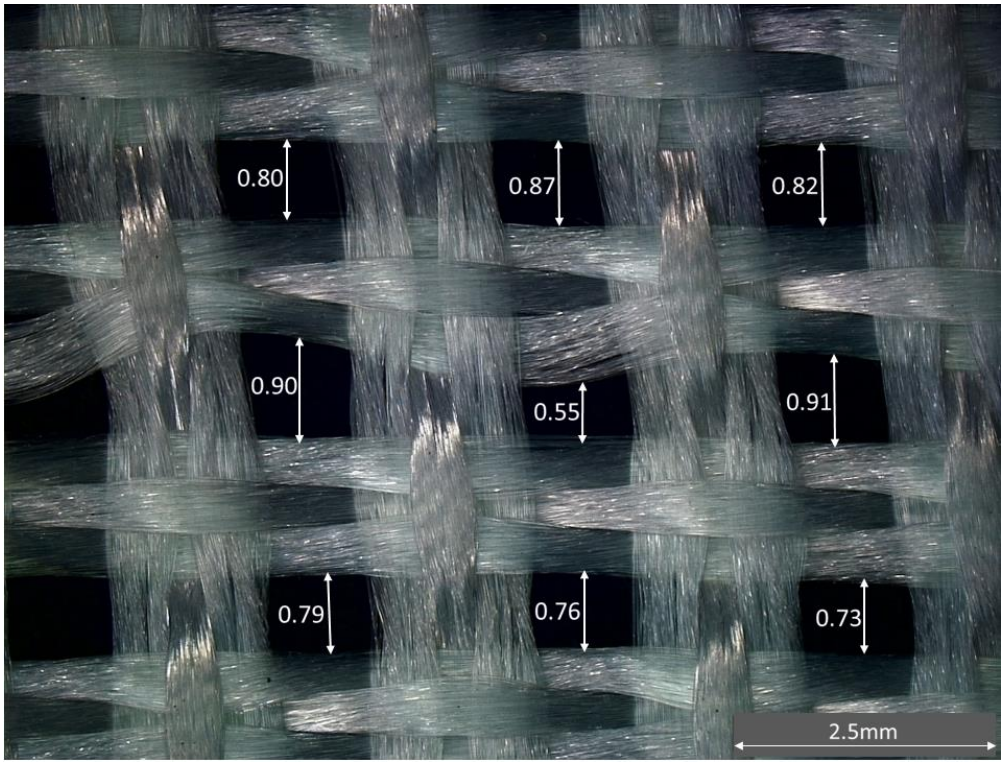

Figure 3.4 Weave pattern, series 10x, with representative dimensions of openings between warp yarns (mm)

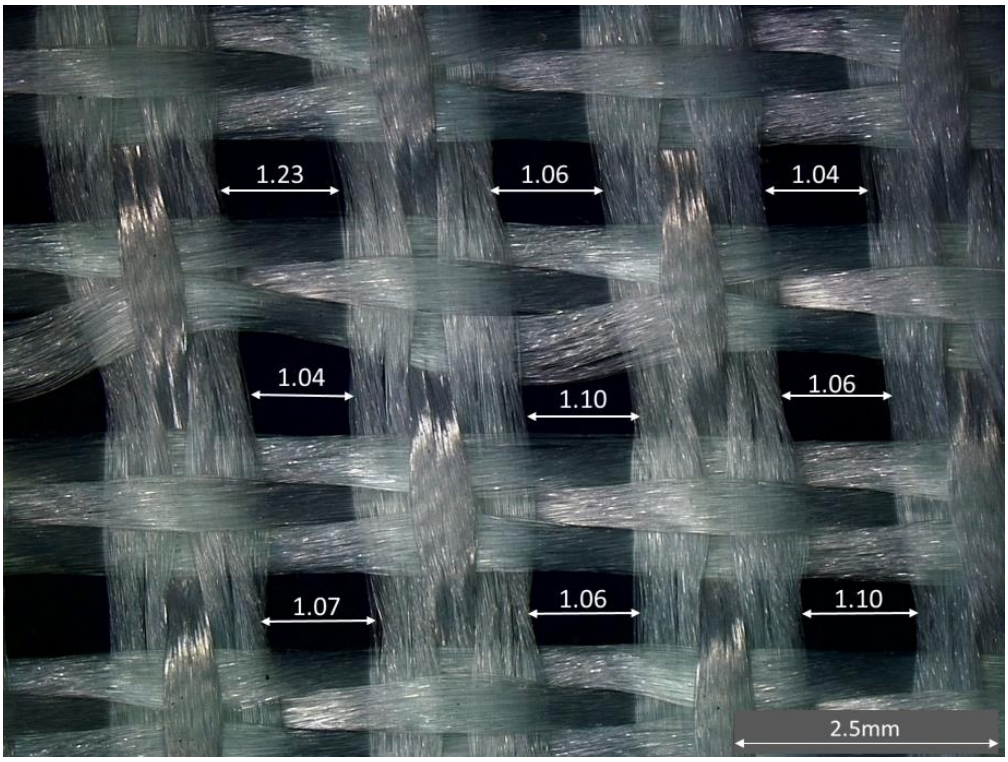

Figure 3.5 Weave pattern, series 10x, with representative dimensions of openings between weft yarns (mm)

Figure 3.6 shows a 3D model of the interlacing pattern for series 10x, created using textile modeling software TexGen. The software and models are discussed in Chapter 6 of this thesis.

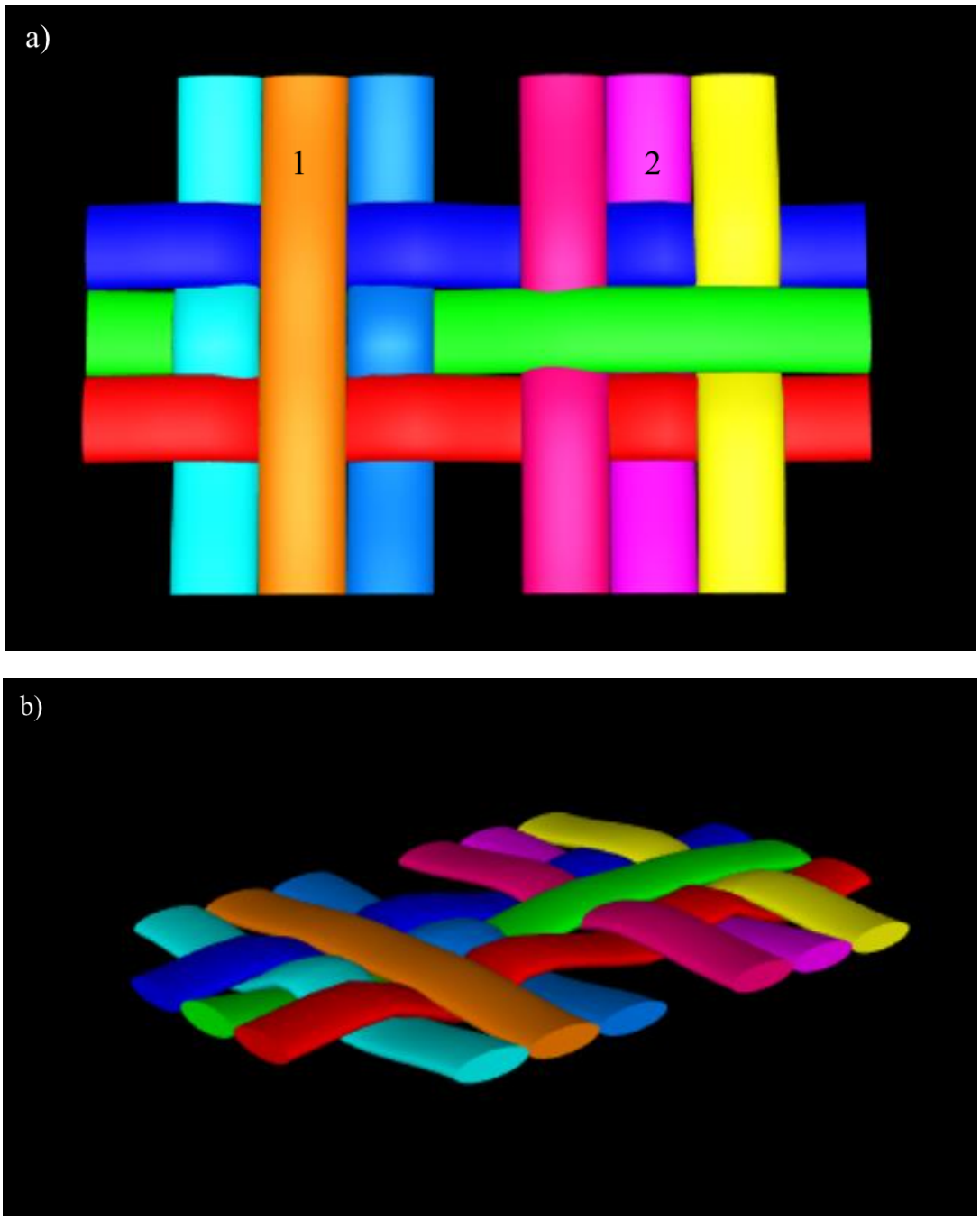

Figure 3.6 3D model of series 10x: a) top face; b) isometric view

In Figure 3.6 a), the interlacing pattern consist of a left part and a right part, each of which includes 3 weft yarns. The two parts of the pattern show reverse symmetric. In an adjacent repeat, the left and right parts exchange their position. As shown in the Figure, weft yarn 1 is always over the three warp yarns while weft yarn 2 is always under the same warp yarns. However, for the adjacent repeat under it, weft yarn 1 is always under and weft yarn 2 is always over.

The weave pattern of ligament series 20x was very similar to that of ligament series 10x. Except for differences in width, where series 10x measured approximately 20mm and series 20x measured approximately 7mm, the only major difference was in the weave pattern used at the edges. One edge was similar to the edges of ligament 10x while on the other edge, weft yarns looped backwards on themselves and into warp yarns, with a more complex structure. This is shown in Figure 3.7.

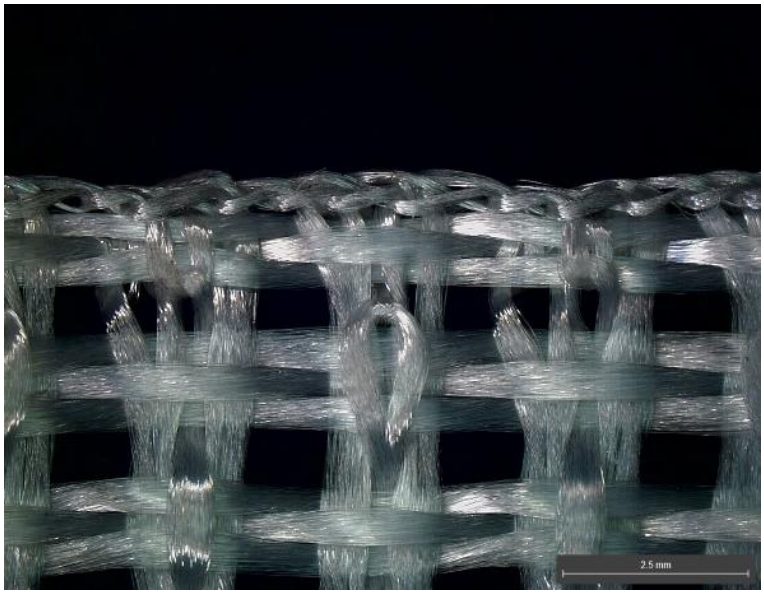

Figure 3.7 One of the edge structure of series 20x (7×800 mm CTP)

The following Figures 3.8 to 3.11 show representative dimensions for the yarns and the textile structure of ligament series 20x.

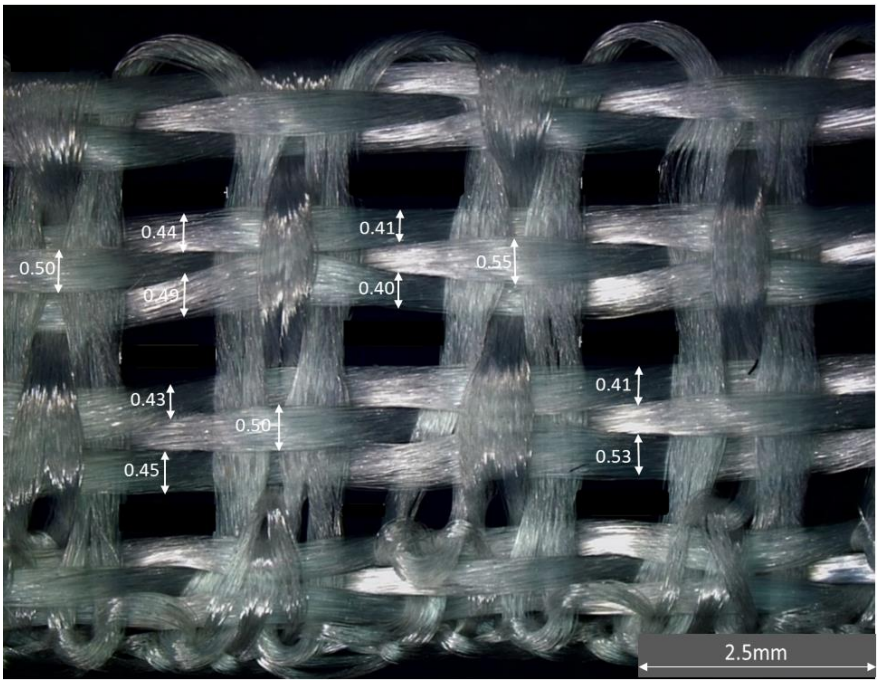

Figure 3.8 Weave pattern, series 20x, with warp yarn dimensions (mm)

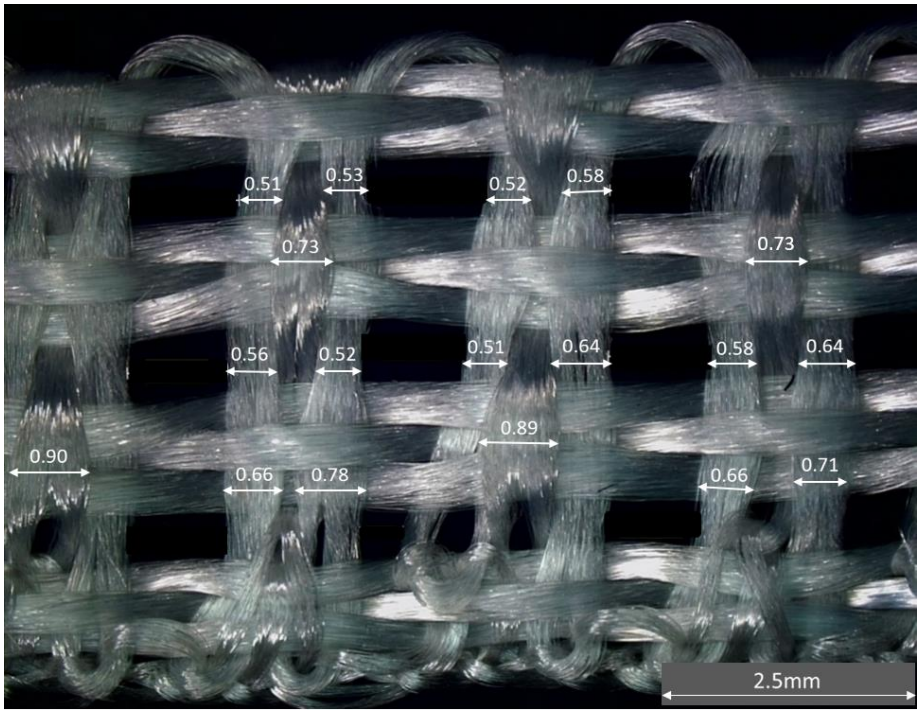

Figure 3.9 Weave pattern, series 20x, with weft yarn dimensions (mm)

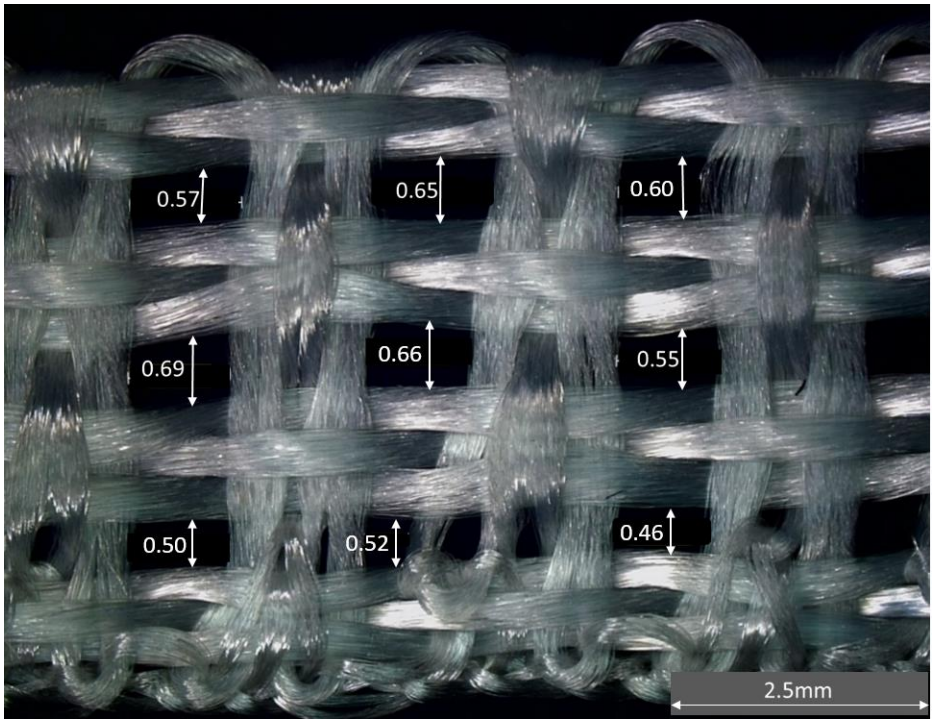

Figure 3.10 Weave pattern, series 20x, with representative dimensions of openings between warp yarns (mm)

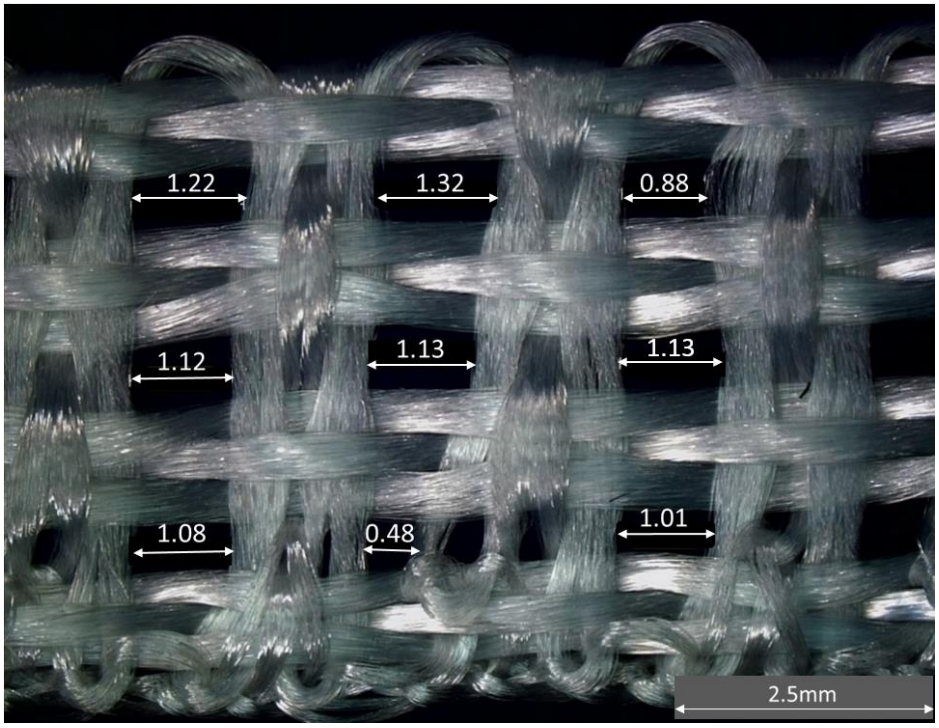

Figure 3.11 Weave pattern, series 20x, with representative dimensions of openings between weft yarns (mm)

Interlacing symmetry in ligament series 20x is the same as observed with series 10x. Averages and standard deviations of dimensions appear in Table 3.3. Around 15 measurements were made, towards calculating yarn widths, and 9 for openings.

Table 3.3 Averages and standard deviations of dimensions, ligament series 20x

	Average (mm)	Standard deviation (mm)
Yarn width (weft)	0.426	0.0638
Yarn width (warp)	0.468	0.0015
Opening along weft	1.041	0.2297
Opening along warp	0.578	0.0739

Series 30x artificial ligaments feature a dense weave. As shown in Figure 3.12, interlacing follows an S-twill pattern with an apparent twill line. Figure 3.13 shows representative dimensions of the yarns and textile structure of ligament series 30x.

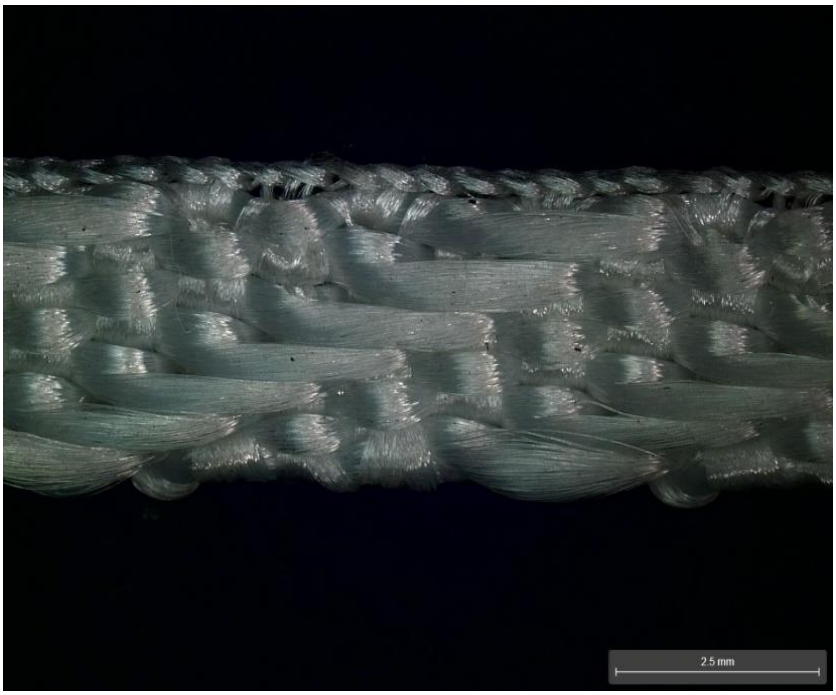

Figure 3.12 Weave pattern, series 30x (Ortho-Tape-600mm)

Figure 3.14 shows a 3D model of the interlacing pattern for ligaments series 30x. Table 3.4 shows averages and standard deviations of weft and warp yarn widths. 10 and 15 measurements were made for calculating weft yarn and warp yarn widths, respectively.

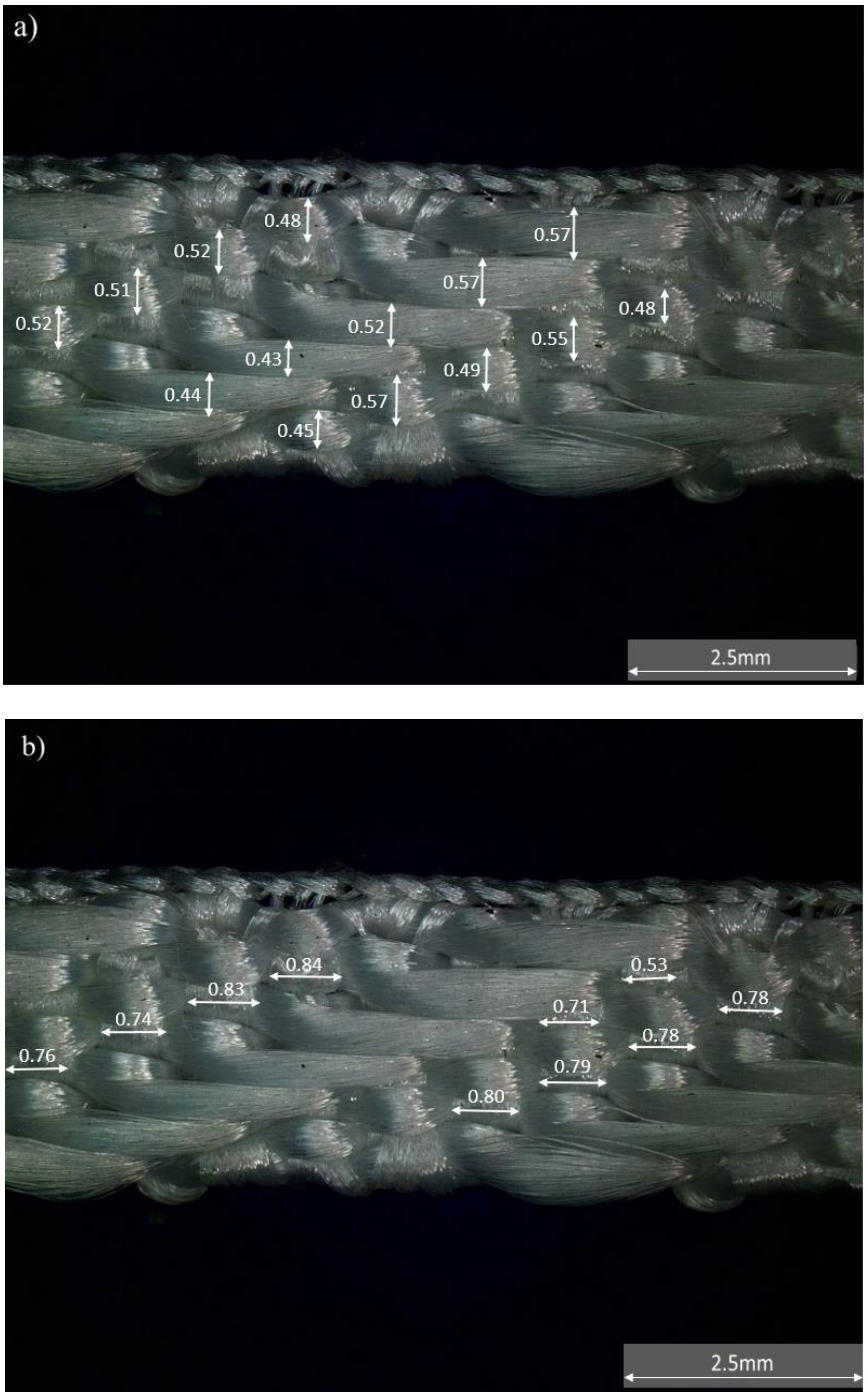

Figure 3.13 Weave pattern, series 30x, with representative yarn dimensions (mm):

a) warp yarns; b) weft yarns

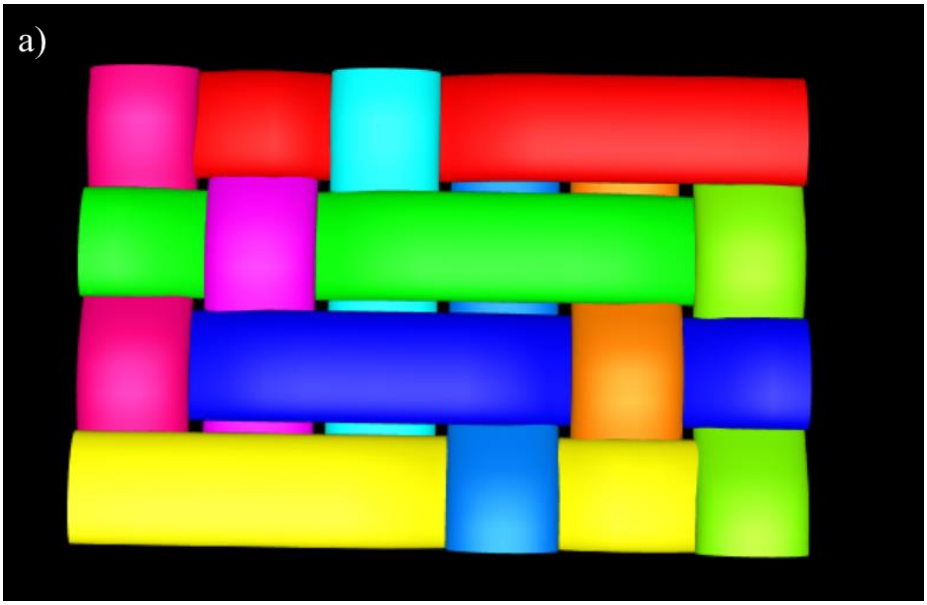

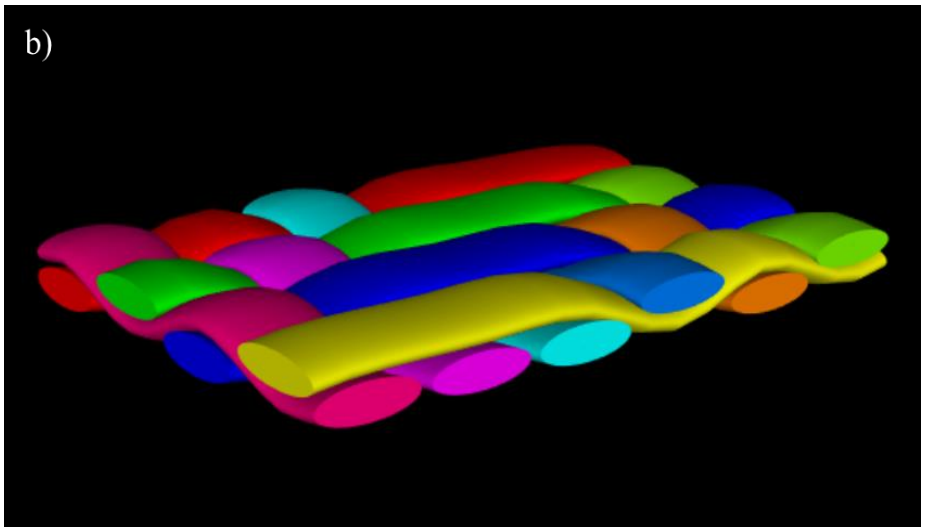

Figure 3.14 3D model of ligament series 30x: a) top face; b) isometric view

Table 3.4 Averages and standard deviations of dimensions, ligament series 30x

	Average (mm)	Standard deviation (mm)
Yarn width (weft)	0.840	0.0156
Yarn width (warp)	0.513	0.0024

3.1.2 Volume fraction of the samples

In order to analyse the stiffness of the samples and compare experimental data with data generated from models, the volume fraction of the samples must be known. The mass of the three original samples appears in Table 3.1. The following Equations 3.1 to 3.3 show the calculation of the volume fraction:

$$V_{fibre} = \frac{m_{yarn}}{\rho} \tag{3.1}$$

$$vf_{fibre-yarn} = \frac{V_{fibre}}{V_{yarn}} \tag{3.2}$$

$$vf_{fibre-sample} = vf_{fibre-yarn} \times vf_{yarn-sample} \tag{3.3}$$

where V_{fibre} is the volume of the fibres within a single yarn, m_{yarn} is the mass of a single yarn, ρ is the density of PET fibres, $vf_{fibre-yarn}$ is the volume fraction of fibres in a single yarn, V_{yarn} is the volume of a single yarn, $vf_{fibre-sample}$ is the volume fraction of fibres in an original sample and $vf_{yarn-sample}$ is the volume fraction of yarns in an original sample. The widths of yarns are shown in Table 3.2 and 3.3, thus V_{yarn} and V_{sample} can be determined by measuring the lengths and estimating the cross section area by assuming that the cross section of a yarn is an ellipse. m_{yarn} can be measured using a balance.

3.1.3 Sample preparation

Standard ASTM D5034-09 titled ‘Standard Test Method for Breaking Strength and Elongation

of Textile Fabrics (Grab Test)' [46] recommends that 100 mm wide specimens be cut to a length of 150 mm in order to quantify breaking strength and elongation in fabrics. Considering the width of the samples tested in this thesis as well as limited ligament avilability, a coupon gauge length of 75 mm was used for the tensile tests. Each original textile ligament was cut into five coupons measuring 105 mm in length. This length was used in determining the dimensions of the test rigs, which are discussed in Section 3.2.1. The identification scheme used for coupons of every type and the average mass of each coupon appear in Table 3.5 along with the proportions of warp and weft yarns.

Table 3.5 Coupon identification, proportion of warp and weft yarns and mass of coupons for all types of artificial textile ligaments

Series	Coupon	Warp yarns (%)	Weft yarns (%)	Mass (g)	Average mass (g)
10x	101	58.9	41.1	0.372	0.3688±0.0195
	102			0.368	
	103			0.366	
	104			0.382	
	105			0.356	
20x	201	57.9	42.1	0.142	0.1426±0.0016
	202			0.144	
	203			0.144	
	204			0.14	
	205			0.143	
30x	301	65.8	34.2	0.213	0.2144±0.0331
	302			0.215	
	303			0.211	
	304			0.221	
	305			0.212	

3.2 Tensile test apparatus

In this section, the appearance, operation and structure of the tensile test apparatus are described. The tensile test procedures are also introduced, including how to mount the coupons, application of load and description of cycles applied to the samples.

3.2.1 Textile test fixture

The design and dimensions of the apparatus used for performing tensile tests appear in Figure 3.2.1. The complete fixture consists of a lower grip and an upper grip. The fixture was mounted in an Instron 4482 screw-driven universal testing frame. The lower grip was fixed to the lower platen of the testing frame using M6 bolts at four set points. The upper grip was attached to a 10N load cell through a 5 mm steel screw and corresponding hole on the grip. Upper and lower jaws measuring 50 mm by 10 mm overall can be seen in Figure 3.2.1. Coupons were secured vertically between the two jaws, using two manually tightened screws at each jaw. The entire fixture was built of aluminium.

During a test, the lower grip did not move while the upper grip moved upwards with the traverse of the universal testing frame. As the distance between the lower and upper grips increased, the sample was subjected to increasing strain, tensile load and tensile stress. The procedure is described in the following section.

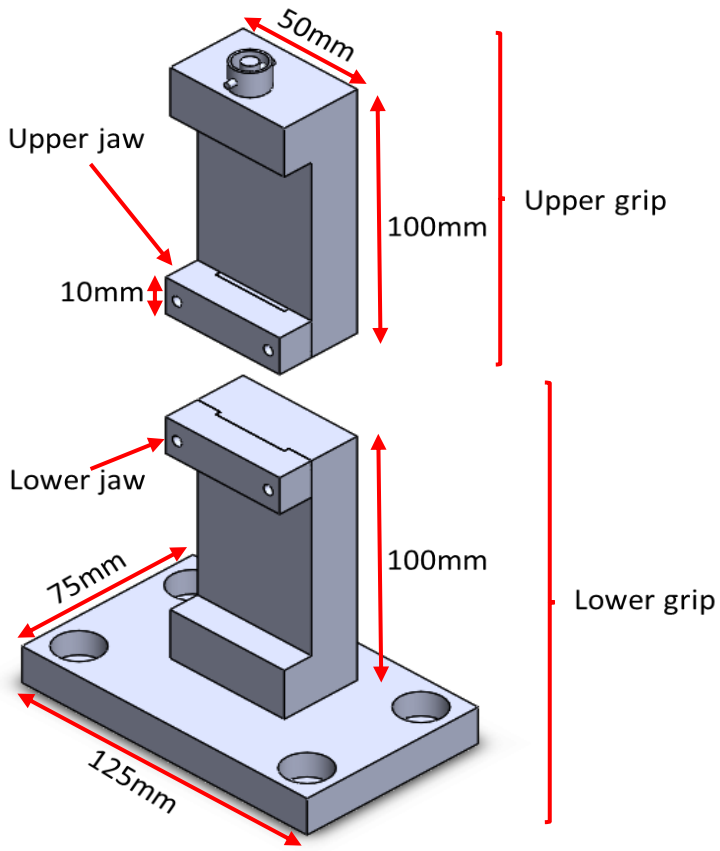

Figure 3.2.1 Design and dimensions of tensile testing fixture [47]

3.2.2 Tensile test procedures

Coupons were mounted manually in the fixture in a naturally straight state, without bending or stretching. Warp yarns were mounted as perpendicular to weft yarns as possible, and as parallel to the direction of applied displacement as possible, so that tensile loads acted longitudinally on the coupons, as accurately as possible. However, given the flexible nature of the coupons, the warp and weft yarns were not rigorously perpendicular in a theoretical sense and the distances between each group of weft yarns was not rigorously constant, as shown in Figure 3.2.2.

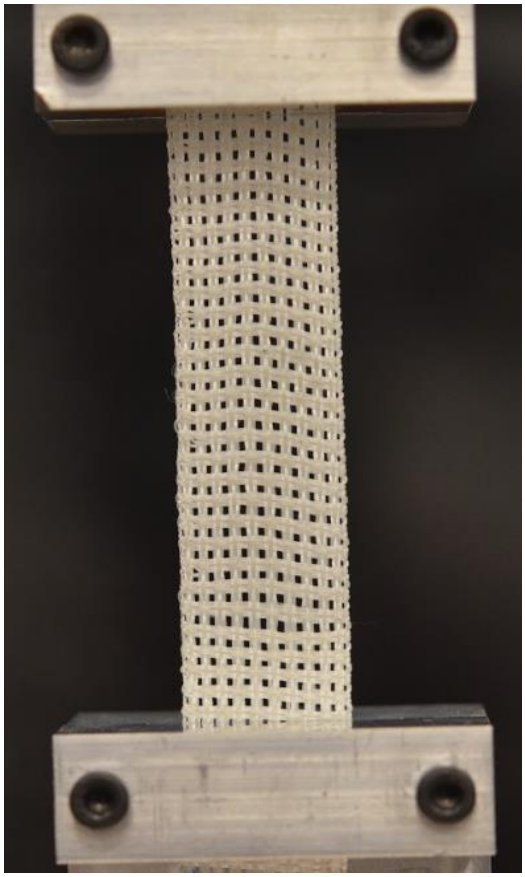

Figure 3.2.2 Coupon mounted in tensile test fixture

Each coupon was tested at a rate of 5mm/min until tension in the coupon reached 5.5 N. Much deformation occurs under lower loads in textile ligaments, hence applying a relatively low level of stress was deemed sufficient to analyse the relationship between load and deformation. Furthermore, applying lower loads well within the elasticity limit of the PET fibres ensured that coupons were not damaged, hence they could be tested multiple times.

Each coupon was cycled seven times. Each cycle has a unique identification number as shown in Table 3.6. In the first five cycles, coupons were elongated and returned immediately to their original length. For the sixth cycle, coupons were loaded to an applied tension of 5.5 N and held at a constant extension for 2 minutes, after which they were returned to their original

length. This was done in order to observe stress relaxation under constant elongation. The seventh cycle was performed in the same way as the first five cycles. Five coupons were loaded; extension data was collected during the seven cycles and analysed as discussed in the following Chapter.

Table 3.6 Tensile test numbers for specific ligaments, coupons and cycles

Ligament	Coupon	Cycle 1	Cycle 2	Cycle 3	Cycle 4	Cycle 5	Cycle 6	Cycle 7
10x	101	101_1	101_2	101_3	101_4	101_5	101_6	101_7
	102	102_1	102_2	102_3	102_4	102_5	102_6	102_7
	103	103_1	103_2	103_3	103_4	103_5	103_6	103_7
	104	104_1	104_2	104_3	104_4	104_5	104_6	104_7
	105	105_1	105_2	105_3	105_4	105_5	105_6	105_7
20x	201	201_1	201_2	201_3	201_4	201_5	201_6	201_7
	202	202_1	202_2	202_3	202_4	202_5	202_6	202_7
	203	203_1	203_2	203_3	203_4	203_5	203_6	203_7
	204	204_1	204_2	204_3	204_4	204_5	204_6	204_7
	205	205_1	205_2	205_3	205_4	205_5	205_6	205_7
30x	301	301_1	301_2	301_3	301_4	301_5	301_6	301_7
	302	302_1	302_2	302_3	302_4	302_5	302_6	302_7
	303	303_1	303_2	303_3	303_4	303_5	303_6	303_7
	304	304_1	304_2	304_3	304_4	304_5	304_6	304_7
	305	304_1	304_2	304_3	304_4	304_5	304_6	304_7

3.3 Shear test apparatus

In this section, the appearance, operation and structures of the shear test apparatus are described. The shear test procedures are also be introduced, including mounting of the coupons, application of load and description of cycles applied to the samples.

3.3.1 In-plane shear test fixture

The design and dimensions of the apparatus used for performing in-plane shear tests appear in Figure 3.3.1.

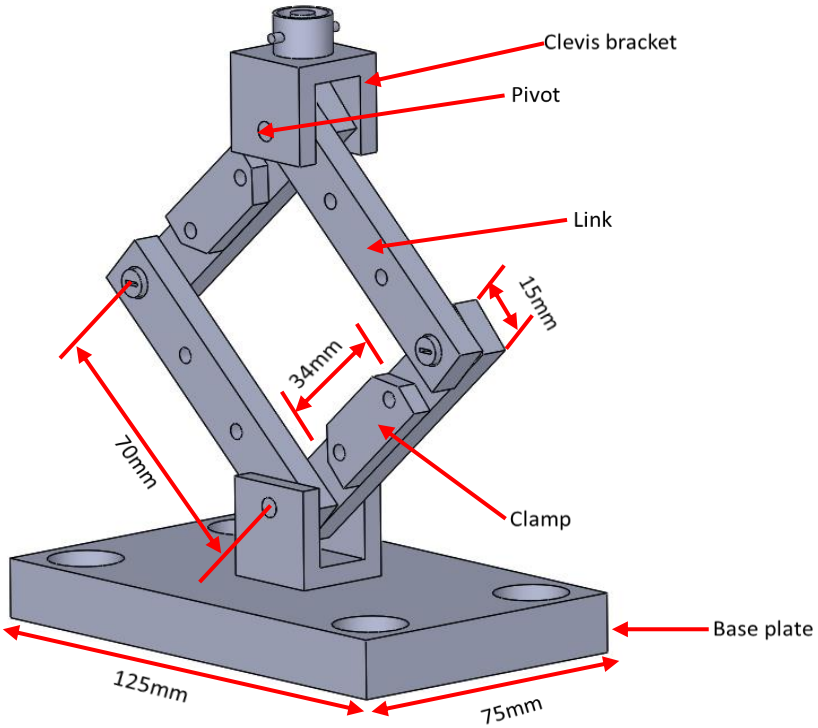

Figure 3.3.1 Construction and dimensions of in-plane shear testing apparatus [47]

The fixture consists of four pivoted links forming a variable-shape parallelogram. Two ball bearings are used at each pivot. The lower pivot is fixed in a clevis bracket, which is attached to the base plate and secured to the Instron 4482 universal testing frame through four set points. The upper pivot is connected to a second clevis bracket which is mounted onto a 10N load cell. Two clamps measuring 34mm by 15mm, mounted on each of two opposite links, are used for securing the coupon. The coupon is mounted between the clamps and links using two manually tightened screws at each clamp. The entire apparatus is made of aluminium. Prior to a test, the coupon is mounted between the two clamps, making the warp yarns in the coupon as parallel as possible to the other two links. As the distance between the two opposite pivots increases, a shear deformation is induced as shown in Figure 3.3.2.

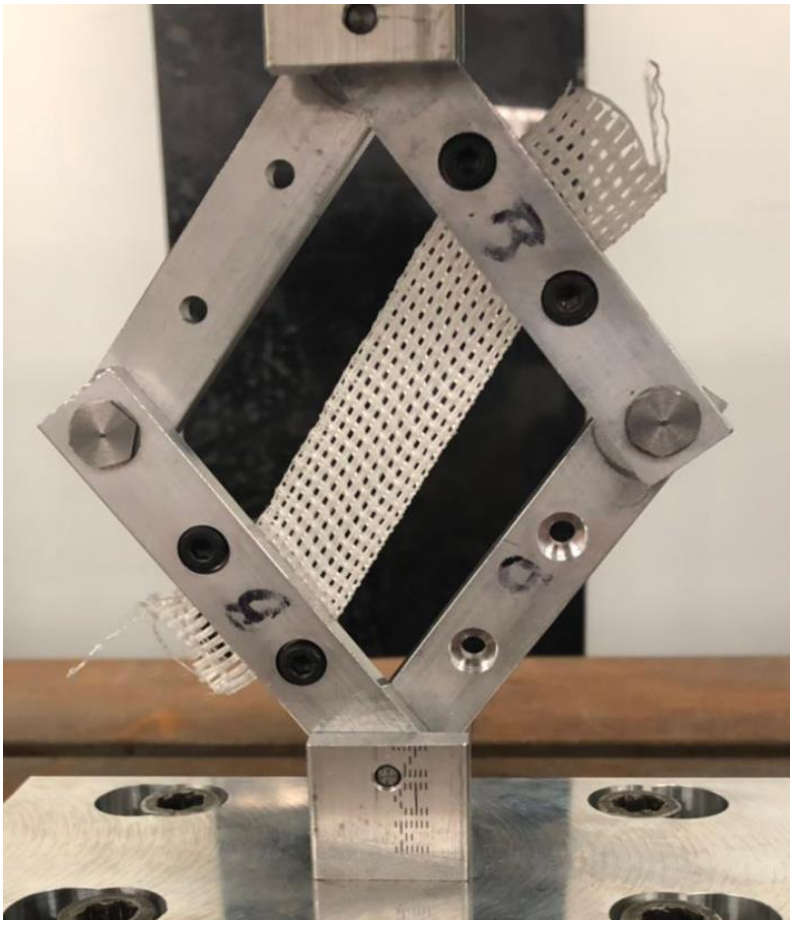

Figure 3.3.2 Shear deformation of coupon undergoing in-plane shear test

3.3.2 In-plane shear test procedures

Coupons used for tensile tests were also used in performing in-plane shear tests, as deformations induced in the coupons during tensile tests were mostly recoverable and had no perceivable influence on the behavior observed during in-plane shear tests. This decision to reuse the coupons was also made in view of the limited quantity of samples made available by the supplier. All tests were conducted using a displacement rate of 5mm/min for the vertical traverse of the Instron 4482 universal testing frame, until the vertical force applied on the apparatus and coupon reached 6.5 N to 8.0 N. Shear force increased significantly in the latter stages of deformation, hence it was necessary to set a fixed elongation for each coupon, making each cycle end at a variable load between 6.5 N to 8.0 N. Within this range, shear force was sufficiently large to enable analysis, while yarns did not break and the textile coupons did not undergo major, unrecoverable distortion. Because of this, the selected ranges of force and extension were appropriate for analysing the relationship between sheer deformation and shear force. Each coupon was subjected five shear cycles in total; each cycle had an identification number as shown in Table 3.7. The first one or two cycles aimed at finding an appropriate maximum extension, whilst for the next three or four cycles, the coupon was held at the same deformation for 5 minutes at maximum extension. After each cycle, the coupons were returned to their original configuration. The data collected is presented and analysed in Chapter 5.

Table 3.7 Shear test number for specific ligaments, coupons and cycles

Ligament	Coupon	Cycle 1	Cycle 2	Cycle 3	Cycle 4	Cycle 5
10x	101	101_1	101_2	101_3	101_4	101_5
	102	102_1	102_2	102_3	102_4	102_5
	103	103_1	103_2	103_3	103_4	103_5
	104	104_1	104_2	104_3	104_4	104_5
	105	105_1	105_2	105_3	105_4	105_5
20x	201	201_1	201_2	201_3	201_4	201_5
	202	202_1	202_2	202_3	202_4	202_5
	203	203_1	203_2	203_3	203_4	203_5
	204	204_1	204_2	204_3	204_4	204_5
	205	205_1	205_2	205_3	205_4	205_5
30x	301	301_1	301_2	301_3	301_4	301_5
	302	302_1	302_2	302_3	302_4	302_5
	303	303_1	303_2	303_3	303_4	303_5
	304	304_1	304_2	304_3	304_4	304_5
	305	304_1	304_2	304_3	304_4	304_5

3.3.3 Analysis of friction in in-plane shear rig

As the links of the in-plane shear test fixture are connected with ball joints, friction at the joints between links should be taken into consideration. Thus, prior to shear tests, pre-experiments were performed in order to analyse the influence generated by frictional forces within the fixture.

The fixture was mounted on the machine with no coupon on it, keeping the adjacent links perfectly perpendicular to each other. The displacement rate was set to 5mm/s, the same as used in the formal tests. Displacement was stopped and the fixture was returned to its original state from a specific displacement which was similar to the maximum extension used for most coupons during formal shear tests - the value is 15mm and as seen in Chapter 5. This procedure was repeated five times in trials labeled 1 to 5. The resulting load-extension curves are shown in Figures 3.3.3 to 3.3.7.

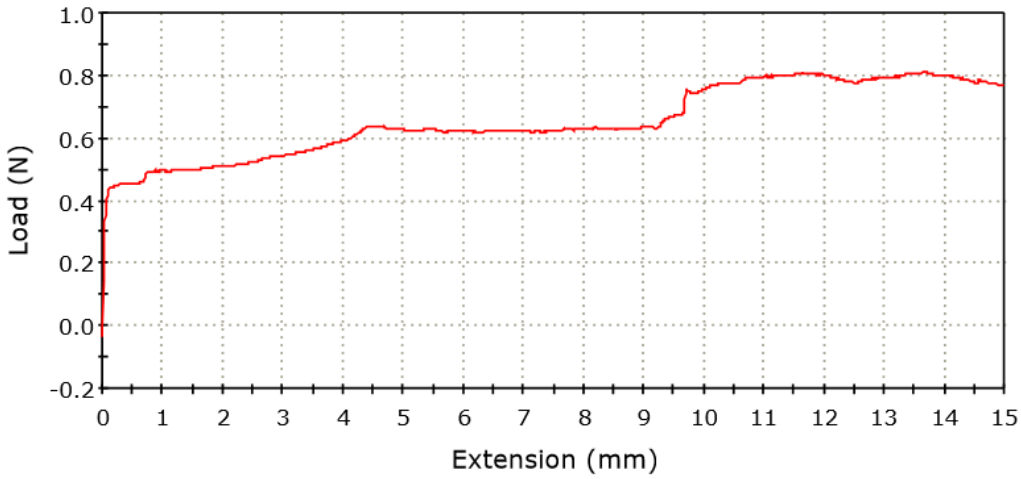

Figure 3.3.3 Load-extension curve, experiment 1

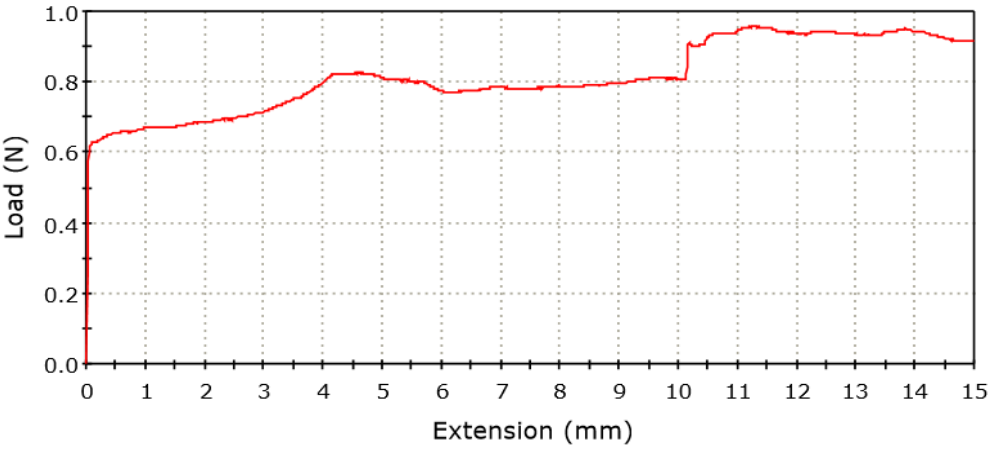

Figure 3.3.4 Load-extension curve, experiment 2

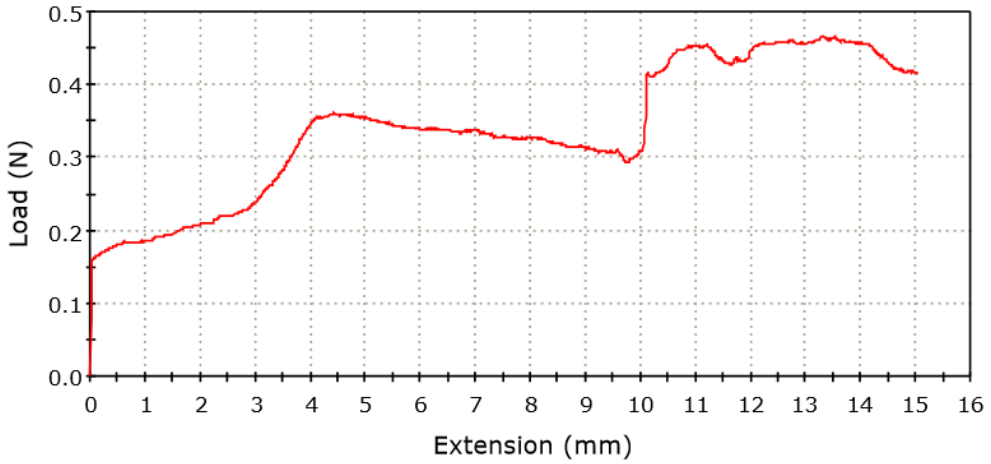

Figure 3.3.5 Load-extension curve, experiment 3

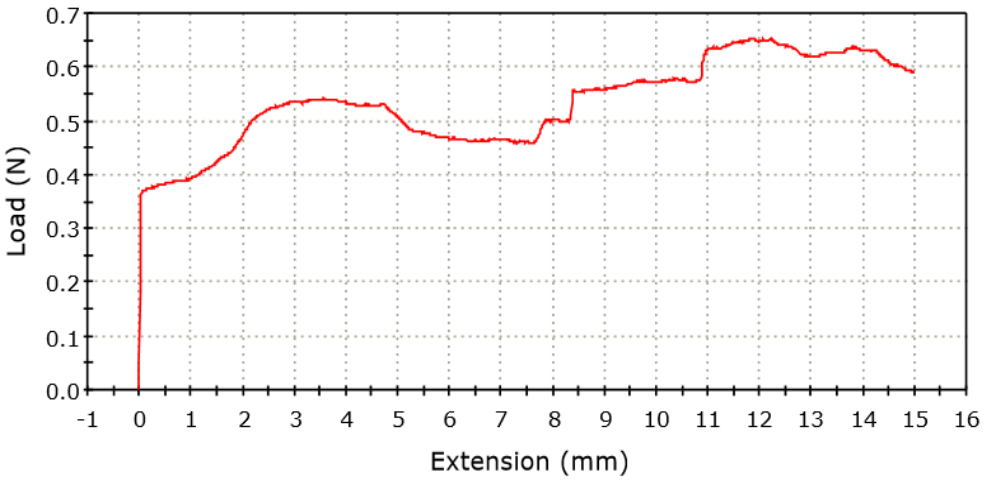

Figure 3.3.6 Load-extension curve, experiment 4

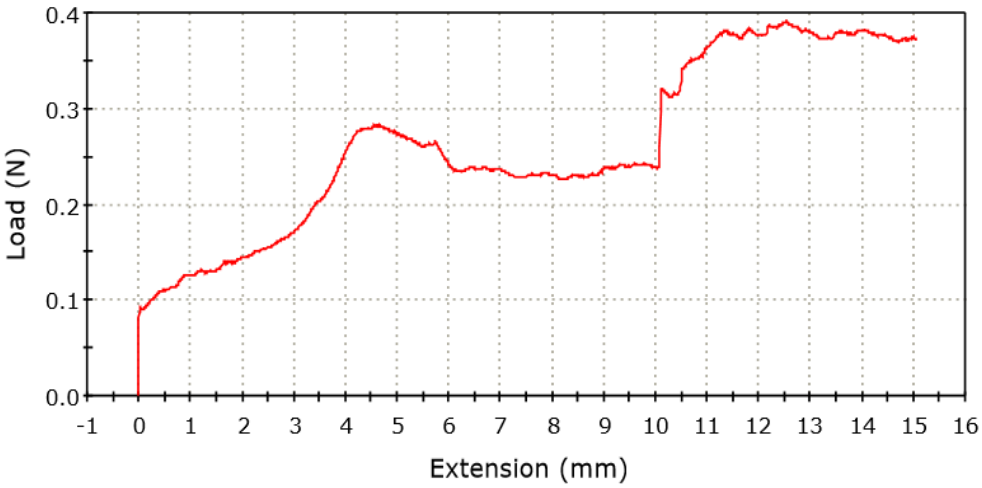

Figure 3.3.7 Load-extension curve, experiment 5

For the five curves, the maximum load was no more than 1N. Within a displacement range of 15mm, the maximum friction generated by the fixture itself is less than 1N. This value will be compared with the maximum load measured during shear tests reported in Chapter 5.

Chapter 4 –Experimental results: tensile tests

The raw data obtained from tensile tests consists of curves depicting the relationship between extension and load. These curves cannot be used directly for describing the mechanical properties of the textile ligaments. In order to analyze the tensile properties of the three samples quantitatively, extension-load curves were converted into strain-stress curves from tensile tests. In this chapter, the methods used for analyzing raw experimental data are described. The mechanical properties of the samples are presented, and the results are analysed in terms of trends and effect of different factors.

4.1 Raw tensile curves

As mentioned in the previous chapter, each textile ligament sample was divided into 5 coupons, and each coupon was cycled 7 times in tension. Each cycle was identified by a unique test number as listed in Table 3.6. For example, the test number of the second cycle performed on the first coupon for ligament 10x is 101_2.

Prior to performing the conversions, the raw data collected for all cycles and coupon were compared, based on the first and fifth cycles. Typical results appear in Figure 4.1.1.

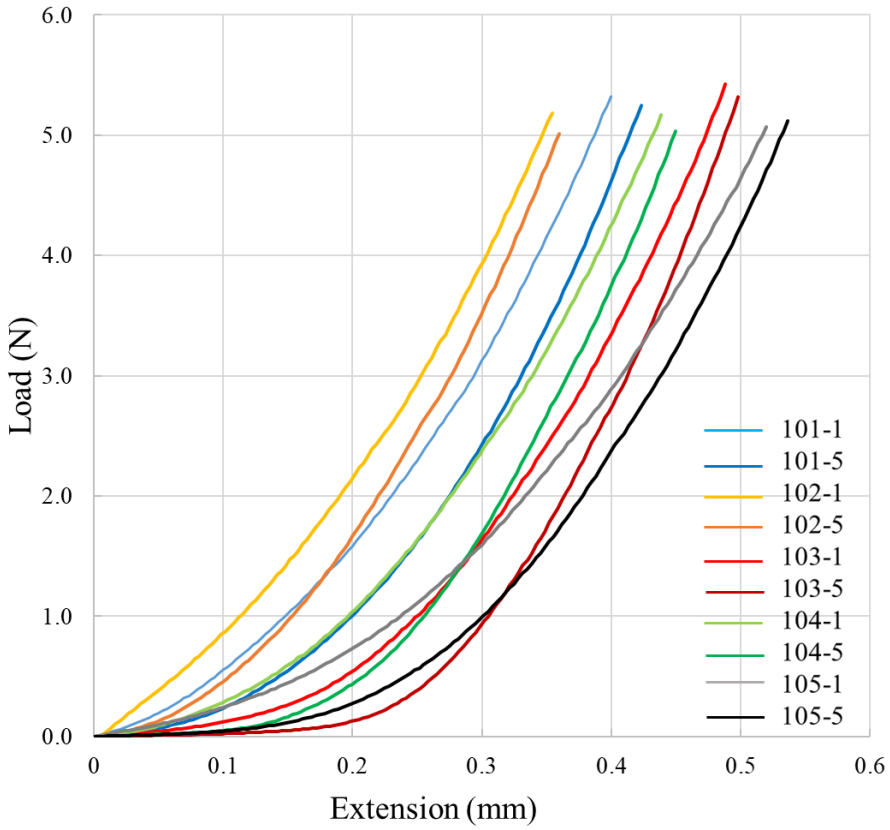

Figure 4.1.1 Raw tensile data, 1st and 5th cycles for all 10x coupons

Figure 4.1.1 shows a number of important elements of information. Firstly, all curves are non-linear, with stiffness increasing with load and with extension. It is seen that this increase is more progressive on the first cycle, whilst it is delayed but more sudden on the last cycle. This type of behaviour is fairly typical for textile structures made of elastic fibres. The increase in stiffness can be associated with a straightening of the yarns and a reduction in yarn crimp as the textile is extended, whilst the delay observed on latter cycles can be associated with a reorganization of fibres in the textile upon cycling. Secondly, the curves show that for a given coupon, the curve for cycle 5 always shows greater extension at a given level of force than the curve for cycle 1. This trend was consistent and as mentioned above, it was expected. Thirdly, whilst the general shape of all curves was similar as expected, the curves did not superimpose

at all for the same cycle number. In fact, differences between curves were larger when comparing the curves obtained from different coupons and the same cycle, than for curves obtained from the same coupon but different cycles. This was unexpected, as all curves were generated from coupons extracted from the same ligament, and tested using the same procedure. Similar behaviour and similar differences were observed for ligaments 20x and 30x: the curves were generally similar, and curves for cycle 5 were shifted to the right of curves for cycle 1; however, here again the curves for the same cycles did not superimpose.

In order to identify the source of this difference, another series of tests was performed. A coupon was mounted in the apparatus and tested for one cycle with the same method, then the coupon was removed, and the machine was shut down. After a short while, the same coupon was mounted again in the apparatus, and tested again. These operations were repeated three times, leading to three curves for each coupon. Typical results appear in Figure 4.1.2.

Clear differences were visible in the results, indicating that the mounting of coupons in the grips did have a clearly visible influence on the results. Because of the nature of textiles and relatively large size of textile repeating unit cells in this specific case, warp and weft yarns move easily upon handling, making it difficult to align them with the testing axis and to keep the coupons in the same initial state when removing and mounting them in the apparatus. However, the slopes of all curves, which are proportional to stiffness, look similar at the same given load level. This indicated that comparing moduli at different points of the curves corresponding to a constant load level is a more meaningful way to assess the tensile behaviour.

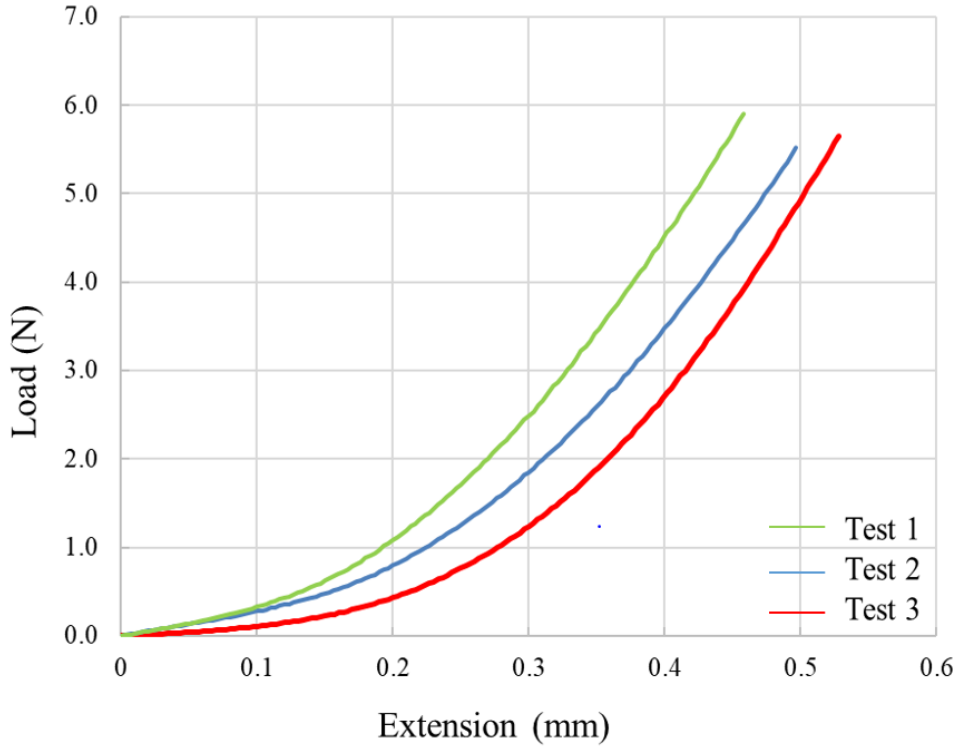

Figure 4.1.2 Effect of successive mounting and unmounting on tensile behaviour, for the same coupon

4.2 Tensile data conversion

In order to extract moduli from the raw curves, extension and load were converted into strain and stress, respectively. The former conversion was done first. In tensile tests, the initial gauge length of the coupons was 75mm. Extension can be calculated using Equation 4.1:

$$\varepsilon = \Delta L / L \tag{4.1}$$

Using this equation, all extension data points in raw tensile curves were divided by 0.075m.

The relationship between load F and stress σ is given by Equation 4.2:

$$\sigma = F/A \tag{4.2}$$

where σ is the normal stress under tension, F is the tensile load and A represents the cross-sectional area of all the fibres that sustain tension in the coupon. This value of A was selected for two reasons. Firstly, the notion of a precise cross-section for an open textile sample, and for yarns, are moot as these cross sections cannot be defined precisely. Conversely, the cross-section area of all fibres sustaining tension in the samples can be defined with satisfactory accuracy. Secondly, reporting stresses to the cross-section of the fibres enables comparisons with the properties of the fibres themselves. As a result, any changes in stiffness can be discussed as purely the effect of the textile structure.

Obtaining the value of A was mandatory. As the samples are very thin textiles with uneven thickness, measuring the cross-sectional area of coupons directly is difficult and not highly meaningful. Considering that the coupons are textiles featuring warp and weft yarns, and that in tensile tests only the warp yarns bear the tensile load, the cross-sectional area of fibres in warp yarns only was needed in this case. The proportion of warp yarns is calculated by measuring the mass of warp yarns and weft yarns respectively, which is around 59% for series 10x, 58% for series 20x and 76% for series 30x. Hence the cross-section of only warp yarns only in the coupons was considered. The relationship between load F and stress σ is shown in Equations 4.3 to 4.5:

$$V = P_{warp} m/\rho \tag{4.3}$$

$$A = V/L' \tag{4.4}$$

$$\sigma = FL'\rho/P_{warp} m \tag{4.5}$$

where V is the volume of all warp fibres in the coupon, P_{warp} is the proportion of warp yarns within a coupon, m is the mass of the coupon, ρ is the density of the constituent fibres and L' is full length of the coupon. The tensile stress σ can be calculated from the load F, only if the density of the fibres and mass of the sample are known. The masses of 15 coupons, or 5 coupons for each sample, appear in Table 3.5.

The second quantity to be documented is the density of the constituent material of the fibres. Table 4.1 lists values of the density of PET fibres collected from a number of reliable sources.

Table 4.1 Density of PET fibres

Density (g/cm^3)		
1.3~1.6 [48]	1.32~1.578 [49]	1.37~1.46 [50]

In order not to underestimate the tensile stress imposed on the fibres, the average of the three highest density values were used in the calculation of the effective density value used, Equation 4.4.

$$(1.6 + 1.578 + 1.46)/3 = 1.546 \text{ g/cm}^3 \quad (4.4)$$

Young's modulus of PET fibres was also documented as shown in Table 4.2. This data will prove useful upon modelling, as it will provide a basic value when calculating the tensile stiffness of the samples.

Table 4.2 Young's Modulus of PET fibres

Young's Modulus	
2.0~12.0 GPa[51]	98~112 g/d[52]

The units of g/d can be converted into GPa through Equation 4.5:

$$1g/d = 0.882 \times 0.0098 \times \rho \ \ GPa = 0.086436 \times \rho \ \ GPa \quad (4.5)$$

hence the range of Young's moduli in the second column is 8.47~9.68 GPa. Large ranges are not unexpected for fibres. Contrary to bulk thermoplastics, fibres experience stretching to different levels when they are manufactured. Stretching aligns the thermoplastic molecules in the direction of the fibres to different extents, hence more stretching will lead to higher longitudinal moduli. In any case, the moduli of thermoplastic fibres will typically be substantially higher than the moduli of the bulk thermoplastic from which they are made.

4.2.1 Analysis of results

Stress-strain curves for ligament series 10x are shown in Figures 4.2.3 to 4.2.7. By observing the curves, it can be seen that as the cycle number increases, the curves have a tendency to shift to the right, which means that under the same stress, the strain tends to be higher in successive cycles. As the cycles progressed, yarns gradually reorganized within the coupons.

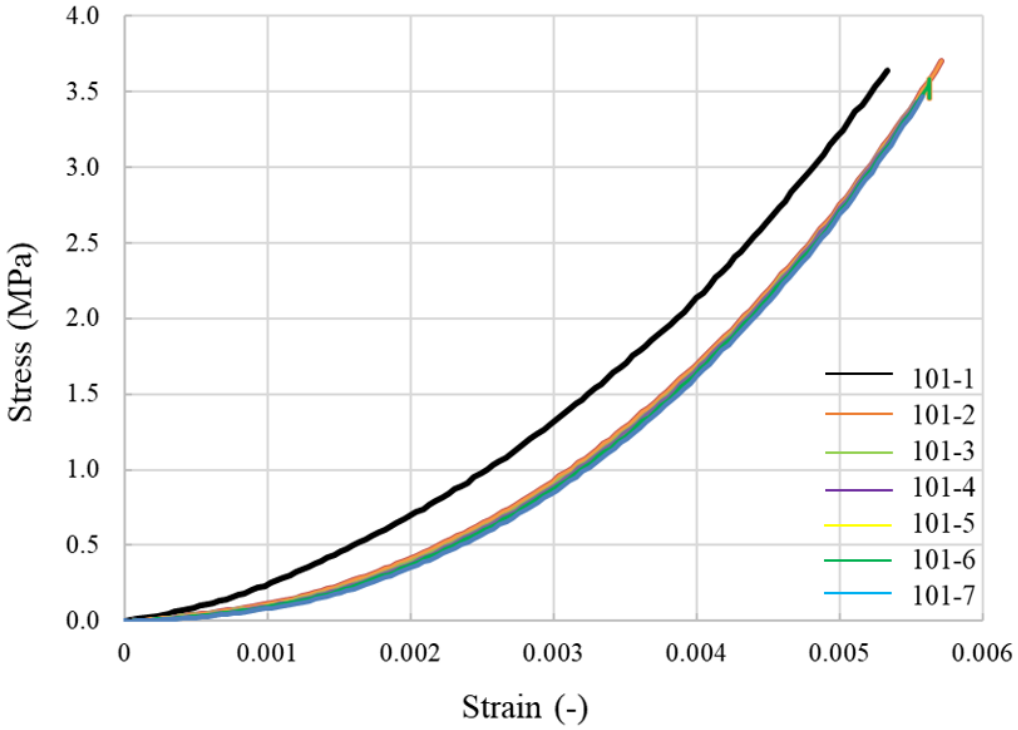

Figure 4.2.3 Tensile test results for coupon 101

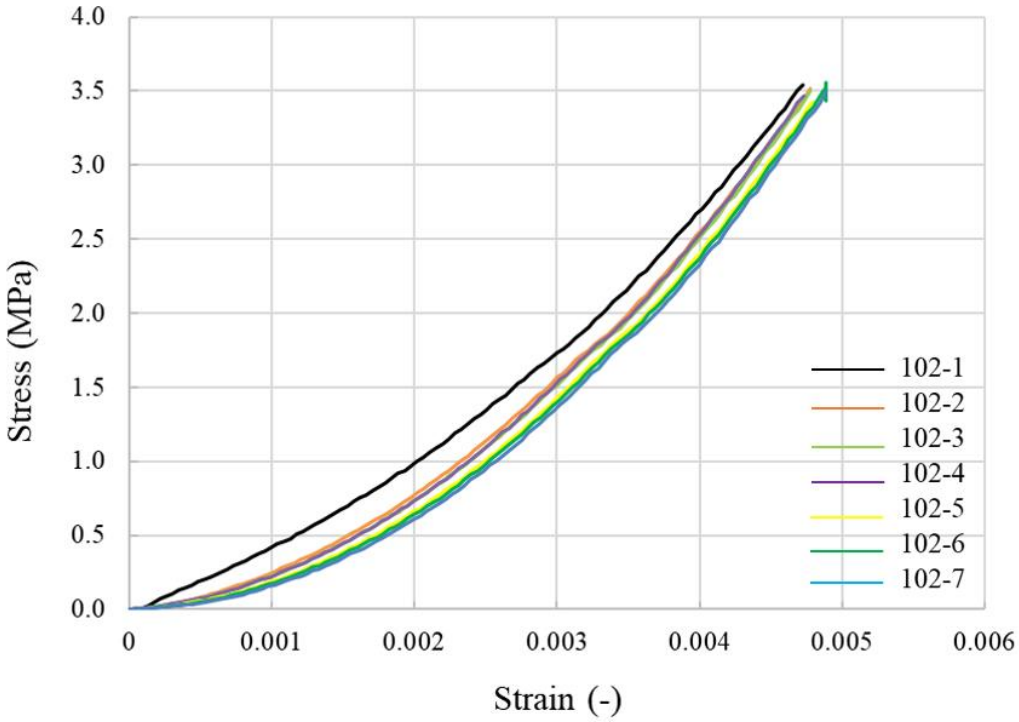

Figure 4.2.4 Tensile test results for coupon 102

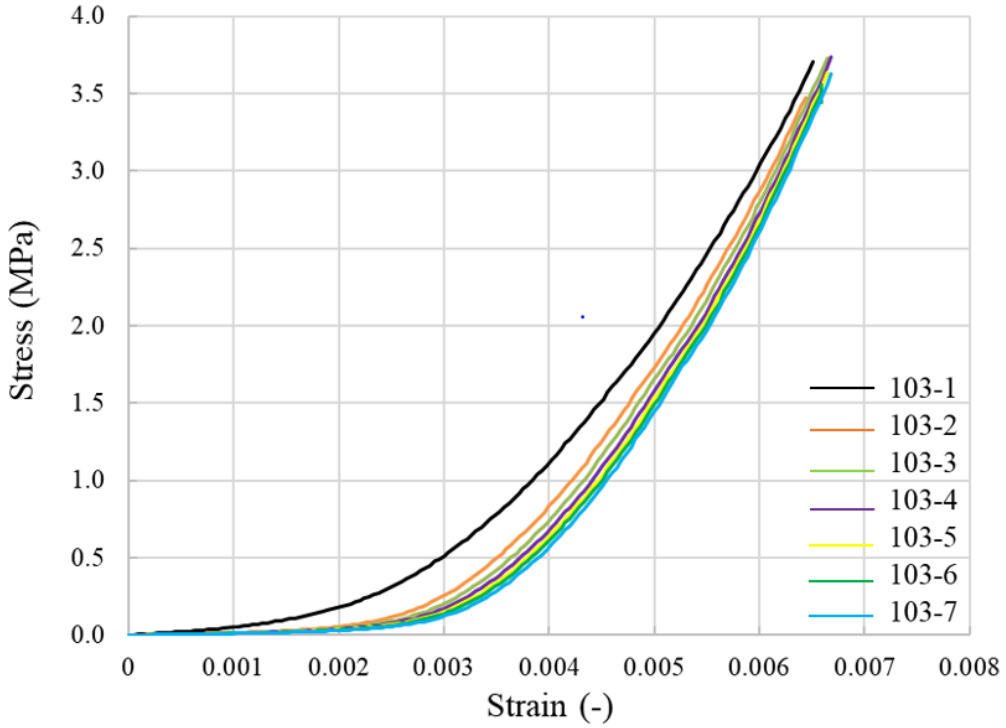

Figure 4.2.5 Tensile test results for coupon 103

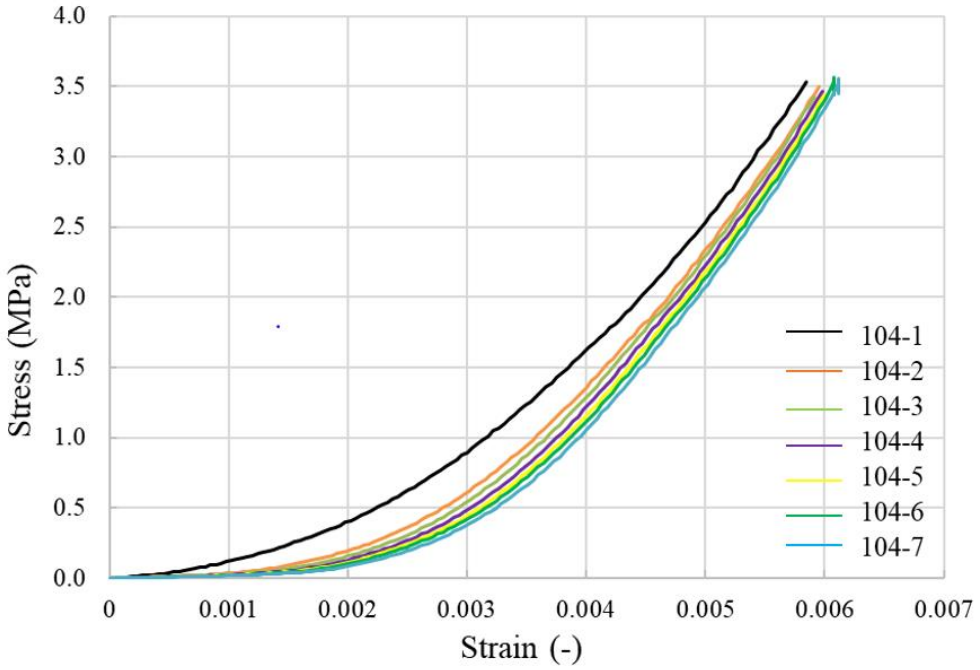

Figure 4.2.6 Tensile test results for coupon 104

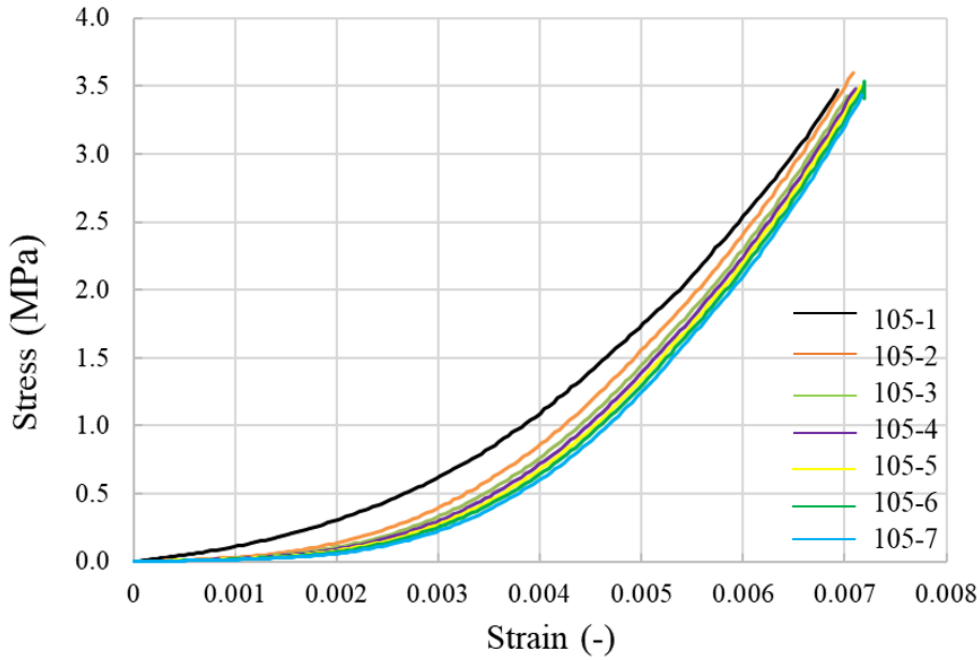

Figure 4.2.7 Tensile test results for coupon 105

As most of the above curves end at a tensile stress around 3.6 MPa, three stress levels were chosen for analysing the evaluation of tensile stiffness for each curve, at 1.2 MPa, 2.4 MPa and at the maximum tensile stress reached. The slope of the tangent to the curve at each stress level is the corresponding tensile stiffness, which can be calculated using Equation 4.7:

$$E = \sigma/\varepsilon \tag{4.7}$$

To minimize error, ten points on each curve closest to the chosen stress levels were picked in order to calculate the tensile stiffness. Table 4.3 shows tensile stiffness values at the chosen three stress levels for coupon series 10x.

A number of consistent observations can be made from Table 4.4. Firstly, the tensile stiffness increases as the stress increases, and reaches a maximum around 1350 MPa at maximum stress. This increase occurs because at low stress levels, yarns are bent and show lesser stiffness, while at high stress levels, yarns are straightened and show higher stiffness. This is an effect of the textile structure.

When comparing stiffness values observed for seven consecutive cycles on the same coupon, the standard deviation is relatively low at within 100 MPa, compared with the average modulus around 1000 MPa. Besides, as the number of cycles increases, the tensile stiffness at the three chosen stress levels rises moderately. This is the result of the gradual extension of the yarns and reorganization of fibres within yarns. When comparing the behaviour of five coupons, the

average moduli at three chosen stress levels are not same, but they are fairly similar. This can be explained by difference in which coupons were mounted.

Table 4.3 Tensile stiffness for coupon series 10x

Tensile stiffness for coupon 101 (MPa)									
	101-1	101-2	101-3	101-4	101-5	101-6	101-7	Average	Standard deviation
1.2 MPa	688.5	752.9	749.5	753.0	756.8	758.7	773.4	747.6	25.1
2.4 MPa	1032.5	1115.4	1112.1	1118.7	1110.1	1148.1	1129.3	1109.5	33.7
Max	1230.2	1384.3	1331.8	1336.0	1380.3	1445.1	1388.5	1356.6	62.3
Tensile stiffness for coupon 102 (MPa)									
	102-1	102-2	102-3	102-4	102-5	102-6	102-7	Average	Standard deviation
1.2 MPa	722.8	806.1	823.9	832.3	832.2	847.5	849.8	816.4	40.5
2.4 MPa	1027.3	1121.9	1154.2	1167.7	1190.1	1193.9	1196.0	1150.1	55.8
Max	1226.0	1284.5	1319.5	1312.1	1332.7	1391.4	1345.4	1315.9	47.7
Tensile stiffness for coupon 103 (MPa)									
	103-1	103-2	103-3	103-4	103-5	103-6	103-7	Average	Standard deviation
1.2 MPa	767.1	907.1	932.8	939.5	961.3	961.7	977.5	921.0	66.4
2.4 MPa	1075.4	1182.9	1216.8	1232.7	1248.9	1288.9	1307.3	1221.8	71.3
Max	1349.9	1412.0	1501.0	1522.4	1524.9	1523.5	1536.4	1481.5	66.4
Tensile stiffness for coupon 104 (MPa)									
	104-1	104-2	104-3	104-4	104-5	104-6	104-7	Average	Standard deviation
1.2 MPa	726.8	835.6	866.8	910.8	929.4	940.2	939.2	878.4	71.8
2.4 MPa	1022.0	1121.5	1121.5	1144.3	1181.8	1173.9	1178.6	1134.8	51.9
Max	1234.7	1311.1	1352.8	1397.9	1397.3	1493.0	1509.3	1385.2	89.8
Tensile stiffness for coupon 105 (MPa)									
	105-1	105-2	105-3	105-4	105-5	105-6	105-7	Average	Standard deviation
1.2 MPa	602.9	712.4	728.4	744.8	746.1	746.9	771.3	721.8	51.4
2.4 MPa	872.2	969.3	995.2	1010.4	1024.5	1019.4	1060.3	993.0	55.6
Max	1077.2	1196.7	1180.1	1221.2	1237.4	1326.1	1242.1	1211.5	69.8

The tensile results of series 20x are shown in Figures 4.2.8 to 4.2.12.

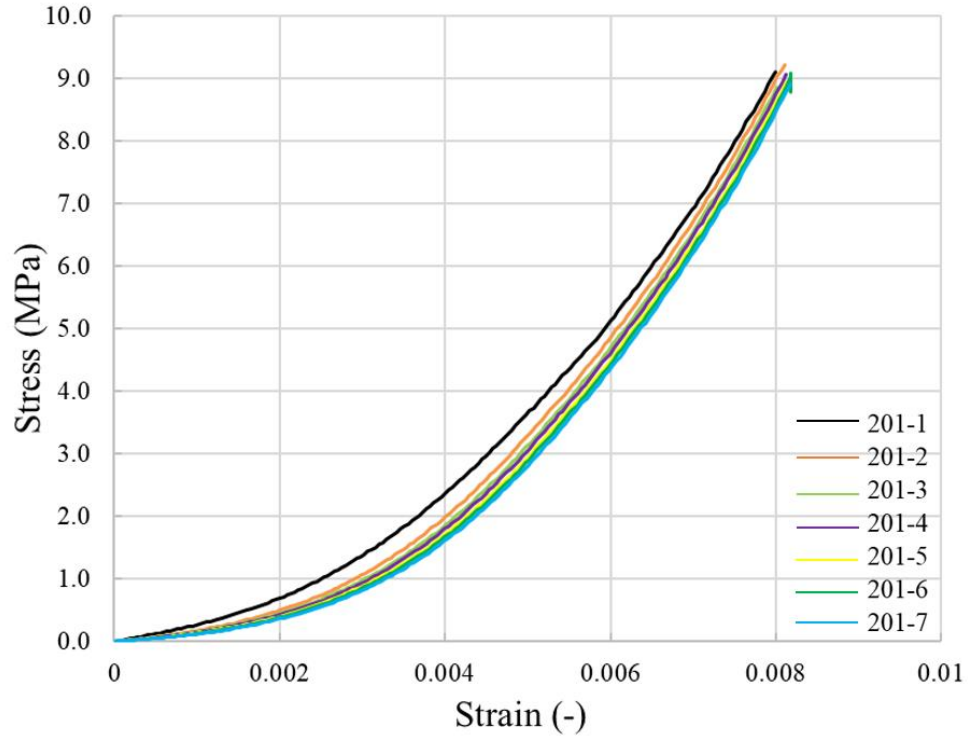

Figure 4.2.8 Tensile test results for coupon 201

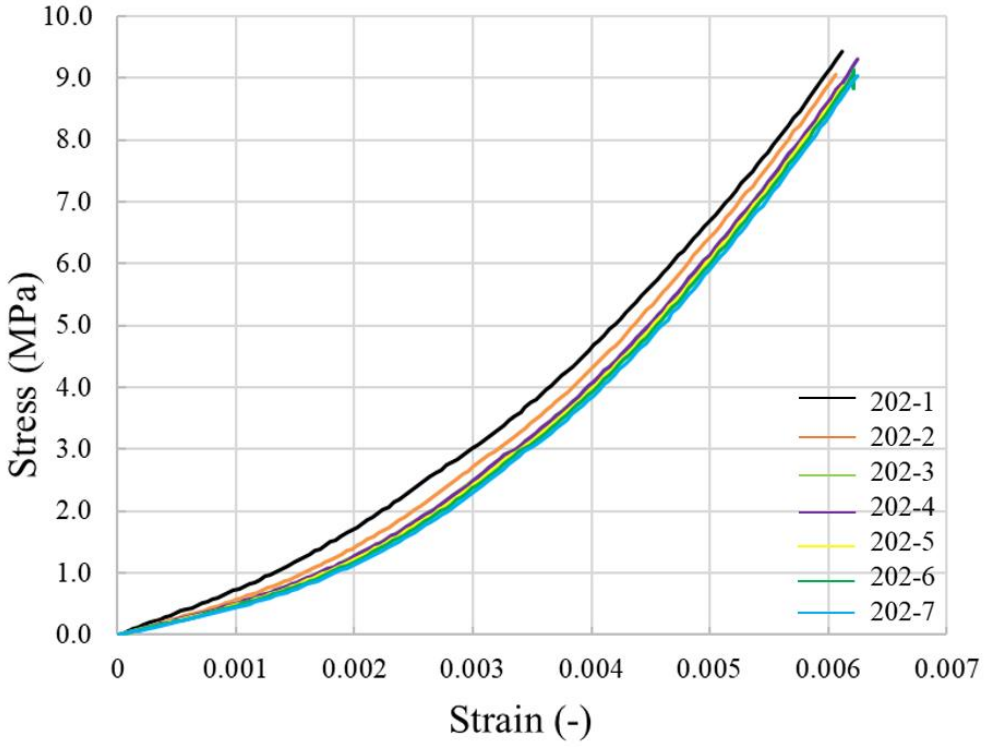

Figure 4.2.9 Tensile test results for coupon 202

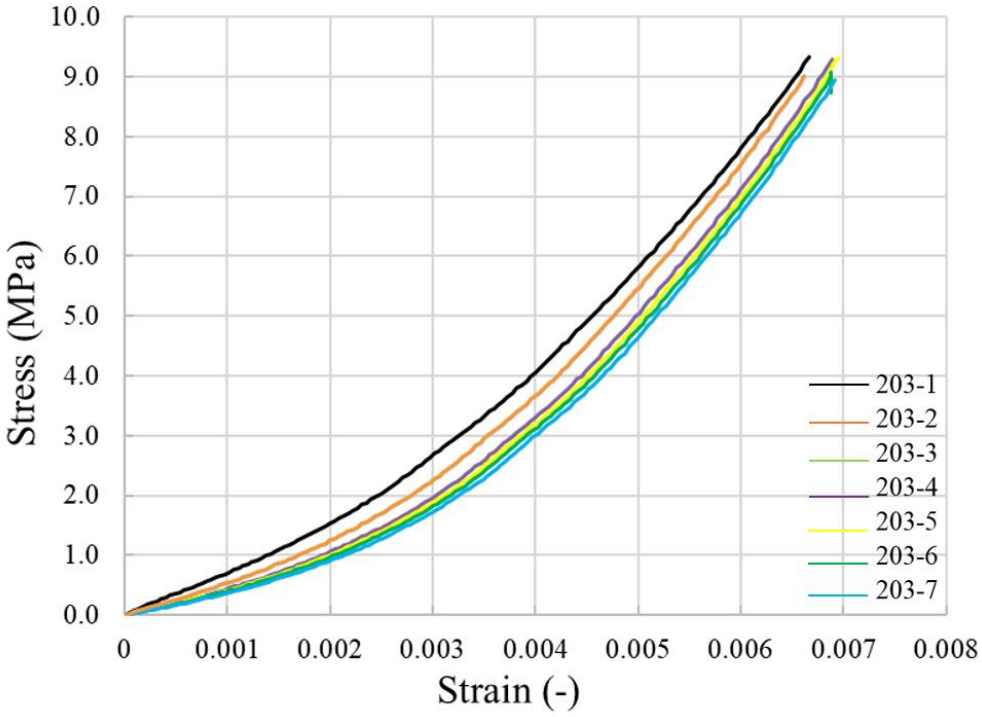

Figure 4.2.10 Tensile test results for coupon 203

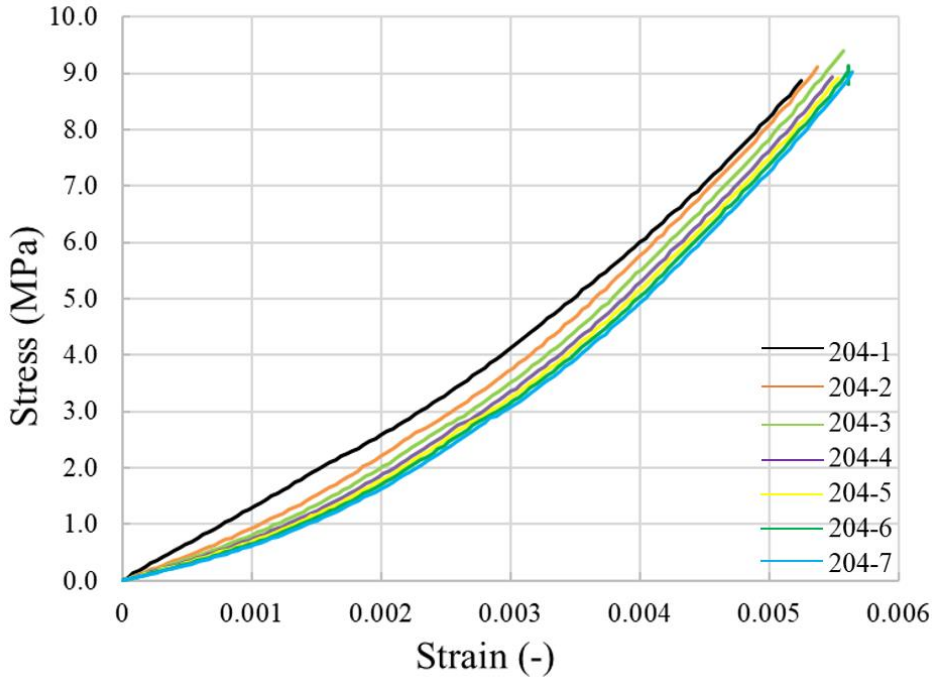

Figure 4.2.11 Tensile test results for coupon 204

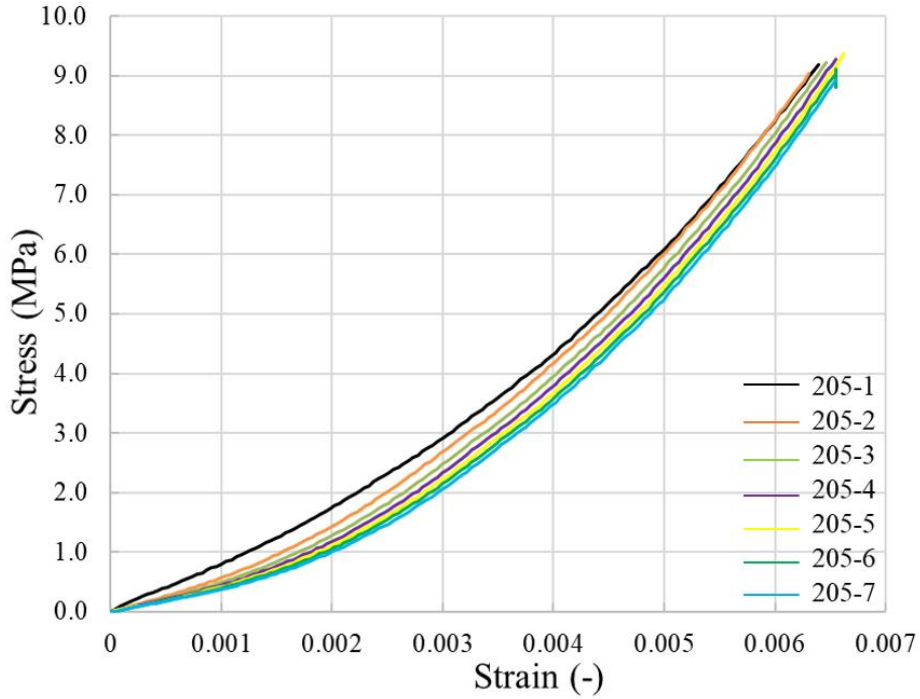

Figure 4.2.12 Tensile test results for coupon 205

Similarly to coupons 10x, the stress-strain curves for series 20x also show a trend where they move to the right as the number of the cycles increases. However, the stress reached around 9 MPa, higher than seen with series 10x. This resulted as for all three ligament types, tests were limited to a maximum force of 5.5N. As series 20x samples are narrower than series 10x samples, the stress in 20x is higher under the same force. The same procedure described above was used for analysing the tensile stiffness for series 20x coupons. In this case, as most curves ended at stress levels around 9 MPa, the three stress levels chosen to analyse tensile stiffness were 3 MPa, 6 MPa and the maximum. Using the same equation, elastic stiffness for series 20x coupons appear in Table 4.4.

Table 4.4 Tensile stiffness for coupon series 20x

Tensile stiffness for coupon 201 (MPa)									
	201-1	201-2	201-3	201-4	201-5	201-6	201-7	Average	Standard deviation
3 MPa	1307.6	1427.9	1451.4	1445.5	1472.8	1474.6	1469.3	1435.6	54.6
6 MPa	1813.0	1902.7	1936.6	1953.8	1961.9	1985.4	1965.5	1931.3	54.0
Max	2313.6	2412.2	2401.7	2453.4	2449.7	2594.1	2526.8	2450.2	83.7
Tensile stiffness for coupon 202 (MPa)									
	202-1	202-2	202-3	202-4	202-5	202-6	202-7	Average	Standard deviation
3 MPa	1333.4	1356.4	1364.6	1371.4	1401.3	1408.5	1404.9	1377.2	26.4
6 MPa	2115.4	2244.7	2283.4	2280.6	2291.2	2285.7	2330.7	2261.7	64.1
Max	2648.2	2612.9	2615.3	2733.0	2659.4	2835.1	2724.1	2689.7	74.0
Tensile stiffness for coupon 203 (MPa)									
	203-1	203-2	203-3	203-4	203-5	203-6	203-7	Average	Standard deviation
3 MPa	1310.8	1420.2	1448.0	1413.0	1389.7	1421.7	1449.9	1407.6	43.9
6 MPa	1866.5	1987.0	1987.0	2064.7	2077.7	2113.6	2142.3	2034.1	87.3
Max	2347.9	2401.5	2401.5	2564.0	2637.2	2703.3	2543.2	2514.1	123.8
Tensile stiffness for coupon 204(MPa)									
	204-1	204-2	204-3	204-4	204-5	204-6	204-7	Average	Standard deviation
3 MPa	1471.3	1518.1	1510.6	1470.3	1440.2	1427.8	1453.6	1470.3	31.4
6 MPa	2014.8	2234.5	2299.5	2292.4	2321.5	2320.1	2356.3	2262.7	106.9
Max	2529.1	2724.4	2762.6	2701.2	2718.6	2947.9	2802.1	2740.8	116.0
Tensile stiffness for coupon 205 (MPa)									
	205-1	205-2	205-3	205-4	205-5	205-6	205-7	Average	Standard deviation
3 MPa	1330.3	1363.6	1392.8	1401.2	1406.2	1407.8	1423.1	1389.3	29.4
6 MPa	1834.0	2036.1	2050.4	2129.4	2126.9	2145.2	2151.2	2067.6	104.3
Max	2369.0	2495.1	2579.4	2629.3	2677.2	2848.9	2658.4	2608.2	139.6

The average maximum tensile moduli for all coupons are around 2600 MPa, which is higher than the corresponding value observed with series 10x. This result came as a surprise, since visual observation of the ligaments reported in Chapter 3 showed similar structures for coupon series 10x and 20x. However, this can be tempered by considering that the stiffening samples were loaded to higher stress levels. Under 3 MPa, the tensile moduli for series 20x is around 1400 MPa, which is similar to tensile moduli for series 10x under around 3.6 MPa. Except for that difference, other features of the data generated for series 20x were similar to those seen for series 10x. The standard deviations and the differences between coupons were limited.

Figures 4.2.13 to 4.2.17 show the results of tensile tests for series 30x.

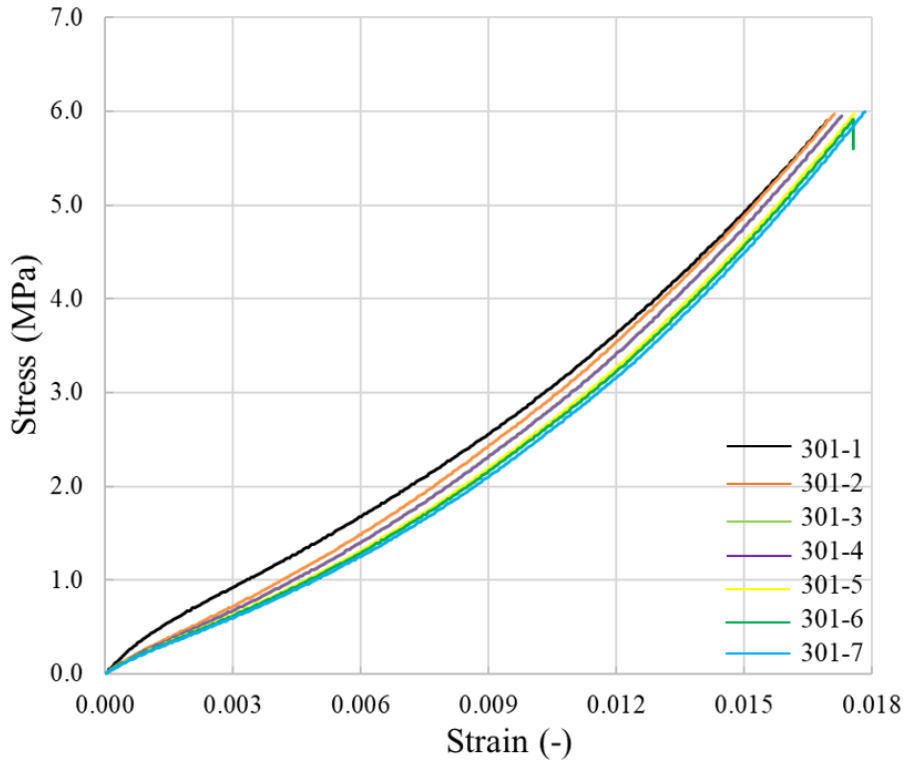

Figure 4.2.13 Tensile test results for coupon 301

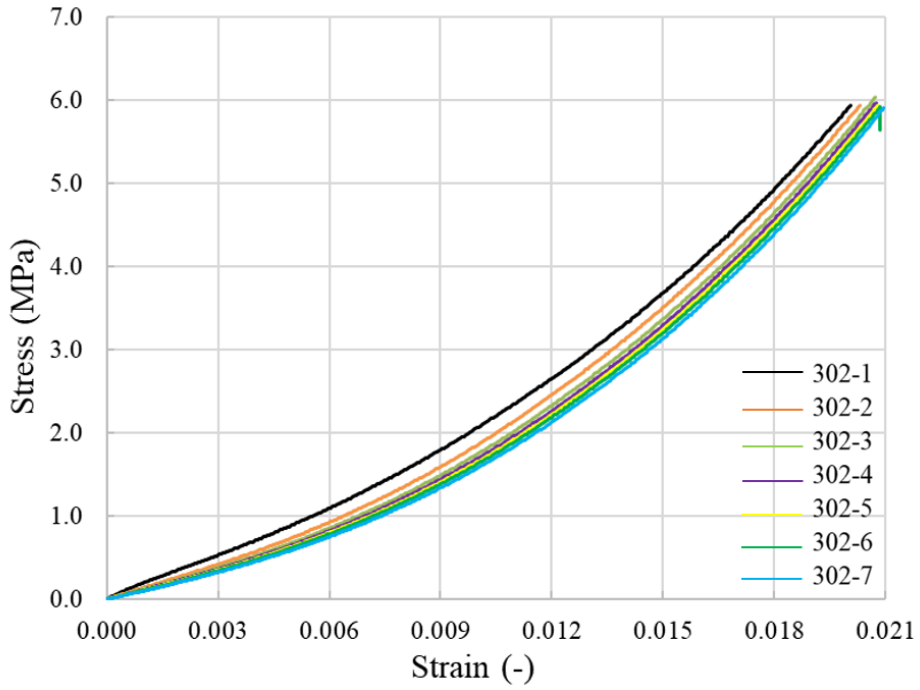

Figure 4.2.14 Tensile test results for coupon 302

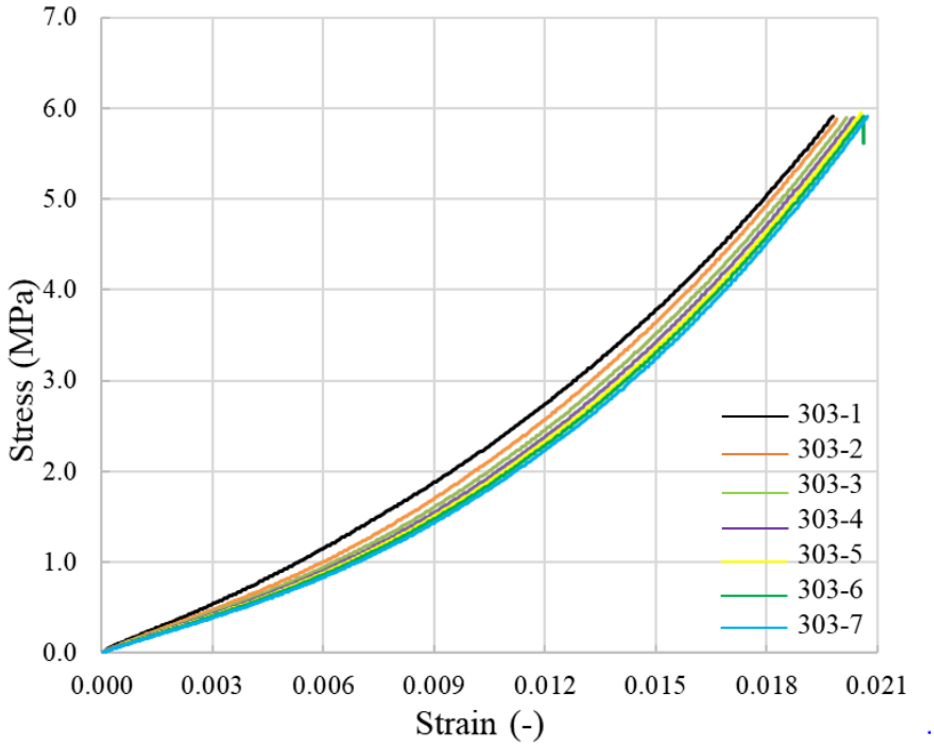

Figure 4.2.15 Tensile test results for coupon 303

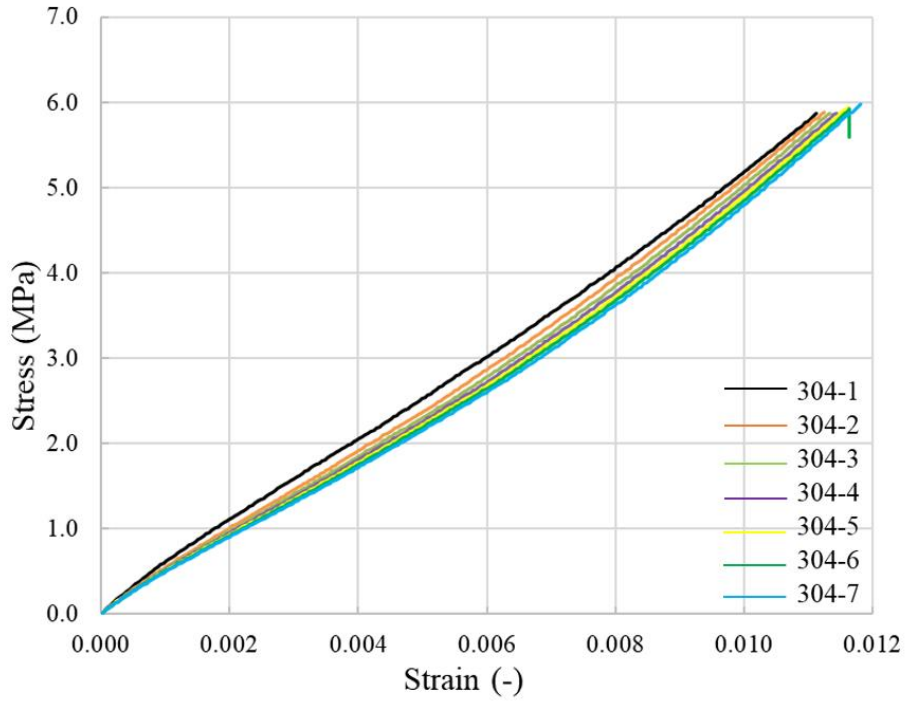

Figure 4.2.16 Tensile test results for coupon 304

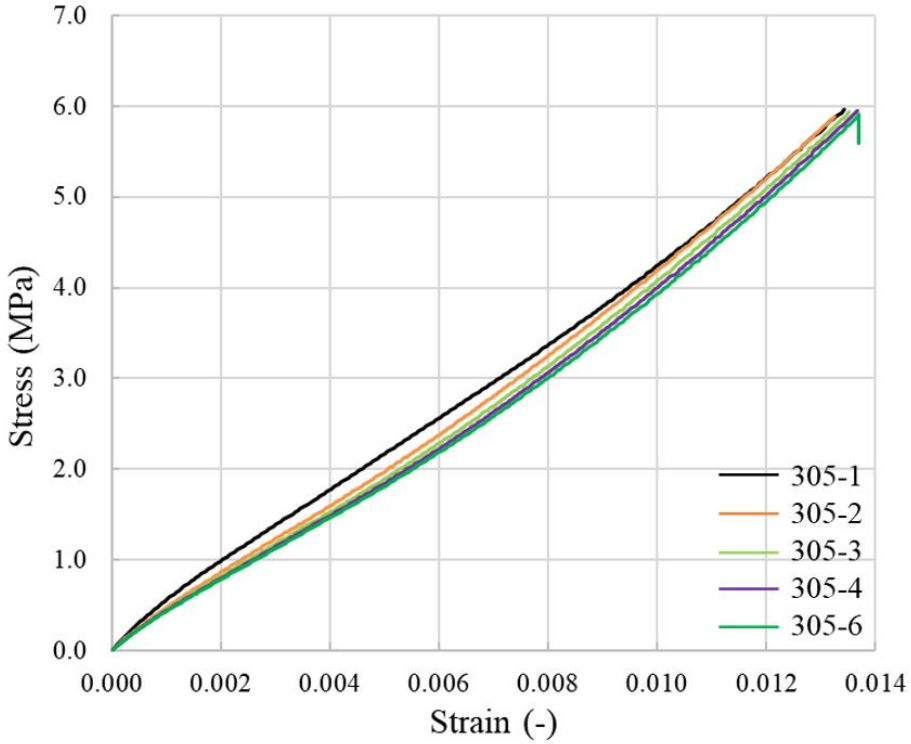

Figure 4.2.17 Tensile test results for coupon 305

One apparent difference observed with series 30x coupons is that the curves are generally more linear than those obtained for coupon series 10x and 20x, meaning that the tensile stiffness does not change as dramatically over the loading domain. This occurred because samples 30x are denser, reducing the potential for yarn reorganization within the textile samples. The yarns have less freedom for reorganizing and realigning compared to the other two ligament types, and the warp yarns are better kept straight. Maximum stresses observed were around 6 MPa hence three stress levels at 2 MPa, 4 MPa and the maximum were chosen to calculate the tensile stiffness. The results appear in Table 4.5.

As mentioned earlier, the average tensile stiffness recorded at the three stress levels showed generally less relative increase when compared with coupon series 10x and 20x. The dense textiles also caused the tensile stiffness to increase relatively less upon successive cycles. For example, for coupon 302, the maximum stiffness value occurred on the sixth cycle at 560.3.1 MPa, rather than the last cycle at 552.3 MPa. Maximum tensile stiffness values were about 550 MPa, much lower than observed for series 10x and 20x. Because of the dense weave structure, more weft yarns are included into the fabric within the same length of the warp yarns, which cause more bends in the warp yarns. In their natural, unloaded state these warp yarns have less freedom to reorganize because they are crimped and held in place by the weft yarns prevent. But when the coupons are loaded, warp yarns under tension can straighten as the weft yarns are not loaded, hence they can withstand more elongation than those straighter warp yarns in coupon series 10x and 20x, as they can crimp and compact the weft yarns across them. Thus, coupon series 30x has lower but more consistent stiffness than series 10x and 20x.

Table 4.5 Tensile stiffness for coupon series 30x

Tensile stiffness for coupon 301 (MPa)									
	301-1	301-2	301-3	301-4	301-5	301-6	301-7	Average	Standard deviation
2 MPa	294.6	325.9	319.3	319.3	320.6	313.4	315.3	315.5	9.3
4 MPa	418.6	435.5	446.9	446.9	456.4	454.2	459.3	445.4	13.2
max	523.3	542.6	539.8	539.8	550.6	555.3	561.9	544.8	11.7
Tensile stiffness for coupon 302 (MPa)									
	302-1	302-2	302-3	302-4	302-5	302-6	302-7	Average	Standard deviation
2 MPa	277.4	293.9	295.7	291.9	287.9	295.4	294.8	291.0	6.1
4 MPa	397.1	417.9	419.2	432.7	428.3	431.9	434.3	423.0	12.2
max	513.0	531.9	544.9	551.2	542.5	560.3	552.3	542.3	14.5
Tensile stiffness for coupon 303 (MPa)									
	303-1	303-2	303-3	303-4	303-5	303-6	303-7	Average	Standard deviation
2 MPa	269.8	289.0	289.8	286.5	291.4	286.1	288.6	285.9	6.8
4 MPa	385.7	402.1	422.5	416.0	428.2	426.9	442.2	417.7	17.3
max	504.6	523.0	524.0	538.6	543.0	541.2	549.9	532.0	14.5
Tensile stiffness for coupon 304 (MPa)									
	304-1	304-2	304-3	304-4	304-5	304-6	304-7	Average	Standard deviation
2 MPa	452.0	460.0	454.5	450.4	450.2	443.5	438.1	449.8	6.6
4 MPa	531.9	568.9	574.5	580.4	562.9	579.1	584.1	568.8	16.5
max	631.2	640.0	642.0	649.2	649.4	682.1	667.3	651.6	16.2
Tensile stiffness for coupon 305 (MPa)									
	305-1	305-2	305-3	305-4		305-6		Average	Standard deviation
2 MPa	396.3	399.8	388.1	376.7		379.8		388.1	9.0
4 MPa	442.3	480.4	485.4	489.0		492.2		477.9	18.2
max	538.2	559.0	572.9	570.2		597.8		567.6	19.4

4.3 Conclusion

In light of the curves and tables above, many conclusions can be drawn. Firstly, the stress-strain curves of coupon series 10x, 20x and 30x all show a trend to move to the right and the tensile stiffness values increase moderately with the number of cycles because of the gradual extension and reorganization of the fibres, though the extent is different for the different series. Among them, series 30x has the highest curve coincidence and similar stiffness when comparing the seven cycles. Secondly, the appearance of 30x sample curves is different than for 10x and 20x sample curves. The stiffness of 30x sample does not increase as much as that of 10x and 20x under the three stress levels as the structure of samples 30x is denser than that of samples 10x and 20x. Thirdly, sample series 30x shows the lowest maximum tensile stiffness which is around 550 MPa. Under the same loading range, sample series 20x shows the highest maximum tensile stiffness at around 2600 MPa, which is twice as much as sample series 10x. This may be the result of the maximum stiffness of sample series 20x being calculated under tensile stresses around 9 MPa, while they are around 3.6 MPa for sample series 10x.

When comparing with real knee ligaments discussed referred in Chapter 2, all three sample groups show much higher tensile stiffness than real ligaments, which provide sufficient stiffness to repair broken ligaments. However, the overall cross-section of these artificial implantable textile ligaments is markedly smaller than that of natural ligaments; furthermore, stiffness values calculated in this work were calculated considering the cross section of the fibres loaded in tension only, for reasons stated above. This latter point will increase differences

between stiffness values reported here, and those measured for full-section real ligaments. Under low stress, the non-linear behaviour is comparable to that of real ligaments, hence they can replicate the behaviour of real ligaments well.

Chapter 5 –Experimental results: shear tests

The raw data from shear curves depicts the relationship between extension and load. In order to compare shear properties between the three textile samples, displacement-load curves were converted into shear angle-normalized force curves. In this Chapter, the methods used for converting raw data into normalized curves are described. The mechanical properties of the samples including shear stiffness, as well as trends and influencing factors, are analysed.

5.1 Raw shear curves

In a series of tests supplemental to tensile tests, each textile ligament sample was divided into 5 coupons, and each coupon was cycled 5 times in in-plane shear. Test and cycle numbers used for labelling same as used for tensile tests, as shown in Table 3.7. For example, the test number of the second cycle performed on the first coupon for ligament 10x is 101_2.

Prior to performing conversions of measured quantities, the raw data collected for all cycles and coupon were compared based on the 3rd and 5th cycles, as the first two cycles mainly settled the samples as discussed in Chapter 3. Typical results appear in Figure 5.1.1.

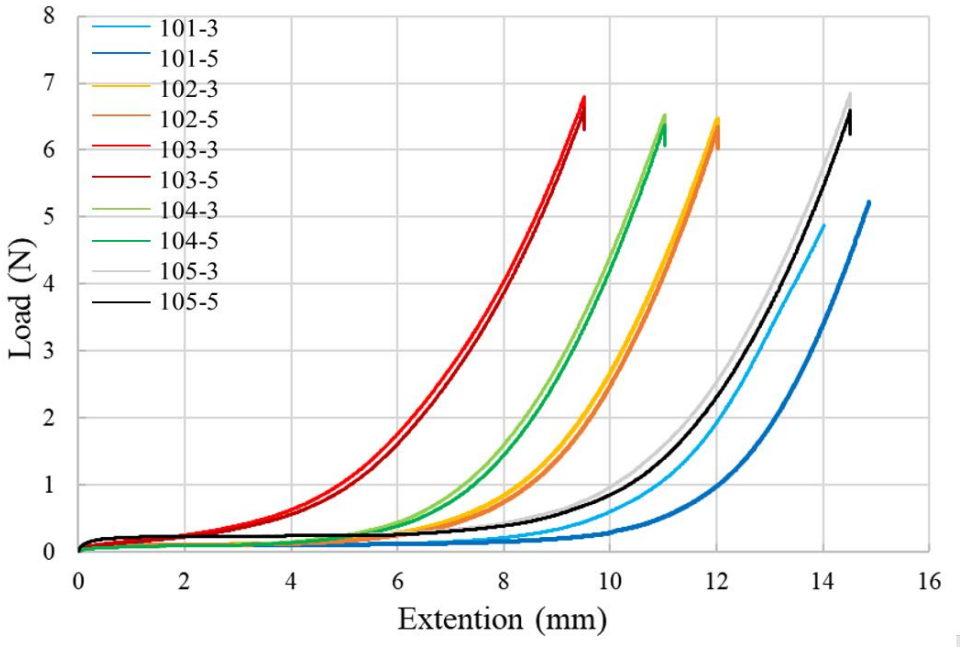

Figure 5.1.1 Raw shear data, 3rd and 5th cycles, for all 10x coupons

Figure 5.1.1 shows a number of important elements of information. Firstly, all curves are non-linear with slope increasing with load and with extension, similar to the trend observed with tensile results. Secondly, the curves show that for a given coupon, the curve for cycle 5 always shows greater extension at a given level of load than the curve for cycle 3; however, the difference is not as pronounced as it was for the curves for tensile results. Thirdly, although the general shape of all curves looks similar as expected, the curves do not superimpose at all for the same cycle number. Similarly to tensile curves, differences between curves obtained from different coupons but for the same cycle are larger than differences observed from same coupon but different cycles. This unexpected behaviour can be explained in the same way as it was for tensile tests, as discussed in Chapter 4.

5.2 Shear data conversion

In order to extract stiffness values from the raw curves, extension and load were converted into shear angle and normalized shear force, respectively. The former conversion was done first. The shear angle γ represents the change of the angle between warp and weft yarns after an imposed vertical displacement and resulting shear deformation, as shown in Figure 5.1.

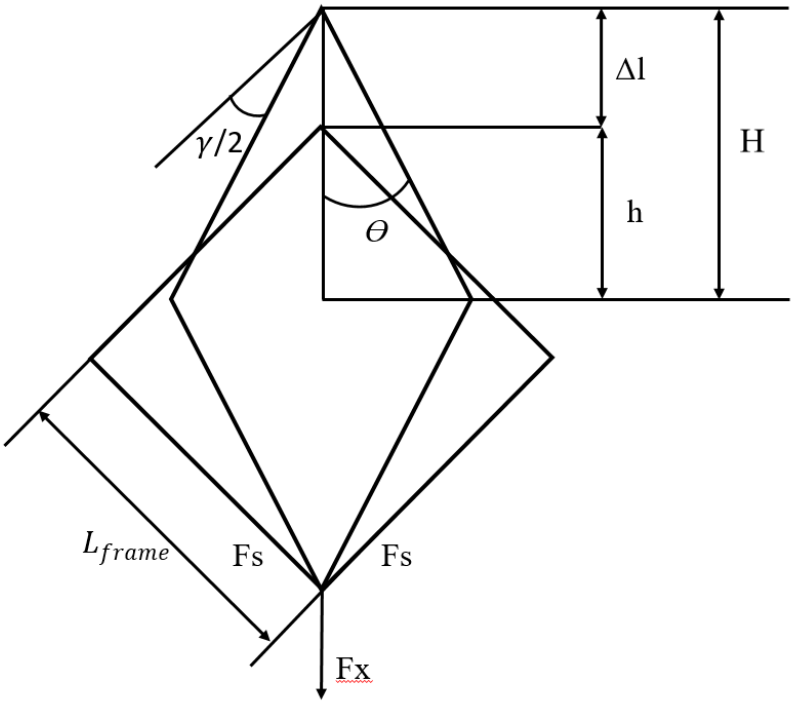

Figure 5.1 Schematic diagram of shear angle [53]

As the initial angle between neighbouring pivoted links of the apparatus is 90˚, the shear angle can be calculated using Equation 5.1:

$$\gamma = 90^{\circ} - 2\theta \tag{5.1}$$

where θ is the half angle between neighbouring pivoted links of the apparatus after deformation, as shown in Figure 5.1. This angle can be calculated using Equation 5.2:

$$\cos(\theta) = \frac{\sqrt{2}L_{frame} + \Delta l}{2L_{frame}} \tag{5.2}$$

where L_{frame} is the length of a pivoted link which is 70mm, and Δl is the distance between the initial and final positions of a corner, before and after deformation as shown in Figure 5.1. The relationship between shear force *Fs* and load *F* is given by Equation 5.3:

$$Fs = \frac{F}{2\cos(\theta)} \tag{5.3}$$

When analysing the shear behaviour of a sample, the values of shear force are influenced not only by the mechanical properties of the sample itself, but also by the size of the rig and dimensions of the sample. To eliminate the influence of dimensions, shear forces must be converted into normalized shear forces. Thus, the normalized force *Fn* is calculated using Equation 5.4:

$$Fn = \frac{Fs}{L_{frame} \times W_{fabric}} \tag{5.4}$$

where W_{fabric} is the width of the coupon. Equation 5.4 is not the same as used in other works related to the calculation of normalized shear forces for the testing of typical cruciform in-

plane shear samples. For example, the master's thesis of Thanos Drivas states that the normalized shear force is calculated using Equation 5.5:

$$Fn = Fs\frac{L_{frame}}{L_{fabric}^2} \tag{5.5}$$

where L_{fabric} is the width of the square central section of fabric in this case. In experiments reported by Drivas, the central section of the sample is square, hence its length and width are the same. As such, with an increase in L_{frame}, both the length and width of the central section of the sample. For example, if the length of the pivoted links is doubled, the length of both adjacent sides double, and the area of the sample multiplies by four. However, in the present case, the length of the coupon is the same as the length of the link and changes with it, while the width of the coupon stays constant. Thus, the area of the sample only doubles with a doubling of link length.

5.2.1 Analysis of results

Curves of the normalized shear force as a function of shear angle for ligament series 10x are shown in Figures 5.2.1 to 5.2.5. By observing the curves, it can be seen that as the cycle number increases, the curves have a tendency to shift to the right, which means that under the same shear force, the shear angle tends to be higher upon successive cycles. As the cycles are imposed, yarns gradually reorganize within the coupons. Besides, except for the trial curves, all curves show stress relaxation after holding shear angle constant for a period of time.

According to research [54], textile show stress relaxation under compaction due to fibre reorganization, which is the same mechanism of stress relaxation under shear stress.

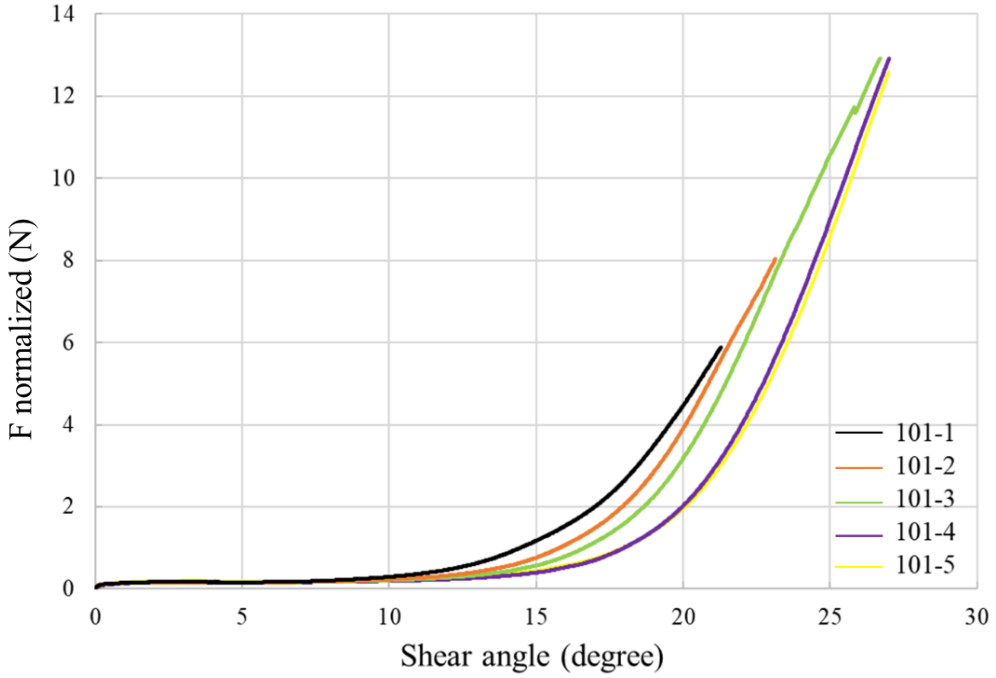

Figure 5.2.1 Shear test results for coupon 101

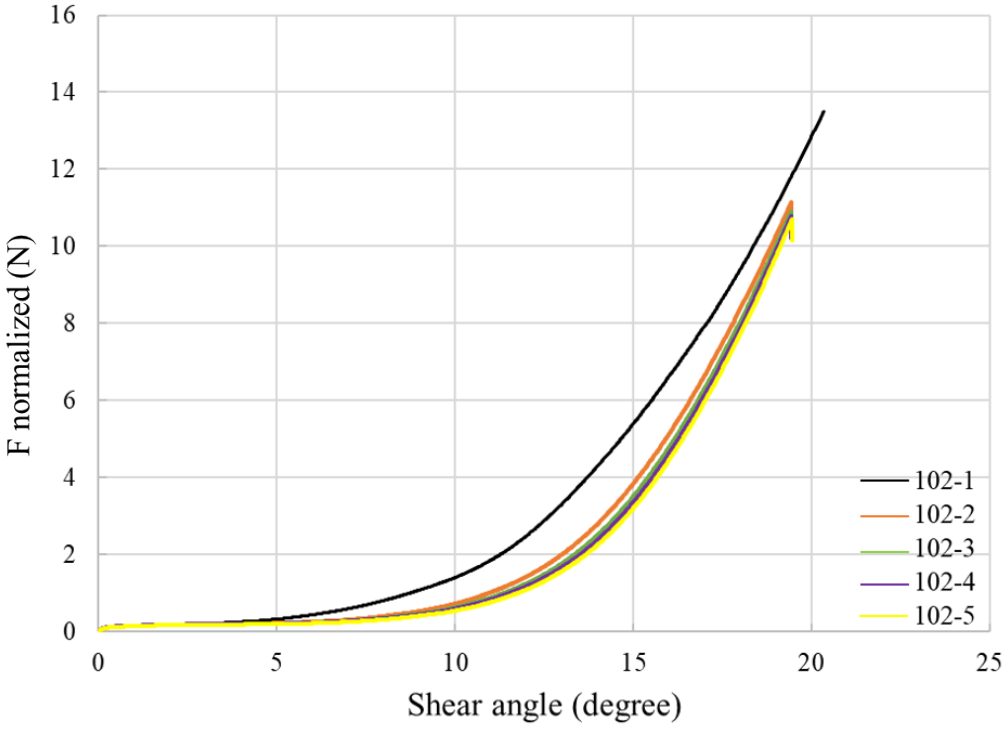

Figure 5.2.2 Shear test results for coupon 102

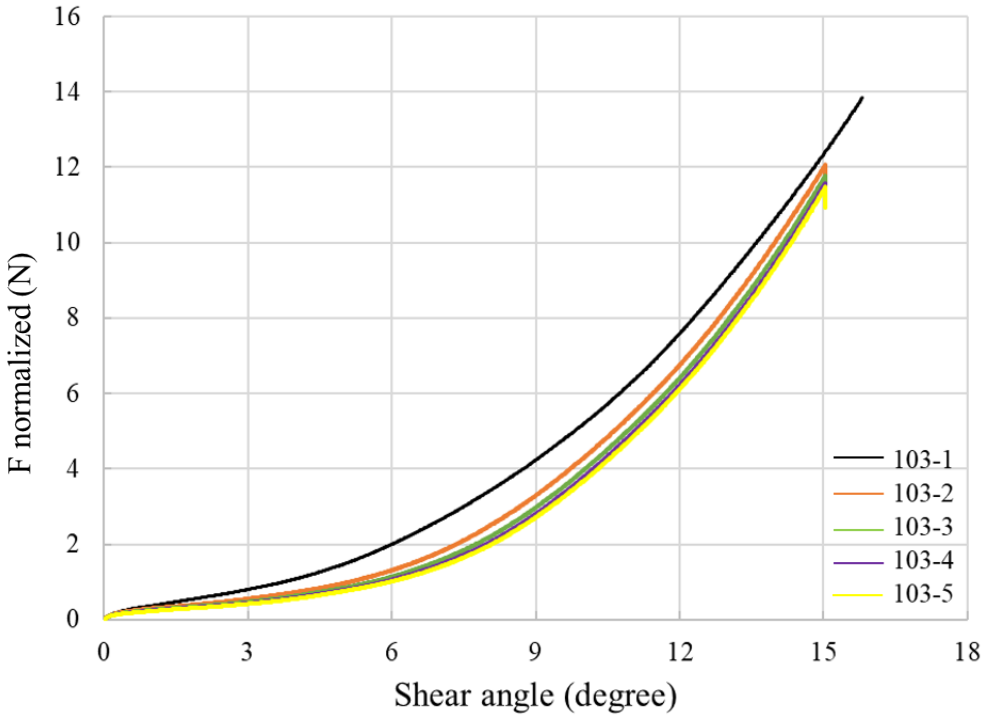

Figure 5.2.3 Shear test results for coupon 103

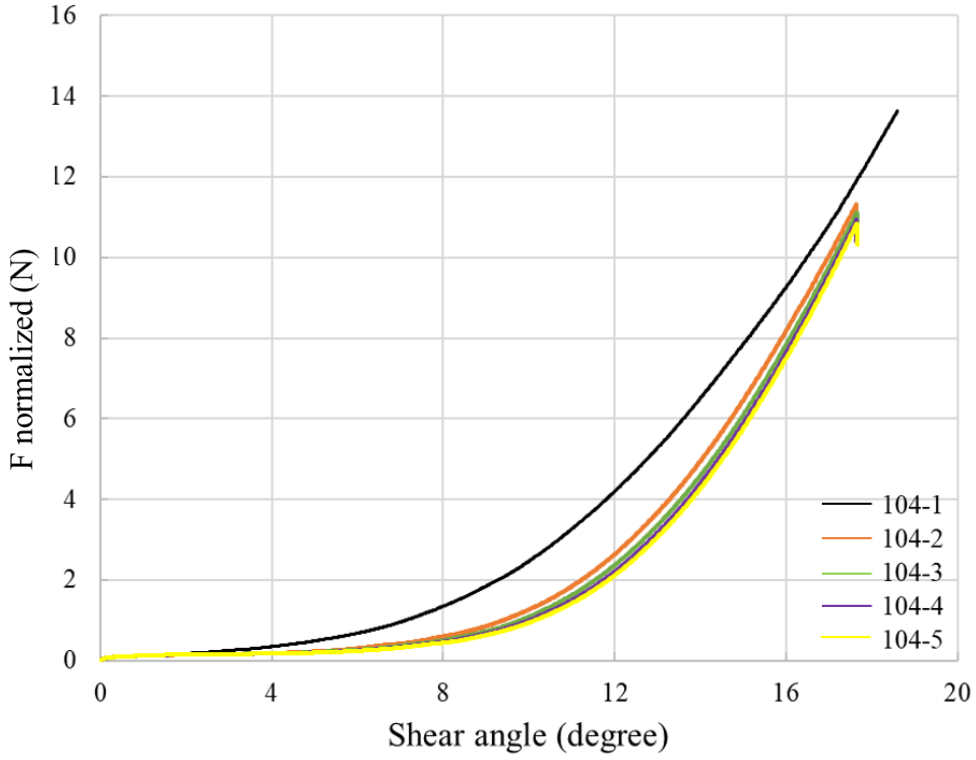

Figure 5.2.4 Shear test results for coupon 104

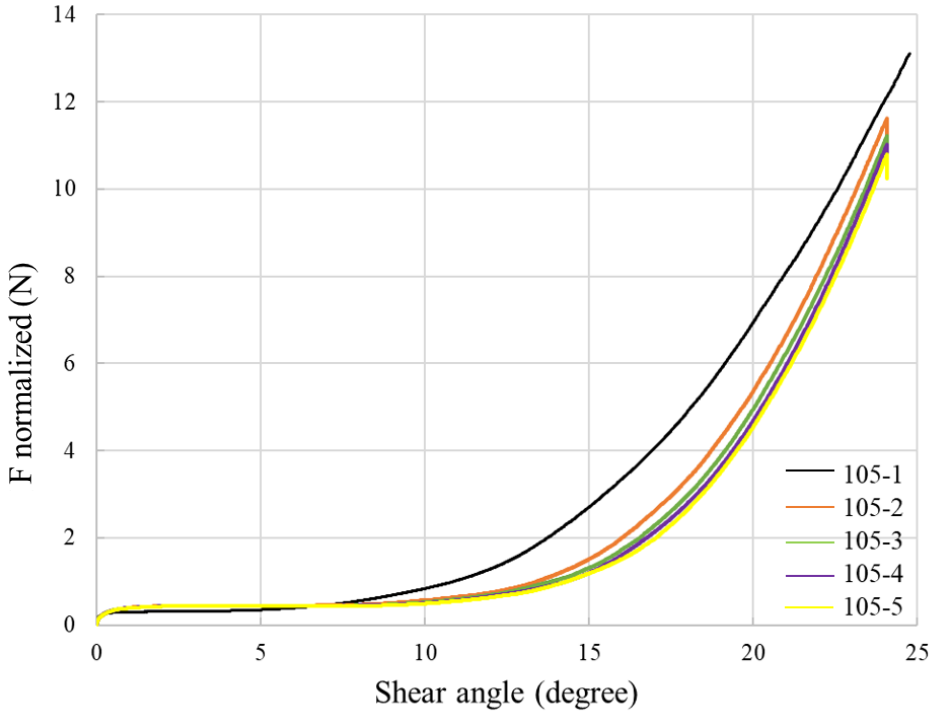

Figure 5.2.5 Shear test results for coupon 105

As most of the curves end at a normalized shear force slightly higher than 10 N, three points were chosen for analysing the shear stiffness for each curve, at 1 N, 5 N and 10 N. The slope of the tangent to the curve at each point is the corresponding shear stiffness. To minimize error, ten points on each curve closest to the chosen force levels were picked in order to calculate the stiffness. Table 5.1 shows shear stiffness at the chosen three force levels for coupon series 10x.

Table 5.1 Shear stiffness for coupon series 10x

Shear stiffness for coupon 101 (N / degree)							
Load	101-1	101-2	101-3	101-4	101-5	Average	Standard deviation
1 N	0.3056	0.3427	0.3520	0.3634	0.3329	0.3393	0.0220
5 N	1.1079	1.3393	1.4608	1.4803	1.4528	1.3682	0.1556
10 N			1.5488	2.0150	2.0370	1.8669	0.2757
Shear stiffness for coupon 102 (N / degree)							
Load	102-1	102-2	102-3	102-4	102-5	Average	Standard deviation
1 N	0.2747	0.3461	0.3444	0.3440	0.3477	0.3314	0.0317
5 N	1.1141	1.3678	1.4549	1.4537	1.4818	1.3745	0.1517
10 N	1.6387	1.9600	2.0249	2.0795	2.1350	1.9676	0.1950
Shear stiffness for coupon 103 (N / degree)							
Load	103-1	103-2	103-3	103-4	103-5	Average	Standard deviation
1 N	0.3047	0.2874	0.3176	0.3125	0.3178	0.3080	0.0127
5 N	0.9854	1.1695	1.1812	1.2123	1.2102	1.1517	0.0948
10 N	1.5884	1.8371	1.9270	1.9733	1.9413	1.8534	0.1565
Shear stiffness for coupon 104 (N / degree)							
Load	104-1	104-2	104-3	104-4	104-5	Average	Standard deviation
1 N	0.3578	0.4005	0.4183	0.4242	0.4312	0.4064	0.0294
5 N	1.1309	1.3952	1.4297	1.4798	1.5023	1.3876	0.1495
10 N	1.5602	1.9335	2.0496	2.0896	2.1179	1.9502	0.2290
Shear stiffness for coupon 105 (N / degree)							
Load	105-1	105-2	105-3	105-4	105-5	Average	Standard deviation
1 N	0.2205	0.2781	0.2212	0.2462	0.2576	0.2447	0.0246
5 N	0.8853	1.1193	1.1804	1.2231	1.2531	1.1323	0.1469
10 N	1.3664	1.7706	1.8032	1.7969	1.8693	1.7213	0.2017

A number of observations can be made from Table 5.1. Firstly, the shear stiffness increases as the shear force increases, and it reaches a maximum around 1.8 N / degree at maximum test

shear force. This increase happens because at low force levels, yarns are distanced from each at the start of the start of a test. As the test proceeds, yarns get closer and they begin to compress each other laterally, increasing resistance to further in-plane shear. When comparing maximum stiffness observed for five consecutive cycles on the same coupon, the standard deviation is relatively low at within 0.3 N / degree, compared with the average stiffness around 1.8 N / degree. Besides, as the number of cycles increases, the shear stiffness at the three chosen force levels rises moderately. This is also the result of the gradual lateral compression of the yarns. When comparing the behaviour of five coupons, the average stiffness values at the three chosen loads are not exactly equal but they are similar. This can be explained by difference in the way each coupon is mounted.

The shear test results for series 20x are shown in Figures 5.2.6 to 5.2.10.

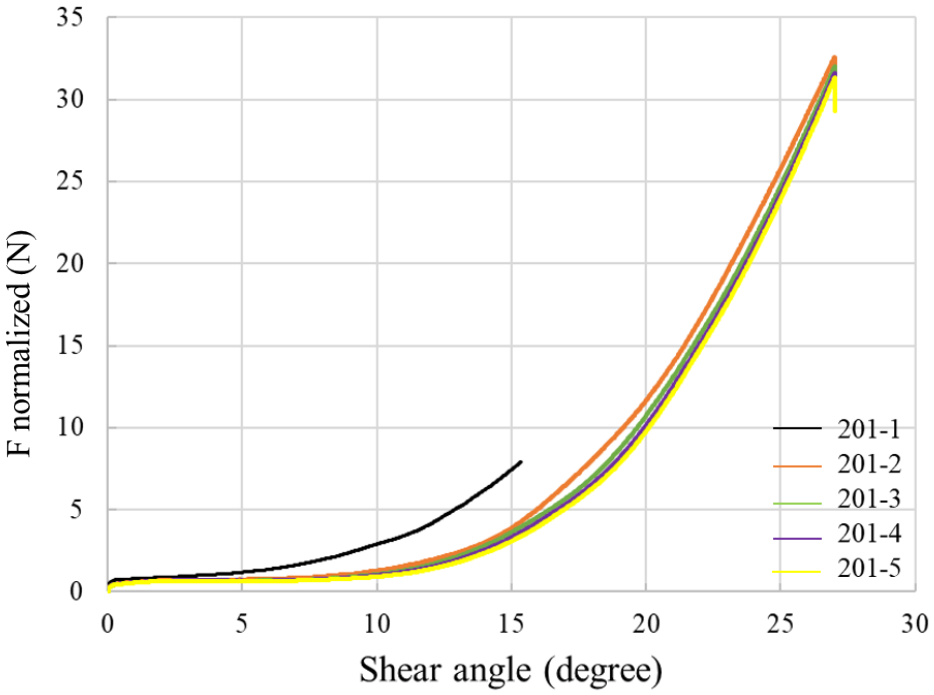

Figure 5.2.6 Shear test results for coupon 201

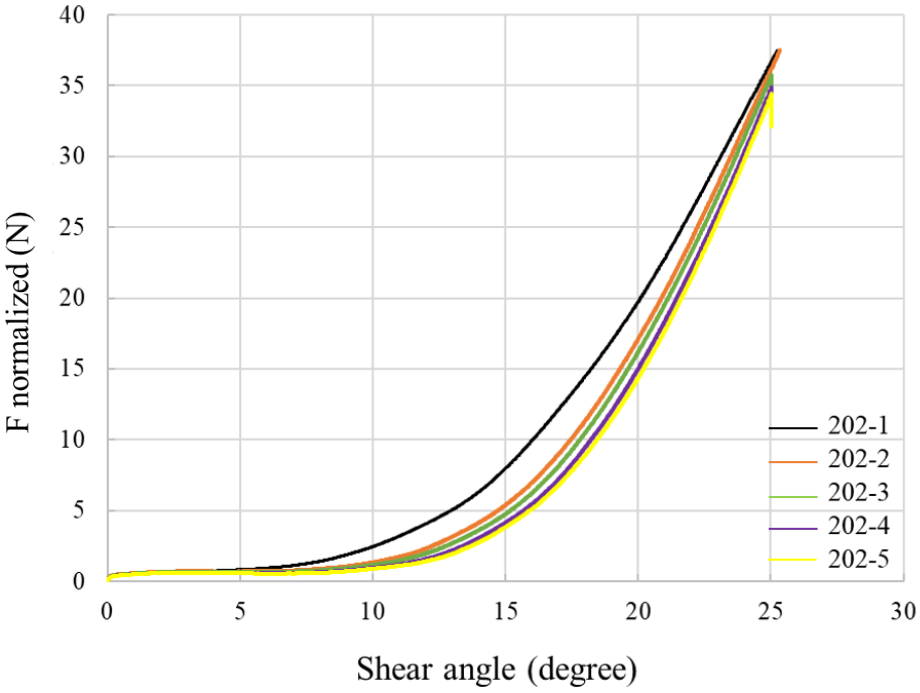

Figure 5.2.7 Shear test results for coupon 202

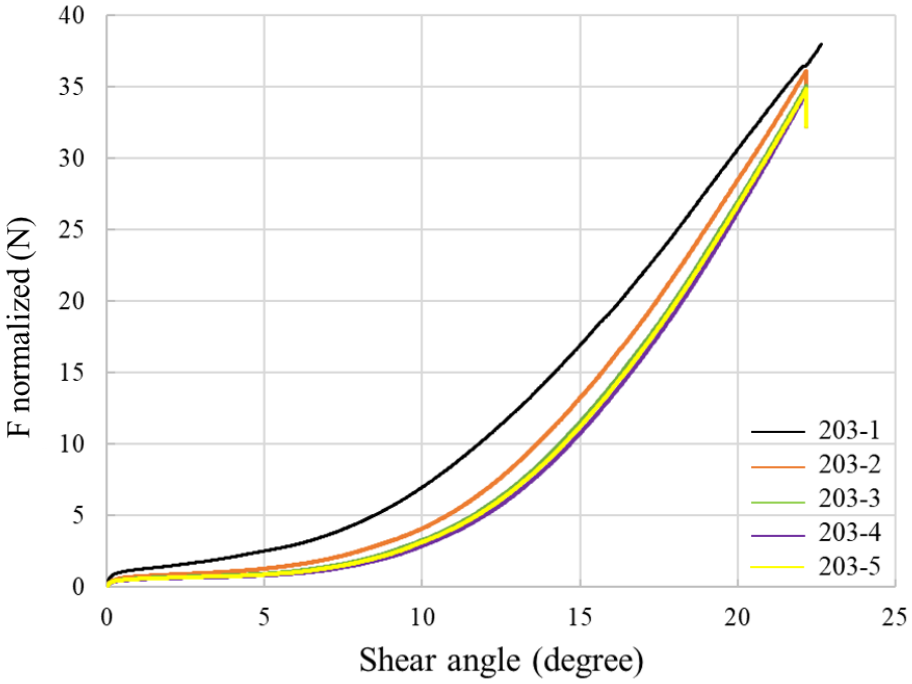

Figure 5.2.8 Shear test results for coupon 203

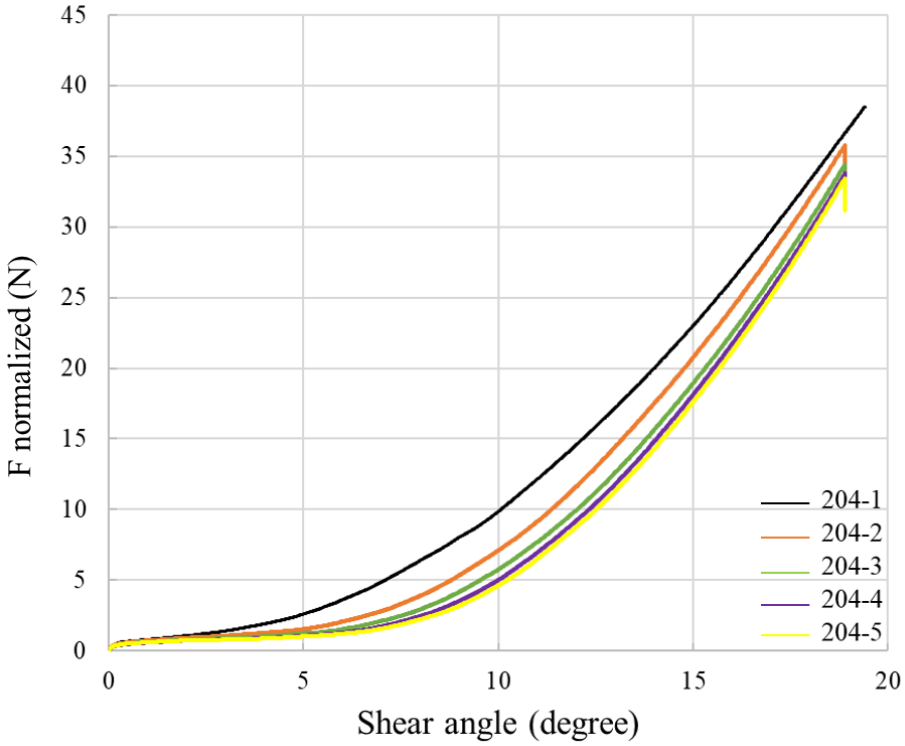

Figure 5.2.9 Shear test results for coupon 204

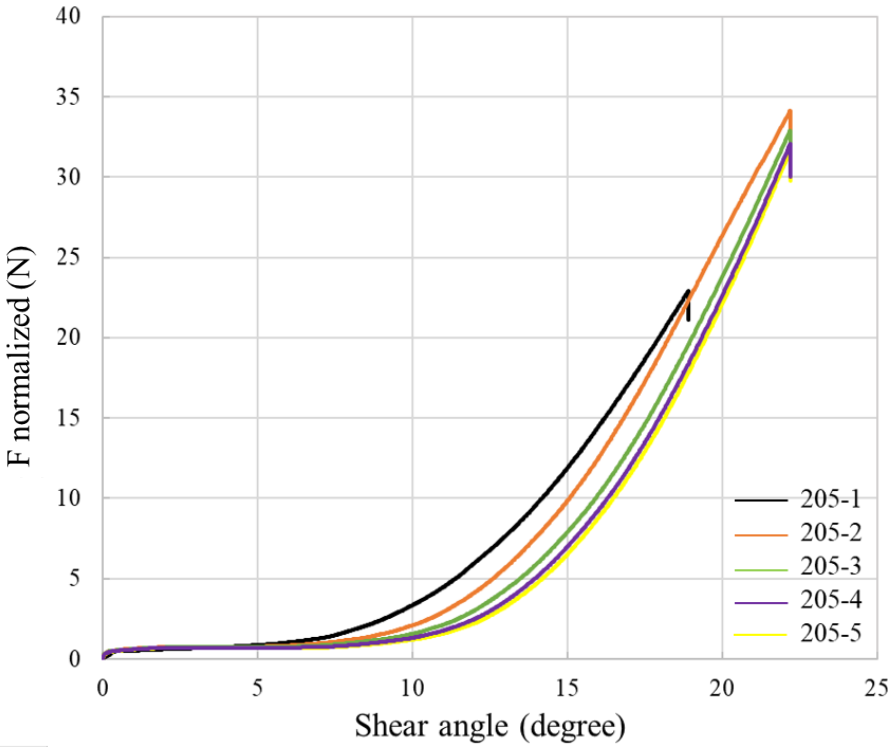

Figure 5.2.10 Shear test results for coupon 205

Similarly to 10x, the curves generated for series 20x also show a trend of moving to the right as the cycle number increases. The same procedure was used for analysing shear stiffness for series 20x coupons. In this case, as most curves ended at force levels over 30 N, the three force levels chosen for analysing shear stiffness were 3 N, 15 N and 30 N. Shear stiffness of series 20x is shown in Table 5.2.

Table 5.2 Shear stiffness for coupon series 20x

Shear stiffness for coupon 201 (N / degree)							
Load	201-1	201-2	201-3	201-4	201-5	Average	Standard deviation
3 N	0.4122	0.7095	0.7580	0.7743	0.7778	0.6863	0.1392
15 N		2.6330	2.5634	2.6664	2.7152	2.6445	0.0552
30 N		3.2580	3.6825	3.8236	3.7462	3.6276	0.2192
Shear stiffness for coupon 202 (N / degree)							
Load	202-1	202-2	202-3	202-4	202-5	Average	Standard deviation
3 N	3.5662	0.8343	0.9021	0.9477	0.9415	1.4384	1.0647
15 N	2.4571	3.0922	3.0265	3.1110	3.2214	2.9816	0.2697
30 N	3.5662	3.9789	4.2713	4.4266	4.4938	4.1474	0.3404
Shear stiffness for coupon 203 (N / degree)							
Load	203-1	203-2	203-3	203-4	203-5	Average	Standard deviation
3 N	0.5784	0.7220	0.8004	0.8901	0.8979	0.7778	0.1187
15 N	2.2503	2.6590	2.8960	2.8381	2.7413	2.6769	0.2282
30 N	2.9511	3.3864	3.6453	3.8825	3.5652	3.4861	0.3114
Shear stiffness for coupon 204 (N / degree)							
Load	204-1	204-2	204-3	204-4	204-5	Average	Standard deviation
3 N	0.9846	0.9941	1.1620	1.1124	1.1222	1.0750	0.0720
15 N	2.5361	3.0084	3.1730	3.2363	3.2595	3.0427	0.2680
30 N	3.5890	3.9862	4.2697	4.4221	4.4987	4.1531	0.3321
Shear stiffness for coupon 205 (N / degree)							
Load	205-1	205-2	205-3	205-4	205-5	Average	Standard deviation
3 N	0.9350	1.0648	1.0987	1.1560	1.1628	1.0835	0.0827
15 N	2.6936	3.1978	3.3043	3.3429	3.4434	3.1964	0.2634
30 N		3.6477	4.2304	4.4168	4.5127	4.2019	0.3357

The average maximum shear stiffness for all 20x coupons are around 4 N / degree, much higher than series 10x. As samples 20x are narrower than samples 10x, under the same maximum load, the maximum normalized shear force applied on 20x reached 30 N while it was limited to 10 N on 10x. Because shear stiffness increases with shear force, this difference is not unexpected. Except for that, other features of results for sample series 20x are similar to those for sample series 10x. Differences and standard deviations between coupons were seen to be contained.

Figure 5.2.11 to 5.2.15 show the shear test results of series 30x.

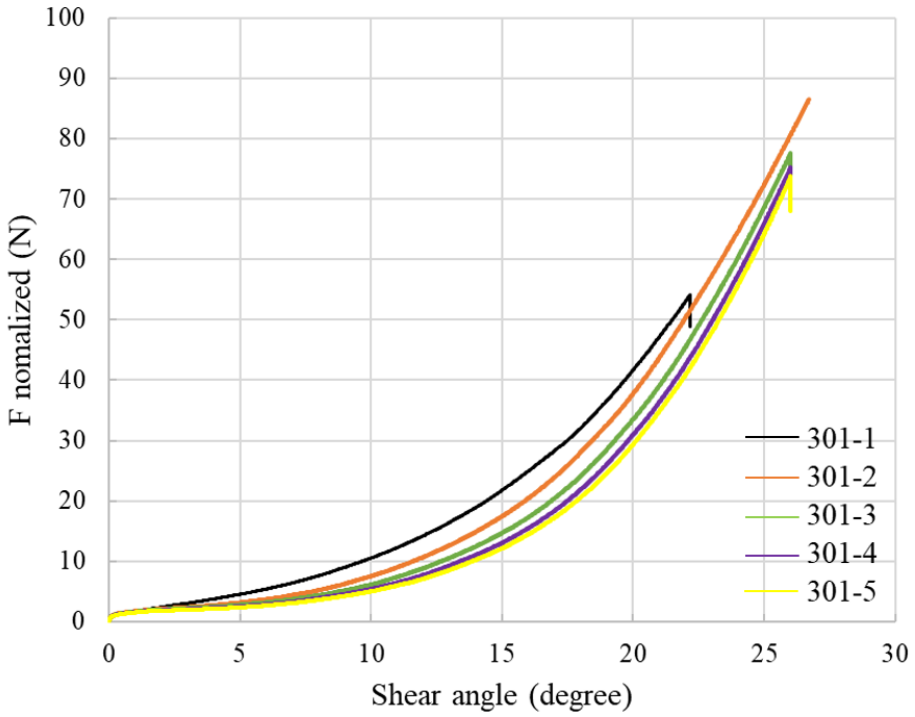

Figure 5.2.11 Shear test results for coupon 301

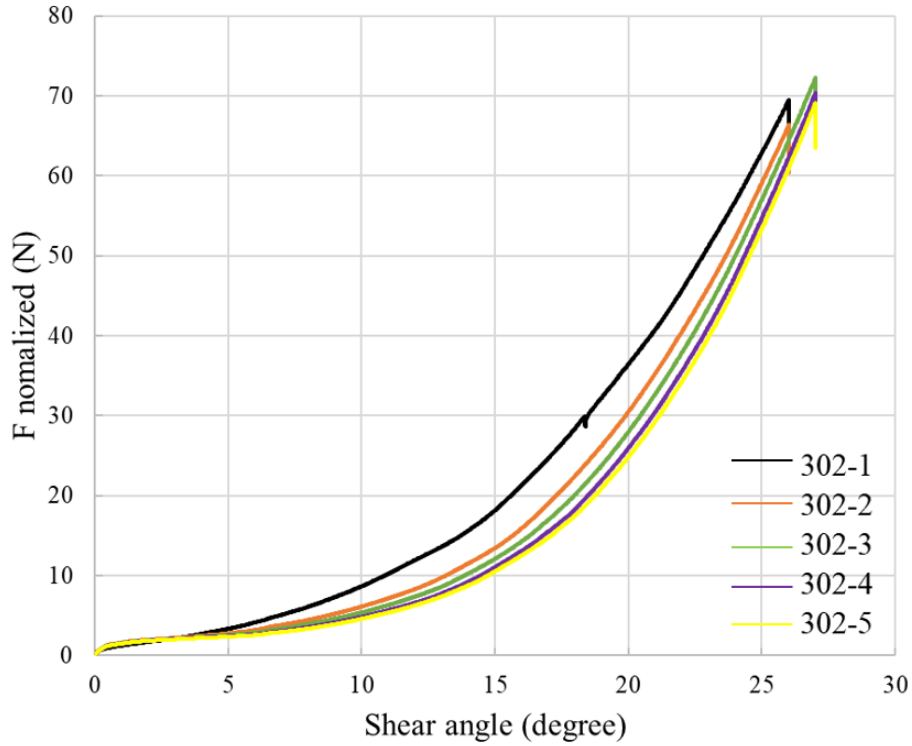

Figure 5.2.12 Shear test results for coupon 302

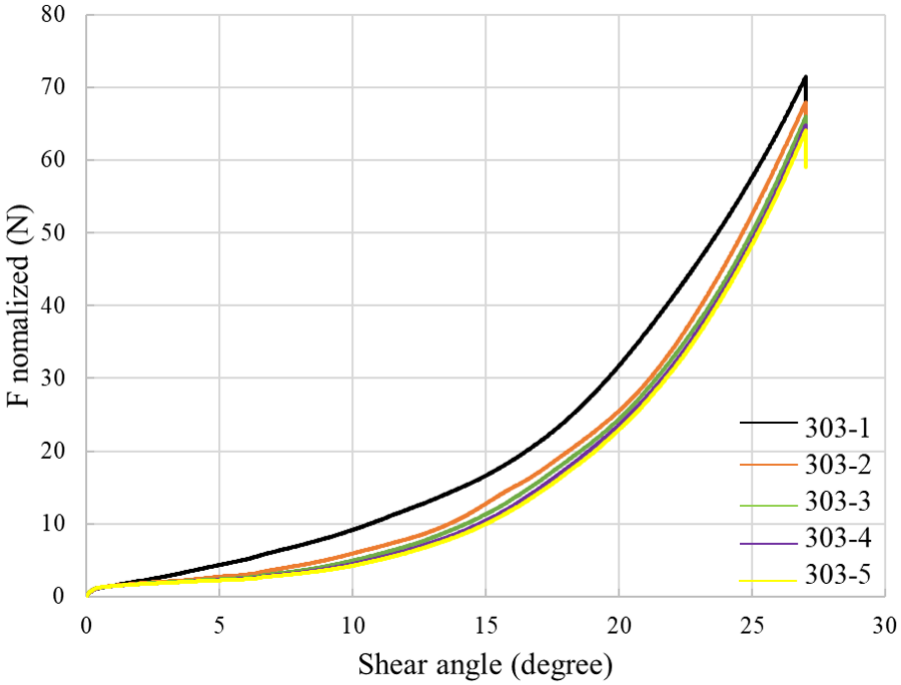

Figure 5.2.13 Shear test results for coupon 303

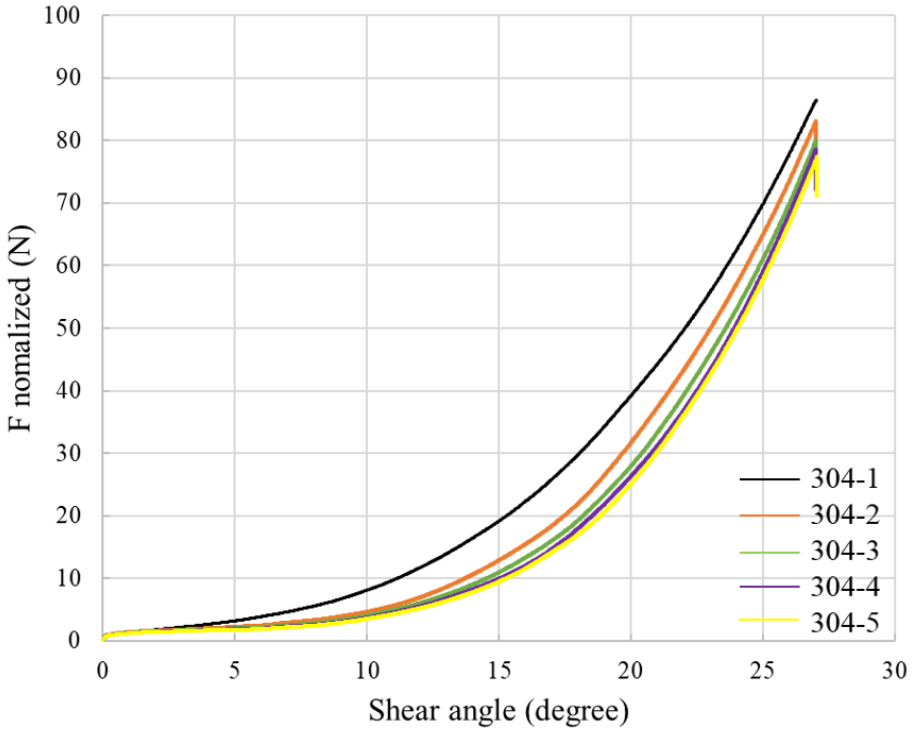

Figure 5.2.14 Shear test results for coupon 304

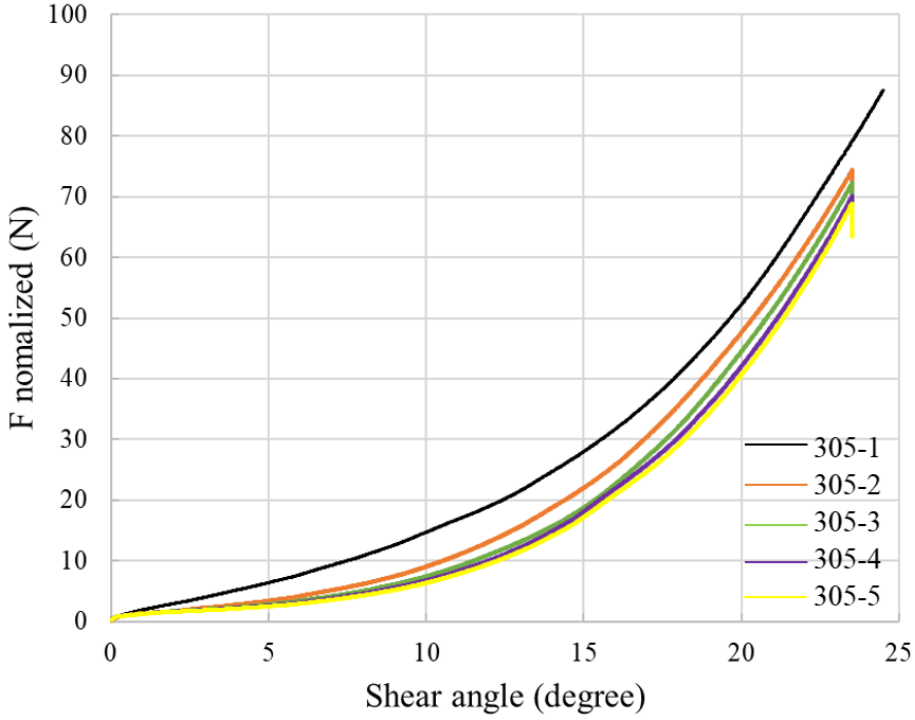

Figure 5.2.15 Shear test results for coupon 305

The shear curves for coupons of series 30x showed the same trends as observed for series 10x and 20x. Maximum shear force was under 60 N so three points at 6 N, 30 N and 60 N were chosen for calculating shear stiffness. The shear test results are shown in Table 5.3.

Table 5.3 Shear stiffness for coupon series 30x

Shear stiffness for coupon 301 (N / degree)							
Load	301-1	301-2	301-3	301-4	301-5	Average	Standard deviation
6 N	0.9331	1.0223	0.9623	1.1273	1.1333	1.0357	0.0825
30 N	3.9903	4.5713	4.8899	5.2427	5.3218	4.8032	0.4867
60 N		7.1398	7.7626	8.1197	8.6267	7.9122	0.5414
Shear stiffness for coupon 302 (N / degree)							
Load	302-1	302-2	302-3	302-4	302-5	Average	Standard deviation
6 N	1.1705	0.9552	0.9666	0.9034	0.9479	0.9887	0.0934
30 N	7.6762	4.4496	4.6575	4.7145	4.8207	5.2637	1.2123
60 N	6.2862	6.9605	7.3203	7.5803	7.6777	7.1650	0.5047
Shear stiffness for coupon 303 (N / degree)							
Load	303-1	303-2	303-3	303-4	303-5	Average	Standard deviation
6 N	0.9396	0.9491	0.9974	0.9929	1.2634	1.0285	0.1197
30 N	4.0034	4.4405	4.4747	4.5636	4.5643	4.4093	0.2087
60 N	6.3622	7.7821	8.2211	8.3170	8.2229	7.7811	0.7334
Shear stiffness for coupon 304 (N / degree)							
Load	304-1	304-2	304-3	304-4	304-5	Average	Standard deviation
6 N	1.0881	1.2272	1.1184	1.1802	1.2011	1.1630	0.0519
30 N	4.2442	5.3266	5.1934	4.9458	5.3904	5.0201	0.4168
60 N	6.8614	7.9542	8.2012	8.9690	8.7369	8.1445	0.7371
Shear stiffness for coupon 305 (N / degree)							
Load	305-1	305-2	305-3	305-4	305-5	Average	Standard deviation
6 N	1.2778	1.0949	1.1154	1.1910	1.2248	1.1808	0.0680
30 N	3.8324	4.9374	4.9996	5.0309	5.1339	4.7868	0.4814
60 N	7.6070	7.6762	8.1566	8.4559	8.6431	8.1078	0.4116

For series 30x, the maximum shear stiffness is around 8 N / degree, much higher than series 10x and 20x. That is because of two reasons. On one hand, series 30x is narrower than 10x and 20x, so the normalized shear force is higher, as the shear stiffness. On the other hand, as mentioned in Chapter 3, series 30x samples are densely weaved. The distance between adjacent yarns is smaller so the compaction of the yarns is higher, which increases the resistance to shear deformation. As a result, even when comparing shear stiffness between samples 30x and 20x under the same normalized shear force, 30 N for example, is observed that stiffness of sample series 30x is still higher than that of samples from series 20x.

5.3 Conclusion

A few conclusions can be drawn from the curves and tables above. Firstly, shear stiffness increases non-linearly with shear force and shear angle as a result of the compaction between adjacent yarns increasing gradually. Secondly, all the curves show a trend to shift to the right and show stress relaxation after holding for a period of time under maximum extension. The two phenomena result from the same physical cause, which is that yarns gradually reorganize within coupons. Thirdly, the maximum shear stiffness of sample series 30x is the highest, indicating that the density of textiles influences the shear stiffness to a great extent.

Chapter 6 – Finite element analysis

Models of the artificial textile ligaments discussed in previous chapters of the thesis were constructed using textile modelling software TexGen, then transferred to finite element solver ANSYS. Tensile loads were applied, and resulting stiffness values were investigated along with the effect of simulation parameters on the distributions of stresses and strains. The aims of this work were to conduct an initial attempt at modelling, to study the effect on various parameters such as the contact conditions at yarn crossovers, and to compare values of the tensile stiffness obtained from experiments and simulations. In this chapter, the method used for constructing models and conducting structural analyses are introduced. Then, a number of cases of increasing complexity are presented, culminating in models that include the interlacing patterns and major features of the physical artificial knee ligaments.

6.1 Textile modelling software: TexGen

TexGen [55] is a software enabling the creation of 3D models of textiles. In TexGen, yarns are modelled as continuous solids. The paths of individual yarns are identified through the positioning of multiple nodes connected to each other. A yarn is created by defining the coordinates of these nodes, as well as the shape and dimension of the yarn cross-section at each node. By creating multiple yarns and adjusting the coordinates of the nodes, and ensuring that each yarn contacts superimposed yarns without passing through, 3D models featuring interlacing patterns similar to those of real textiles can be constructed.

Figure 6.1 shows a 3D model of a repeating unit cell for artificial knee ligament series 10x. In order to adjust the contact region accurately, the paths of each warp yarn and of each weft yarns were defined using 20 nodes and 11 nodes, respectively. The presence of an overlap or of an interference at each yarn crossover can be assessed using TexGen functionality 'Render textile interference'. As showed in Figure 6.2, the white dots highlighted within the two white ellipses indicate interference, which must be avoided by manually relocating nearby nodes. Once a model is complete and interference-free, it is exported as an IGES file and imported into ANSYS for quasi-static structural analysis.

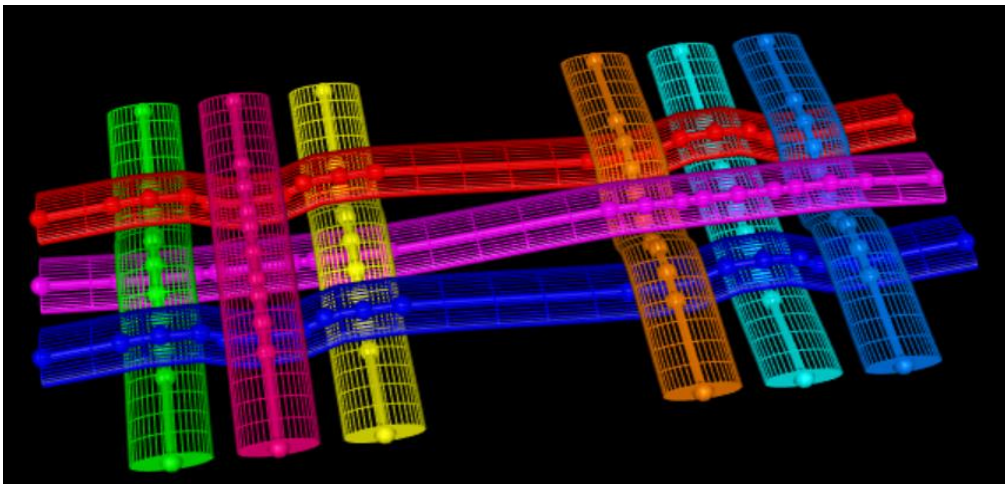

Figure 6.1 3D TexGen model of artificial knee ligament series 10x

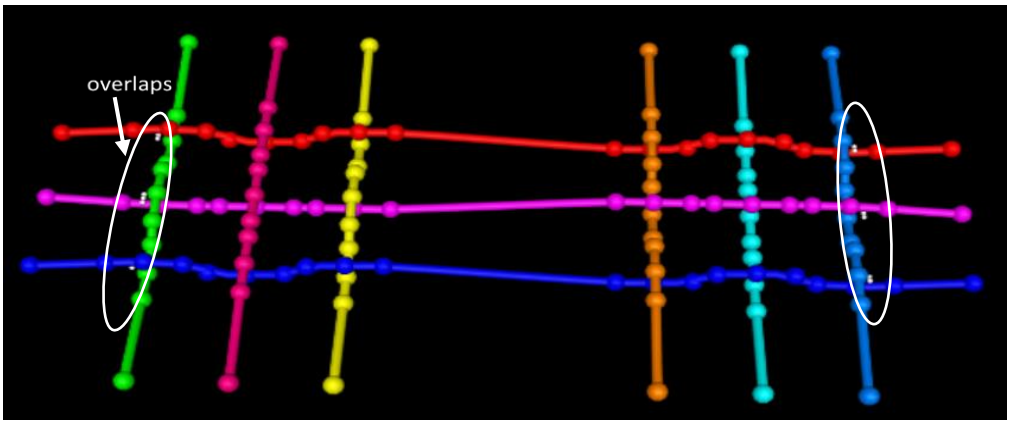

Figure 6.2 Interference in textile model, prior to manual displacement of nearby nodes

6.2 Quasi-static structural analysis: ANSYS

ANSYS [56] is a software enabling the iterative computation of solutions to a number of mathematical problems defined over domains of complex geometry, including quasi-static structural analyses, based on the finite element method. In this work, ANSYS was used for analysing stresses, strains and elongations in the TexGen textile models, resulting from the application of tensile forces as specified below. The basic concept of the finite element method is to divide a domain of complex geometry into numerous adjoining and connected domains of simple geometry, and to solve the equilibrium, continuity, compatibility and constitutive equations defined over every smaller domains – or elements – iteratively. Given the material properties, boundary conditions and applied forces, ANSYS can replicate an actual loading case through a model that is more or less simplified or faithful to the physical case, and provide results that are useful in probing and understanding the behaviour of physical structures. In the following sections, work conducted towards identifying and implementing suitable material properties, model parameters and static conditions is presented.

6.2.1 Case 1

A few simple models were created and tested initially, in order to establish simulation parameters as well as validate settings and accuracy. More extensive models that replicate the

geometry of the artificial knee ligaments probed in the previous chapters were developed afterwards.

Case 1 and its sub-cases 1a, 1b, 1c, 1d, 1e and 1f featured two perpendicular straight yarns overlapping and touching each other at their centers. One yarn extended along axis *x* while the other extended along axis *y*. The geometric model for Case 1 is shown in Figure 6.2.1. Each yarn was 10 millimeters long. Both yarn cross-sections were ellipses with a major radius r_1 = 0.3 mm and a minor radius r_2 = 0.06 mm, the value of r_1 was selected from yarn width in series 10x shown in Table 3.2. The cross-section areas of warp yarns was calculated in Chapter 4. As 10x samples feature around 30 warp yarns, the minor radius of a yarn was approximated as follows, acknowledging that actual yarn sections are never perfectly elliptic and typically flatten in the thickness at contact points:

$$r_2 = \frac{A'}{\pi r_1} = \frac{\frac{1}{30}A}{\pi \times 0.3mm} \tag{6.2}$$

where A is the cross-section area of all warp yarns in a sample and A' is the cross-section area of one single yarn. As yarns consist of numerous individual fibres as opposed to being continuous solids as modelled in TexGen and ANSYS, the constitutive behaviour of the yarns along and across their main direction was replicated using a linear orthotropic material. As discussed in Chapter 3, Young's modulus of oriented PET fibres ranges around 10 GPa. Considering that a single yarn is not completely filled with fibres and assuming that the yarn

fibre volume fraction is around 70%[57], an orthotropic material with Young's moduli of 7×10^9 Pa along yarn and 7×10^6 Pa across the yarn was applied to the model. The ratio of the transverse modulus to the longitudinal modulus was set to 0.001, which is the lowest value that would reliably lead to convergence in ANSYS.

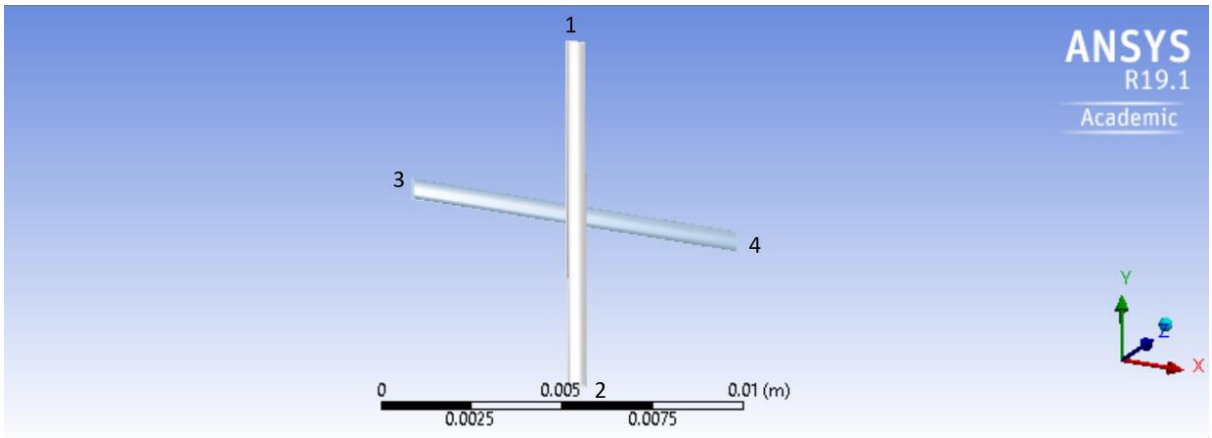

Figure 6.2.1 Geometric model, Case 1

In Figure 6.2.1, the four yarn ends are numbered from 1 to 4. For Case 1a, ends 1, 2 and 3 were fixed. Initially, a force of 0.01 N was applied to the vertical surface at end 4, along axis *x*; the surface is normal to yarn 3-4 and the force is parallel to the yarn. This initially applied force was low but sufficient to induce deformation; it was increased in following attempts to observe changes in deformation under increasing applied force. In Case 1a the contact type between the two yarns was set as frictionless. Elongation along axis *x* is shown in Figure 6.2.2.

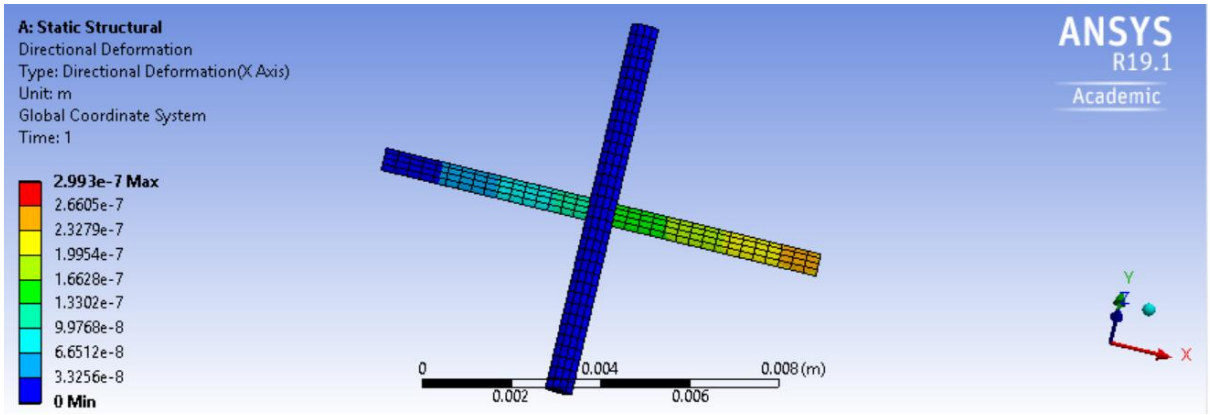

Figure 6.2.2 Elongation along axis *x*, Case 1a

At end 4, maximum elongation was 2.993×10^{-7} m. The corresponding theoretical value for this elongation can be calculated using Equation 6.3:

$$\delta = \frac{FL}{SE} = \frac{0.01 \times 0.01}{5.65 \times 10^{-8} \times 7 \times 10^{9}} = 2.53 \times 10^{-7} \tag{6.3}$$

where δ is the maximum elongation along axis *x* at end 4, *F* is the applied external force, *L* is the length of yarn 3-4, *S* is cross-section area of the yarn, and *E* is Young's modulus of yarn 3-4 along its axis. The error between theoretical and simulation values is:

$$\frac{2.993 \times 10^{-7} - 2.53 \times 10^{-7}}{2.993 \times 10^{-7}} \times 100\% = 15.4\% \tag{6.4}$$

It was initially conjectured that the error may originate from end effects. As seen in Figure 6.2.3, the surface load does not result in uniform deformation over that surface. In order to investigate whether this effect resulted from usage of orthotropic material properties, an isotropic material with Young's modulus equal to 7×10^{9} Pa along axes *x*, *y* and *z* was assigned to the same model. The results shows a similar discrepancy and the same end effect. Therefore, the material properties did not cause the discrepancy.

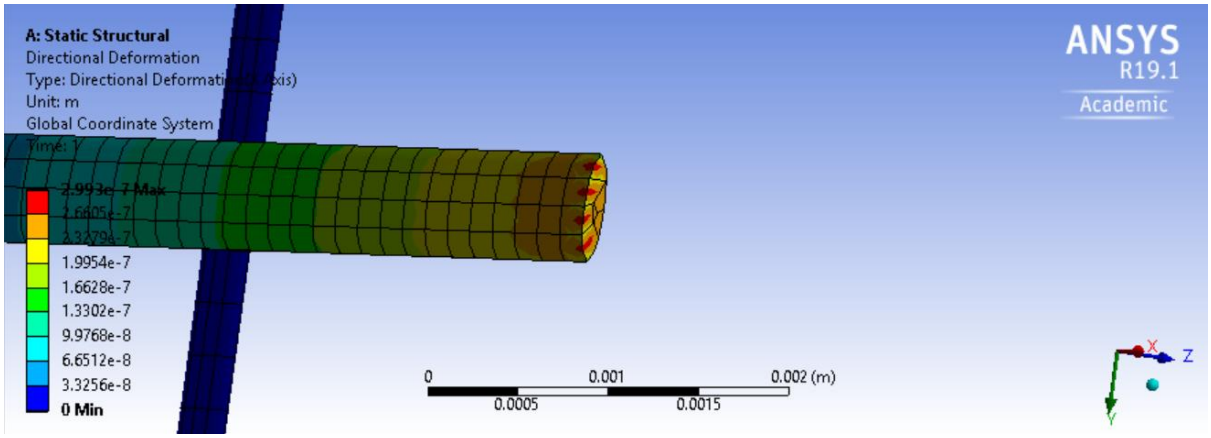

Figure 6.2.3 Apparent uneven stress distribution and end effect at yarn end 4, Case 1a

The external load was then set to 0.1N and 1N respectively, using the original model, in order to observe the trend in elongation. The results were elongations of 2.993×10^{-6} m and 2.993×10^{-5} m respectively, showing a linear force-elongation behaviour. The stiffness of the yarn stayed constant as expected in Case 1a.

The contact type was then set as frictional in Case 1b with a coefficient of friction of 0.3, using the orthotropic material and an applied load of 0.01 N. Elongation stayed the same as recorded for the frictionless case, as the contact region was too small to influence the deformation and no vertical, normal loads were present at the contact.

The contact type was then set as bonded in Case 1c, which means that the two yarns were attached at their point of contact. The same orthotropic material was assigned to the model, and the same 0.01 N force was applied along axis *x*. This time, elongation at yarn end 4 was marginally smaller at 2.985×10^{-7} m. This is reasonable as the deformation of end 4 along axis

x is restricted by the lateral bending of yarn 1-2 along its local, transverse axis *y* – which is the same as global axis *x* for the complete model as seen in the Figure.

For Case 1d, the same isotropic material properties momentarily used in Case 1a were also tested in the bonded configuration. This led to an even smaller elongation of yarn 3-4 along axis *x*, recorded at 2.9613×10^{-7} m. This result is also reasonable as lateral bending of yarn 1-2 was expected to be more limited, since both yarns were made of an isotropic material with a higher transverse modulus and a higher stiffness in lateral bending.

Once the above simulations were completed it was envisaged that the 15.4 % error recorded for Case 1a may have resulted from the relatively coarse mesh used, which would have been entirely appropriate in terms of numerical convergence but possibly less so in terms of replicating the shape and elliptic envelope of the yarns, resulting in a smaller cross-section area compared to the original model hence leading to increased elongation. In order to further analyze the error, a finer mesh was generated from the same geometric model- and the same material properties were applied. The same static structural load case was used in one further static loading simulation labeled Case 1e. In Case 1e, element size was manually set to 0.00005 m, much smaller than the default size used in previous cases. Elongation along axis *x* is shown in Figure 6.2.4.

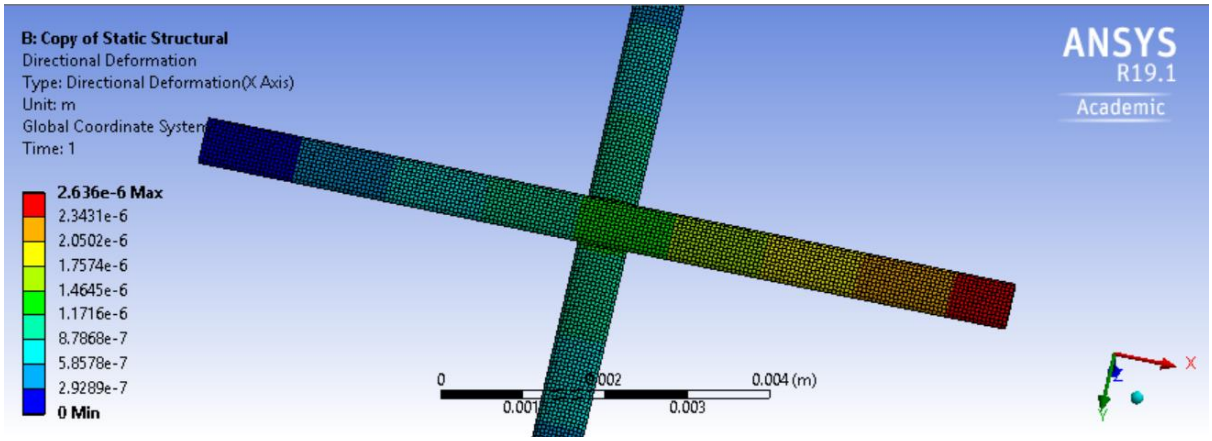

Figure 6.2.4 Elongation along axis *x*, Case 1e

The maximum elongation for Case 1e was 2.636 $\times 10^{-7}$, much smaller than observed in Case 1a. In Case 1e, the error between theoretical and simulation values was:

$$\frac{2.636 \times 10^{-7} - 2.53 \times 10^{-7}}{2.636 \times 10^{-7}} \times 100\% = 4.02\% \qquad (6.5)$$

Thus, a finer mesh that better espouses the external envelope of the yarns reduces error dramatically. However, this has the consequence of increasing computational times significantly, especially for cases of sliding contact between numerous distinct bodies as featured in the simulations undertaken for this work.

Hexahedral elements were used for Cases 1a to 1e. In order to generate a more faithful yarn envelope without increasing the number of elements substantially, meshing with tetrahedral elements was attempted. For Case 1f, one yarn was re-meshed using tetrahedral elements as shown in Figure 6.2.5.

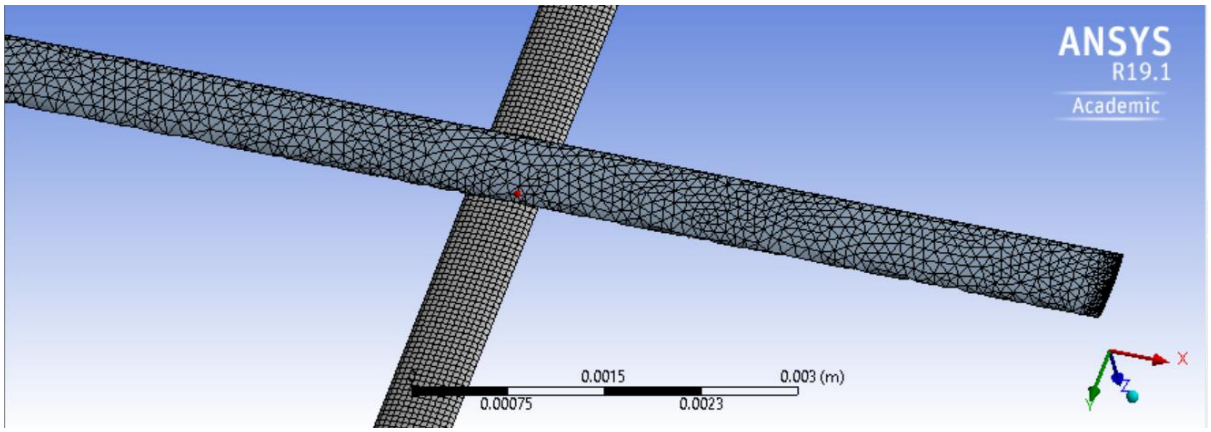

Figure 6.2.5 Model re-meshed using tetrahedral elements, Case 1f

For a number of elements similar to Case 1e, tetrahedral elements generally fill the yarn cross-better, but they leave many geometric irregularities on external surfaces as seen in Figure 6.2.5. Elongation along axis x is shown in Figure 6.2.6. The maximum elongation is 2.7961×10^{-7} m, smaller than for Case 1a but still larger than for Case 1e. Thus, tetrahedral elements were removed from consideration in further simulations.

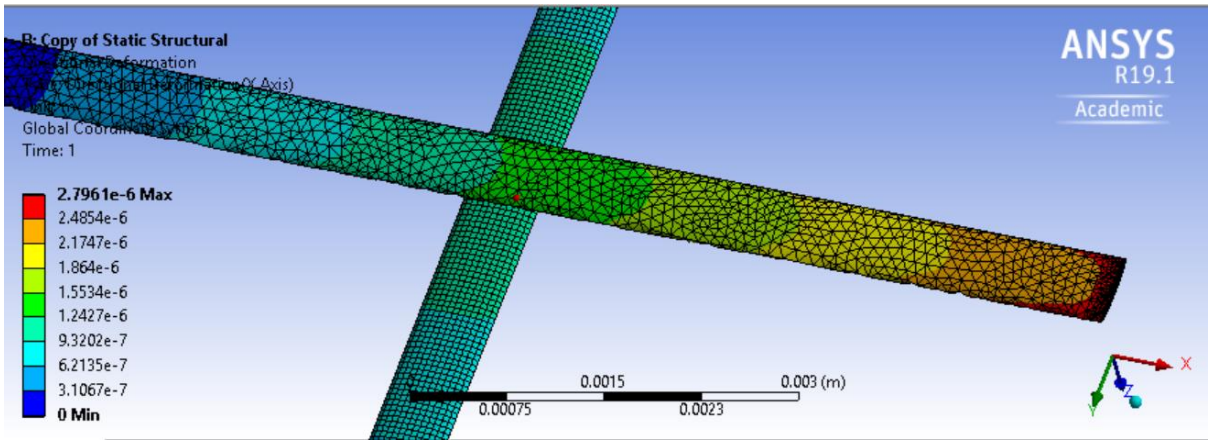

Figure 6.2.6 Elongation along axis *x*, Case 1f

In conclusion, a finer mesh using 0.00005 mm size hexahedral elements is most suitable for replicating the geometric envelop and mimic tensile behaviour of the yarns. However, using such elements make the management of contacts by ANSYS in such problems significantly

more demanding. For more complex models envisaged in this work, the proposition of the finer elements and meshes becomes untenable using the resources at hand. Considering that models in the following cases feature several woven yarns hence are markedly more complex than Case 1, the default mesh size was used in further work and the error caused by relatively coarse meshes and underrepresentation of the yarn cross-section area was eliminated through an increase in stiffness of 15.4 %.

Yarn stiffness in the models was calculated using the following equations:

$$\sigma = \frac{F}{A} \tag{6.6}$$

$$\varepsilon = \frac{\Delta L}{L} \tag{6.7}$$

$$E = \frac{\sigma}{\varepsilon} \tag{6.8}$$

where F represents the loads applied to the yarns; A is the yarn cross-section areas that sustain forces; ΔL is the maximum elongation that occurs in the models; L is the original projected length of the yarns, and E is tensile stiffness of the model.

6.2.2 Case 2

The model used in Case 2 and its sub-cases 2a, 2b and 2c is a single repeating unit cell of a plain woven textile, Figure 6.2.4. It consists of two warp yarns and two weft yarns, all of which are 9 mm in length. Each warp and weft yarn overlap each other at one-third of their length.

Yarn cross-sections are ellipses with the same radii used in Case 1. As discussed in Case 1, to eliminate error caused by the relatively coarse mesh, the material properties were modified. Young's longitudinal modulus was set to:

$$7 \times 10^9 \text{ Pa} \times (1 + 15.4\%) = 8.078 \times 10^9 \text{ Pa} \tag{6.9}$$

and Young's transverse modulus was increased to 8.078×10^6 Pa.

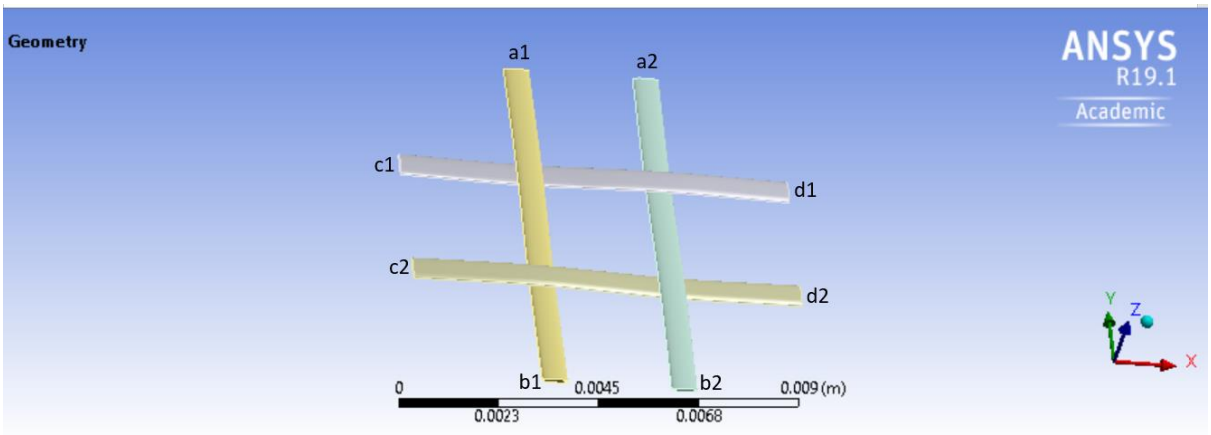

Figure 6.2.7 Geometric model, Case 2

In Figure 6.2.7, the eight yarn ends are labeled a1 to d2. In Case 2, ends a1, a2, b1, b2, c1 and c2 were all fixed. One force of 0.005 N directed towards the positive direction of axis *x* was applied on each of the vertical surfaces at ends d1 and d2, hence the total force applied was 0.01 N.

In Case 2a, the four contact regions were set as frictionless. Displacements along axis *x* are shown in Figure 6.2.8.

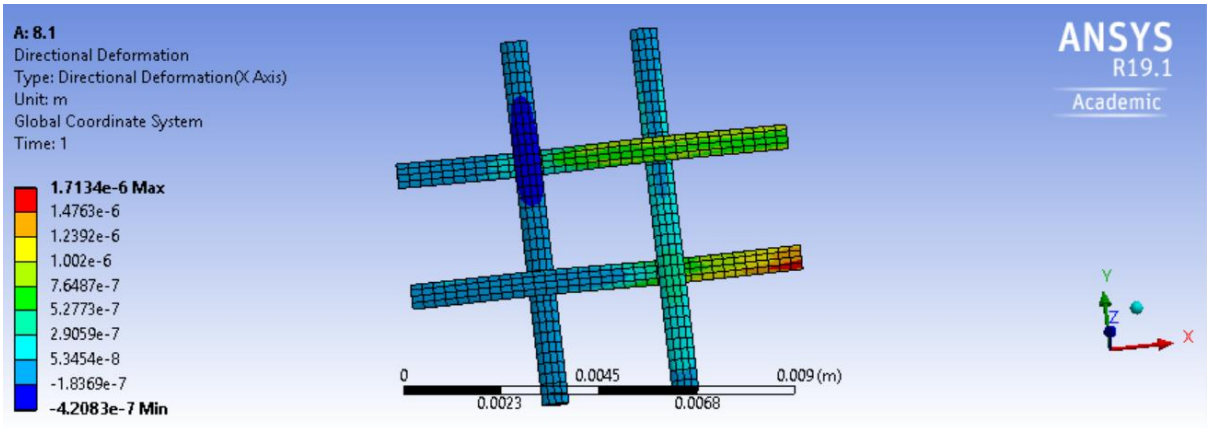

Figure 6.2.8 Displacements along axis *x*, Case 2a

The maximum elongation at ends d1 and d2 was 1.7134×10^{-6} m.

Ignoring the resistance to displacement potentially provided by yarns a1-b1 and a2-b2, and ignoring yarn crimp hence assuming that yarns c1-d1 and c2-d2 are straight, the theoretical elongation is:

$$\delta = \frac{FL}{SE} = \frac{0.01 \times 0.009}{2 \times 5.65 \times 10^{-8} \times 8.078 \times 10^{9}} = 9.9 \times 10^{-8} \qquad (6.10)$$

where δ is the elongation along axis *x*, *F* is the external applied force, *L* is the length of the yarns, S is the yarn cross-section area calculated in Equation 6.1, and *E* is Young's longitudinal modulus of the yarns. The calculated elongation is much smaller than the simulated elongation, by a factor of approximately 17, because in Case 2 the yarns bend. When subjected to forces, the yarns bend and the displacements at the points of application of the forces are primarily from straightening of the yarns, instead of elastic deformation of the yarns under tension. This behaviour is typical of textiles undergoing tension in their plane: their initial stiffness is typically much smaller than the corresponding stiffness of the yarns as yarns straighten. In Case

2a, the stiffness of the model is around 464.86 MPa as calculated using Equations 6.5 to 6.7. The effect of crimp and of the textile structure is observed very clearly.

The total external load was then increased to 0.1N and 1N respectively using the original model, in order to observe the trend in elongation. The results were elongations of 1.5642×10^{-5} m and 1.5036×10^{-6} m respectively. Under the two loads, values of the model stiffness were around 509.20 MPa and 529.72 MPa respectively. It can be seen that under increasingly loads, the tensile stiffness of the model shows a non-linearly increase, as observed under tensile loading for ligament samples 10x, 20x and 30x. In conclusion, Case 2 showed some clear elements of behavior observed in relation to the tensile properties of actual textiles.

In Case 2b, the contact type was set to frictional with a coefficient of friction of 0.3, using the same orthotropic material properties and applied total loads of 0.01 N. Displacements along axis *x* are shown in Figure 6.2.9. The maximum elongation decreased to 1.668×10^{-6} m. This result is reasonable, as friction between warp and weft yarns restricts the deformation of yarns c1-d1 and c2-d2. In this case, and unlike for Case 1, the application of tensile forces on the yarns does induce normal loads at the contacts, as a result of yarn interlacing.

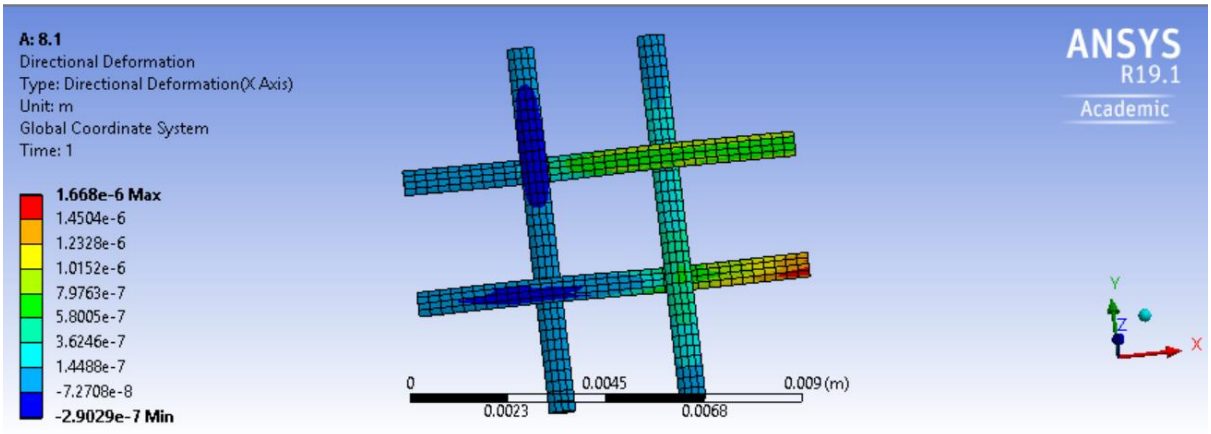

Figure 6.2.9 Elongation along axis *x*, Case 2b

In Case 2c, the contact type was set to 'bonded', using the same orthotropic material and applied total load of 0.01 N. As expected, the maximum elongation further decreased to 1.4759 $\times 10^{-6}$ m, and yarns a1-b1 and a2-b2 deformed more than they did in Cases 2a and 2b.

6.2.3 Case 3

The model used in Case 3 is a repeating unit cell of series 10x, the geometry of which is shown in Figure 6.2.10. It consists of three warp yarns and six weft yarns divided into two groups. In Figure 6.2.10, each yarn end is labeled a1 to d3. The distance between two adjacent sides of two adjacent yarns is 0.12 mm, which is the minimum distance to prevent one yarn from going through another. The distance between weft yarn a3-b3 in the left group and a4-b4 in the right group is 1 mm, which mimics openings in the textile. Yarn cross-sections are identical to those in Case 1 and Case 2, with the same radii. Thus, the warp yarns are 6.08 mm long in total and the weft yarns are 3 mm long. The same orthotropic material properties with Young's moduli of 8.078×10^9 Pa along the yarns and 8.078×10^6 Pa across the yarns were also used.

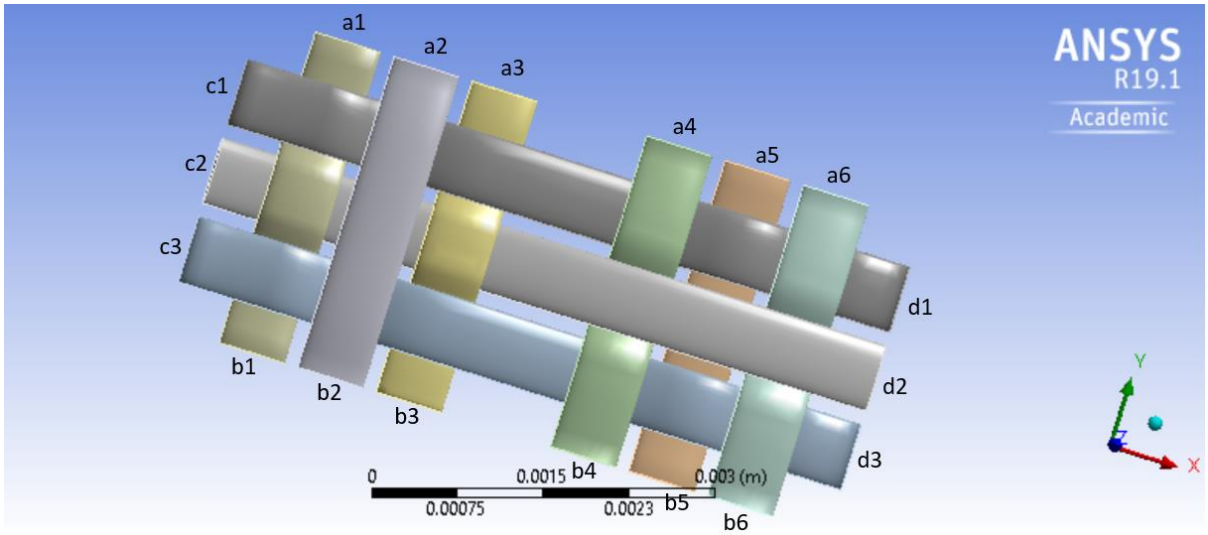

Figure 6.2.10 Geometric model, Case 3

In Case 3, ends a1 to a6 and b1 to b6 are fixed along axis *y* and *z*, while free along axis *x*, which mimics the behaviour of the textile under tensile loads. Under the same consideration, ends c1 to c3 are fixed along axis *x* while free along axis *y* and *z* because shrink may occurs on the three warp yarns when pulling. A total load of 0.01 N along axis *x* was applied, equally separated to the vertical surfaces of ends d1 to d3, all of which can only deform along axis *x*.

In Case 3a, all of the contact regions are set as frictional with a coefficient of friction of 0.3. Displacements along axis *x* are shown in Figure 6.2.11.

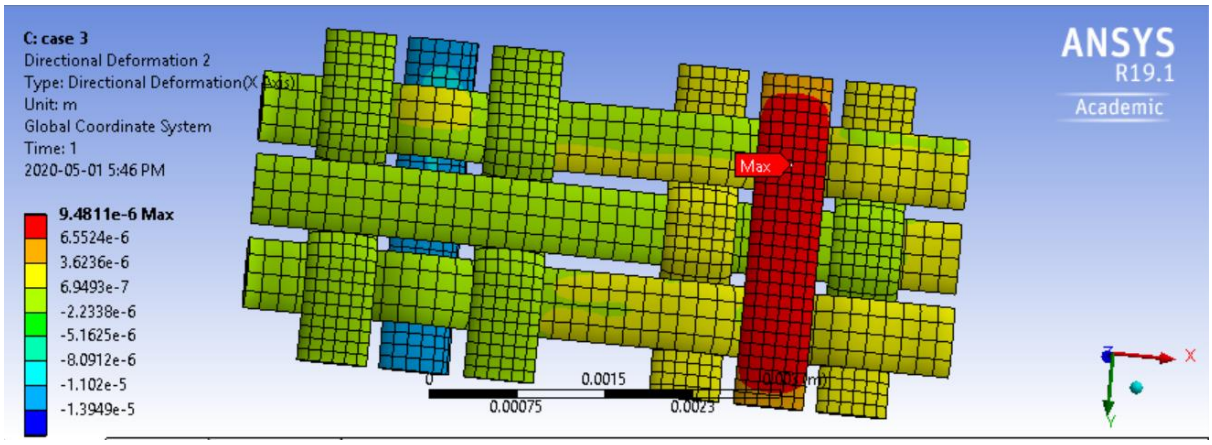

Figure 6.2.11 Displacements along axis *x*, Case 3a

The green and yellow parts mean that these yarns have similar deformation within a range of -2.23×10^{-6} m to 3.62×10^{-6} m. However, yarn a2-b2 and a4-b4 show unreasonable deformation much greater than others. This unreasonable result is considered as a model error. In a repeating unit cell, yarn a2-b2 and a4-b4 are attached above or below the three warp yarns that provide no restriction along any direction. As a result, the software cannot analyse the deformation of the two yarns because of the lack of a restriction or boundary condition.

In Case 3b, the contact type was set to frictionless, applying the same material properties and loads. Results for displacement along axis *x* also show a similar error, because of the same reason.

In Case 3c, the contact type was set to bonded. Material properties, supports and loads are same as Case 3a and 3b. Displacements along axis *x* are shown in Figure 6.2.12.

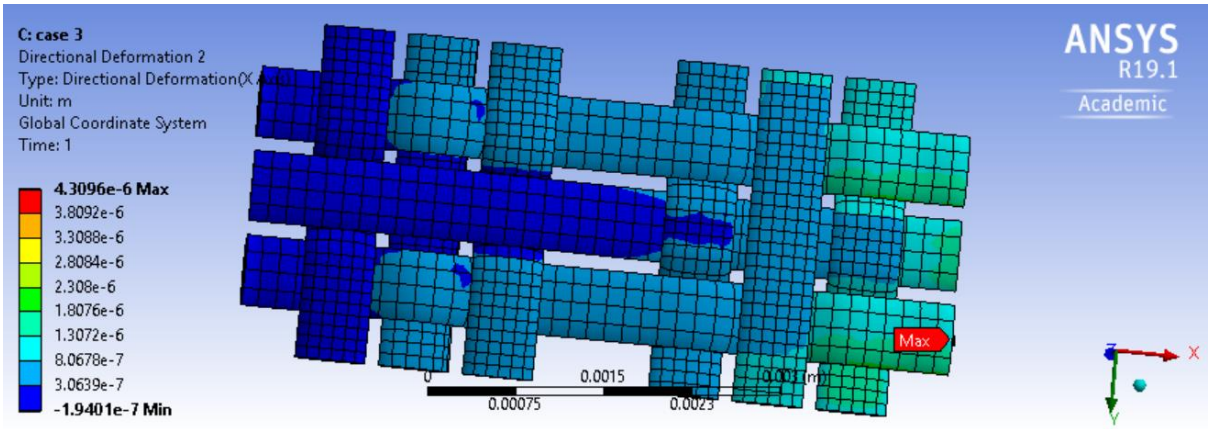

Figure 6.2.12 Displacements along axis *x*, Case 3c

In Figure 6.2.12, the displacements of yarn a2-b2 and a4-b4 are reasonable and the maximum displacement occurs on the rightmost element. That is because the two yarns are bonded to the three warp yarns at their contacts, hence their displacements are restricted by the three warp yarns.

6.2.4 Case 4

In Case 3, ANSYS gave reasonable results only when contact regions were set to bonded. However, in real condition, warp and weft yarns are not bonded but they can slide under tensile loads. In order to better represent the tensile behaviour of the sample, Case 4 was constructed using the same geometry model as Case 3 shown in Figure 6.2.10. The same orthotropic material properties with Young's moduli of 8.078×10^9 Pa along the yarns and 8.078×10^6 Pa across the yarns were also used. The same 0.01 N total tensile load was applied on ends d1 to d3. What differed from Case 3 is that in Case 4, ends a1 to a6 and b1 to b6 are fixed. Except for that, boundary conditions for ends c1 to c3 and d1 to d3 are same as that of Case 3. The

contact regions are set as 'frictional' with a coefficient of friction of 0.3. Displacements along axis *x* are shown in Figure 6.2.13.

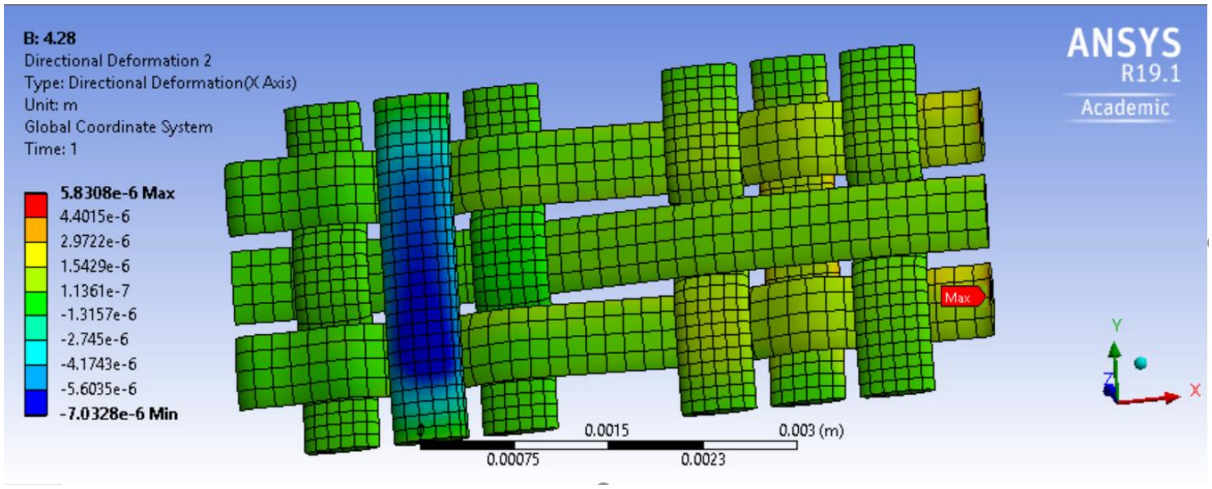

Figure 6.2.13 Displacements along axis *x*, Case 4

In Figure 6.2.13, the maximum elongation occurs on the ends d1 and d3 with a value of 5.8308 $\times 10^{-6}$ mm. Apart from that, the center of yarn a2-b2 also moves significantly along axis *x*, because of rotation. The same type of rotation occurs with yarn a4-b4, on the opposite side of the model. Compared with Case 3a, the results of Case 4 are more reasonable.

According to Equation 6.5 to 6.8, tensile stiffness for case 4 is around 184.46 MPa under a load of 0.01N. The total external load was then increased to 0.1N and 0.5N respectively using the same model, in order to observe the trend in elongation. The results were elongations of 4.4168 $\times 10^{-5}$ m and 2.2006$\times 10^{-4}$ m respectively. Under the two loads, values of the model stiffness were around 243.66 MPa and 244.4 MPa respectively. As seen with Case 2 and observed with samples 10x, 20x and 30x, the tensile stiffness for Case 4 shows non-linear increase under increasing loads.

Although the non-linear increase in tensile stiffness shows tensile behavior that is typical of textile samples, the values are much smaller than those presented in Chapter 4. In Chapter 4, the tensile stiffness for series 10x was around 800 MPa, 1100 MPa and 1300 MPa under stress values of 1.2 MPa. 2.4 MPa and 3.6 MPa respectively, while the maximum tensile stiffness for Case 4 was 244.4 MPa. As a comparison of stiffness under similar loading conditions, when applying a 0.5 N total tensile load, the equivalent stress is:

$$\sigma = \frac{F}{A} = \frac{0.5N}{3 \times 0.0565mm^2} = 2.95MPa \tag{6.11}$$

where 0.0565 mm^2 is the cross-section area of one single yarn in this case. Thus, under a similar level of tensile stress, the tensile stiffness values observed from experimental results were around 5 times higher than that of the model. Reasons for such discrepancy could be explained in a number of ways. Firstly, the model constructed is probably not sufficiently accurate or intricate. The yarns are constructed as uniform solid bars with the same shape of cross-section everywhere along their length. In order to ensure there is enough room for these solid bars to form a weave pattern, yarns in the model are more bent than they are in real conditions. Furthermore, real yarns consist of numerous independent fibres that touch each other at numerous discrete points; yarns under tension will follow a straight path between crossovers, and the cross-sections of these yarns can deform due to compaction. Thus, yarns in real textiles are more compact and straighter, and they will deform less form an initial, artificially bent shape compared with the models. Figure 6.2.14 shows deformation along axis *z* under 0.01N, which is the thickness direction of the model. The maximum elongation is 2.9338×10^{-5} mm.

Compared with the maximum elongation along axis *x*, this value is high, which means the straightening or 'unbending' behaviour of the yarns contributes the most elongation along axis *x*.

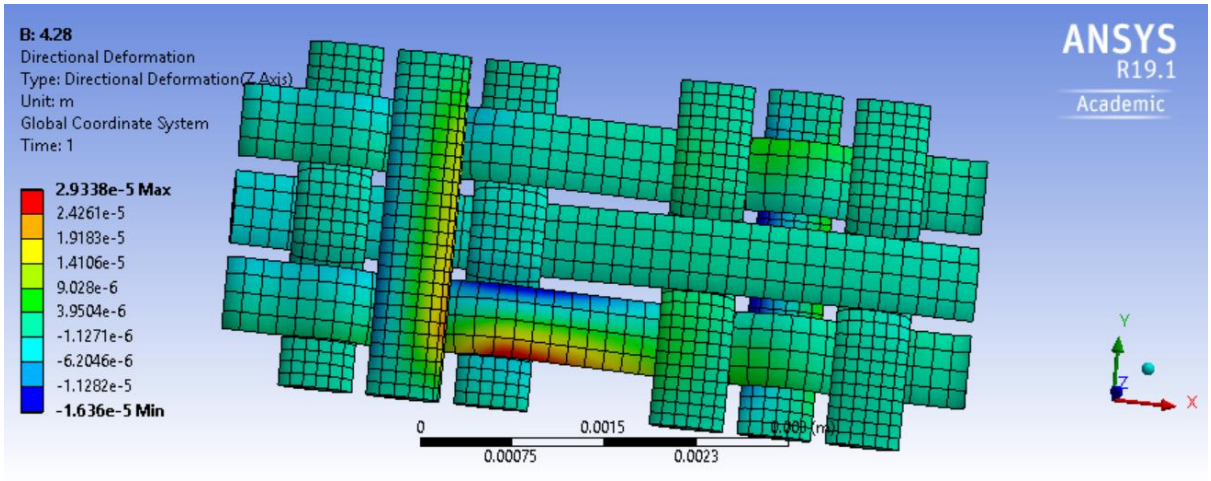

Figure 6.2.14 Displacements along axis *z*, Case 4

Chapter 7 - Conclusions

The main goals of this thesis were to assess the mechanical behaviour of three types of artificial implantable textile ligaments, as well as simulating tensile behaviour using finite element analysis. All objectives listed in Section 1.2 were achieved:

- Tensile and in-plane shear properties of the three kinds of samples were measured;
- Tensile and in-plane shear stiffness under different loads were calculated;
- Mechanical properties of the three samples were analysed and compared with those of real knee ligaments;
- Geometric models of the samples were created in TexGen;
- Geometric models of the samples were subjected to loads in ANSYS, and analysis of stresses, strains and deformations were conducted;
- Results from the models were analysed and compared with experimental results.

Investigation of tensile and shear behaviour of the three samples is detailed. The stress-strain curves for tensile and in-plane shear show features of both PET fibres and textiles. Among many features, stiffness increases with stress, which is the same as biological ligaments subjected to relatively low levels of stress. Thus, the samples can replicate the mechanical behaviour of real ligaments in human bodies. Besides, tensile stiffness values for the samples are much higher than those of real knee ligaments. Considering that stiffness of the whole structure will experience a decrease when the in vivo cell ingrowth is considered and the section

of the resulting implanted structure is significantly increased accordingly; the samples can sustain loading without being too stiff for use in human bodies.

The tensile and in-plane shear results for the three samples differ significantly, indicating that the interlacing patterns influence the mechanical properties dramatically. For tensile results, sample series 20x showed the highest tensile stiffness at around 2500 MPa, while sample series 30x shows the lowest tensile stiffness at around 550 MPa under same tensile load. This large difference was the result of two reasons. One is differences in weave patterns, as mentioned previously. The other arises as although stiffness values were calculated under the same load levels, stress levels in the three samples were different. In addition, stress-strain curves for samples 30x were more linear than they were for the other two samples because of its dense woven structure. For shear results, samples 30x showed the highest in-plane shear stiffness at around 8 N/degree, while samples 10x shows the lowest in-plane shear stiffness at around 1.9 N/degree under same shear load. Among many factors, density is the most important factor that influence in-plane shear stiffness.

In terms of modeling, a series of successes were achieved. Simulation models that replicates geometric relations were successfully created using TexGen. As for FEA results, ANSYS performed reasonable calculations for simple models, including stresses, strains and deformations for models constructed using both isotropic and orthotropic materials. Though relatively coarse meshes caused moderate error compared with theoretical results, this was contained successfully. It should also be noted that whilst the models only featured repeating

unit cells, the presence of slightly different textile structures and interlacing patterns on the edge of physical samples may have contributed to some of the differences observed between results obtained from simulations and experiments.

In conclusion, the modeling process and analysis of mechanical properties of simple textile models was introduced and achieved some level of success in this thesis. The FEA results for complex models are not wholly satisfying, and additional work will be required in terms of their development; this work also require better resources and more time than those available with the context of this work, where the modeling was exploratory and only a part of the overall objective. Calculated tensile stiffness values for the model which simulated sample series 10x were much lower than the experimental results. It was demonstrated that using solid yarns coupled with off-the-shelf material models available in the software for representing flexible yarns is not accurate. In real textiles, yarns compact with each other and deform, causing the yarns to flatten or narrow very markedly. These types of deformations could not be simulated to a sufficient extent using solid yarns in ANSYS. As a result, differences in the structures of models and real textiles resulted in the inaccuracy of models and calculated tensile stiffness values. On the other hand, a number of trends could be replicated successfully, at least in part.

Based on above, future work should focus on how to create more realistic textile models. More attention should be paid to make yarns the more deformable that replicates the local compaction behaviour of yarns and textiles better. If possible, introducing more repeating unit cells and modeling weave patterns on the edges of the textiles would also increase accuracy.

References

[1] M. O. H. Cioffi, H.J.C. Voorwald and R. P. Mota, Surface energy increase of oxygen-plasma-treated PET. *Materials Characterization.* pp. 209-215, March 2003.

[2] L. Ambrosio, R. D. Santis and L. Nicolais. Proceedings of the Institution of Mechanical Engineers, Part H: Journal of Engineering in Medicine. *Composite hydrogels for implants.* vol. 212, no. 2, pp. 93-99, February 1998.

[3] S. Sahoo, J. G. Cho-Hong and T. Siew-Lok. Development of hybrid polymer scaffolds for potential applications in ligament and tendon tissue engineering. *Biomed. Mater.* vol. 2, pp. 169-173, 2007.

[4] J. A. Cooper, H. Lu, F. K. Ko J. W. Freeman, Cato T. Laurencin. Fiber-based tissue-engineered scaffold for ligament replacement: design considerations and in vitro evaluation. *Biomaterials*. vol. 26, pp. 1523-1532, 2005.

[5] S. Kawabata, M. Inoue, and M. Niwa. Non-linear Theory of the Biaxial Deformation of a Triaxial-weave Fabric. *Journal of the Textile Institute.* vol. 1, pp. 104-119, 1992.

[6] S. Salehi, M. Kharaziha, N. Masoumi, A. Fallahi and A. Tamayol. (2017). *Textile finishing: Recent developments and future trends.* Hopewell Jct., NY: Wiley Blackwell.

[7] The basic structures of woven fabrics – plain weave, twill weave, and satin weave. [Online]. Available: https://m.sxqiyu.com/news/the-basic-structures-of-woven-fabrics-plain-weave-twill-weave-and-satin-weave

[8] M. Akbari, A. Tamayol, S. Bagherifard, L. Serex, P. Mostafalu, N. Faramarzi, M. H. Mohammadi and A. Khademhosseini. Textile technologies and tissue engineering: A path toward organ weaving. *Advanced Healthcare Materials.* vol. 5, no, 7, pp. 751-766, May 2016.

[9] M. Akbari, A. Tamayol, V. Laforte, N. Annabi, A. H. Najafabadi, A. Khademhosseini and D. Juncker. Composite living fibers for creating tissue constructs using textile techniques. *Adv. Funct. Mater.* pp. 4060-4067, 2014.

[10] A. Tamayol, M. Akbari, N. Annabi, A. Paul, A. Khademhosseini and D. Juncker. Fiber-based tissue engineering: Progress, challenges, and opportunities. *Biotechnology Advances*. vol. 31, pp. 669-687, 2013.

[11] F.T. Moutos, L.E. Freed and F. Guilak, A biomimetic three-dimensional woven composite scaffold for functional tissue engineering of cartilage. *Nat. Mater.* pp. 162-167, June 2007.

[12] A.F.D.P. Freitasa, M.D. de Araujoa, W.W. Zub and R.M.E. Fangueiroa. Development of weft-knitted and braided polypropylene stents for arterial implant. *The journal of the textile institute.* vol. 101, no. 12, pp. 1027-1034, December 2010.

[13] R. Kamiya, A. B. Cheeseman and T.Chou. Some recent advances in the fabrication and design of three-dimensional textile preforms: a review. *Composites Science and Technology.* vol. 60, pp. 33-47, January 2000.

[14] S. Kannan and M.S. Kumaravel, A comprehensive look at 3-D fabrics. *Journal of the Textile Association.* vol. 66, no. 1, pp. 35-40, 2005.

[15] S. S. Roy and P. Potluri. Braiding: From Cordage to Composites. *Textile Research Conference.* 2016.

[16] M. Grolms. Silicone Rubber Knee. *Advanced science news.* July 2015.

[17] A. Liberski, N. Ayad, D. Wojciechowska and D. M. Zielińska. ReasearchGate. Knitting for heart valve tissue engineering. *Global Cardiology Science and Practice.* December 2016.

[18] T. Cheng, X. Yan and L. Wang. A kind of extracellular matrix scaffold material and preparation method thereof. China. October 2012.

[19] F. Alam, V.R. Shukla, K.M. Varadarajan and S. Kumar. Microarchitected 3D printed polylactic acid (PLA) nanocomposite scaffolds for biomedical applications. *Journal of the Mechanical Behavior of Biomedical Materials.* vol. 103, March 2020.

[20] S. S. Liao, F. Z. Cui, W. Zhang and Q. L. Feng. Hierarchically biomimetic bone scaffold materials: Nano-HA/collagen/PLA composite. *Journal of Biomedical materials research.* vol. 69, no. 2, pp. 158-165, 2004

[21] L. Zhao, C. He and L. Cui. The Influence of Copolymer Compositions on the Physiochemical and Biological Properties of Poly (Lactic-co-Glycolic Acid) Porous Scaffolds. *Journal of Biomimetics, Biomaterials and Tissue Engineering.* vol. 6, no. 1, pp.35-44, September 2010.

[22] G. Li ,Y. Li , G Chen, J He, Y Han, X Wang and D. L. Kaplan. Silk-based biomaterials in biomedical textiles and fiber-based implants. *Advanced Healthcare Materials.* vol.4, no. 8, pp. 1134-1151, June 2015.

[23] B. Chevallay, D. Herbage. Collagen-based biomaterials as 3D scaffold for cell cultures: applications for tissue engineering and gene therapy. *Medical and Biological Engineering and Computing.* vol. 38, no. 2, pp.211-218, March 2000.

[24] D Zhang, X Wu, J Chen and K Lin. The development of collagen based composite scaffolds for bone regeneration. *Bioactive Materials.* pp. 129-138, March 2018.

[25] A. Sensini and L. Cristofolini. Biofabrication of Electrospun Scaffolds for the Regeneration of Tendons and Ligaments. *Materials.* October 2018.

[26] Y. Gloy, M. Loehrer, B. Lang, L. Rongen, T. Gries and S. Jockenhoevel. Tubular Woven Narrow Fabrics for Replacement of Cruciate Ligaments. *Annals of Biomedical Engineering.* vol. 41, no. 9, pp. 1950-1956, September 2013.

[27] S. Marzougui, S.B. Abdessalem and F. Sakli. Viscoelastic behavior of textile artificial ligaments. *Journal of Applied Sciences.* vol. 9, no. 15, pp. 2794-2800, 2009.

[28] T.J.A. Mommersteeg, L. Blankevoort, R. Huiskes, J.G.M. Kooloos and J.M.G. Kauer. Characterization of the mechanical behavior of human knee ligaments: A numerical-experimental approach. *Journal of Biomechanics.* vol. 29, no. 2, pp. 151-160, February 1996.

[29] K. Smeets, J. Slane, L. Scheys, S. Claes, J. Bellemans, Mechanical Analysis of Extra-Articular Knee Ligaments. Part One: Native knee ligaments. The Knee. vol. 24, no. 5, pp. 949-956, 2017.

[30] A. J. Weiss, J. C. Gardiner and C. Bonifasi-Lista. Ligament material behavior is nonlinear, viscoelastic and rate-independent under shear loading. *Journal of Biomechanics.* vol. 35, pp. 943–950, February 2002.

[31] A. Ristaniemi, L. Stenroth, S. Mikkonen and R.K. Korhonen. Comparison of elastic, viscoelastic and failure tensile material propertiesof knee ligaments and patellar tendon. *Journal of Biomechanics.* vol. 79, pp:31-38, October 2018.

[32] K. L. Billiar and M. S. Sacks. Biaxial Mechanical Properties of the Natural and Glutaraldehyde Treated Aortic Valve Cusp—Part I: Experimental Results. *Journal of Biomechanical Engineering.* vol. 122, no. 1, pp. 23-30, February 2000.

[33] S. H. Alavi, V. Ruiz, T. Krasieva, E. L. Botvinick and A. Kheradvar. Characterizing the collagen fiber orientation in pericardial leaflets under mechanical loading conditions. *Annals of Biomedical Engineering.* vol. 41, no. 3, pp. 547-561, March 2013.

[34] J. A. Stella and M. S. Sacks. On the Biaxial Mechanical Properties of the Layers of the Aortic Valve Leaflet. *J Biomech Eng.* pp. 757-766, February 2007.

[35] C. K. Breuer, T. Shin'oka, R. E. Tane, G. Zund, D. J. Mooney, P. X. Ma, T. Miura, S. Colan, R. Langer, J. E. Mayer and J. P. Vacant. Tissue engineering lamb heart valve leaflets. *Biotechnology and Bioengineering.* vol. 50, pp. 562-567, 1996.

[36] A. F. Quigley, K. J. Bulluss, I. L. B. Kyratzis, K. Gilmore1, T. Mysore, K. S. U. Schirmer, E. L. Kennedy, M. O'Shea, Y. B. Truong and S L Edwards. Engineering a multimodal nerve conduit for repair of injured peripheral nerve. *Neural Eng.* pp. 1741-2560, 2013.

[37] X. Li, Y Yang, Y. Fan, Q. Feng, F. Cui and Fumio Watari. Biocomposites reinforced by fibers or tubes as scaffolds for tissue engineering or regenerative medicine. *Journal of Biomedical Materials Research - Part A.* vol. 102. no.5, pp. 1580-1594, May 2014.

[38] S. Ichihara, Y. Inada, A. Nakada, K. Endo, T. Azuma and R. Nakai. Development of new nerve guide tube for repair of long nerve defects. *Tissue Engineering.* pp. 387-402, 2009.

[39] I. C. Liao, F. T. Moutos, B.T. Estes, X. Zhao and F. Guilak. Composite three-dimensional woven scaffolds with interpenetrating network hydrogels to create functional synthetic articular cartilage. *Advanced Functional Materials.* vol. 23, pp. 5833-5839, 2013.

[40] M. Arjmandi, M. Ramezani, T. Bolle, G. Köppe, T. Gries and T. Neitzert. Mechanical and tribological properties of a novel hydrogel composite reinforced by three-dimensional woven textiles as a functional synthetic cartilage part A: Applied science and manufacturing. *Composites.* pp. 123-133, December 2018.

[41] W. Dai, N. Kawazoe, X. Lin, J. Dong and G. Chen. The influence of structural design of PLGA/collagen hybrid scaffolds in cartilage tissue engineering. *Biomaterials.* vol. 31, pp. 2141-2152, 2010.

[42] F. Han, S. Liu, X. Liu, Y. Pei, S. Bai, H. Zhao, Q. Lu, F. Ma, D.L. Kaplan and H. Zhu. Woven silk fabric-reinforced silk nanofibrous scaffolds for regenerating load-bearing soft tissues. *Acta Biomaterialia.* vol. 10, no. 2, pp. 921-930, February 2014.

[43] C. Lou, J. Hu, Y. Chen, S. Wen, K. Lin, and J. Lin. Manufacturing Technology of 316L Stainless Steel/Poly(Lactic Acid) Composite Braids and the Induction of Hydroxyapatite Formation on the Braid. *Advanced Materials Research.* vol. 287-290, pp. 2669-2672, 2011.

[44] X. Wang, Q. Li, X. Hu, L. Ma, C. You, Y. Zheng, H. Sun, C. Han and C. Gao. The influence of structural design of PLGA/collagen hybrid scaffolds in cartilage tissue engineering. *Journal of the Mechanical Behavior of Biomedical Materials*.vol. 8, pp. 204-215, 2012.

[45] B. Rentsch, A. Hofmann, A. Breier, C. Rentsch and D. Scharnweber. Embroidered and surface modified polycaprolactone-co-lactide scaffolds as bone substitute: In vitro characterization. *Annals of Biomedical Engineering.* pp. 2118-2128, October 2009.

[46] Standard Test Method for Breaking Strength and Elongation of Textile Fabrics (Grab Test)1

[47] Jawwad Akbari. Querying the Material Properties of Synthetic Medical Soft Tissue Scaffolds. December 2018.

[48] M Biron. (2007). *Thermoplastics and Thermoplastic Composites.* Burlington: Elsevier Ltd.

[49] S. Fakirov. (2002). *Handbook of Thermoplastic Polyesters.* Weinheim: Wiley-VCH.

[50] C. C. Ibeh. (2011). *Thermoplastic materials: properties, manufacturing methods and applicaions.* Florida: CRC Press.

[51] P. B. Rim and C. J. Nelson. Properties of PET fibers with high modulus and low shrinkage (HMLS). I. Yarn properties and morphology. *Journal of Applied Polymer Science.* vol. 42, pp. 1807-1813, April 1991.

[52] T. Kunugi, A. Suzuki and M. Hashimoto. Mechanical properties and superstructure of high-modulus and high-strength PET fiber prepared by zone annealing. *Journal of Applied Polymer Science.* vol. 26, pp. 1951-1960, June 1981.

[53] T. Drivas. Manufacturing Three-dimensional Carbon-fibre Preforms for Aerospace Composites. 2014.

[54] F. Robitaille and R. Gauvin. Compaction of Textile Reinforcements for Composites Manufacturing. 111: Reorganization of the Fiber Network. *Polymer Composites.* vol. 20, no.1, February 1999.

[55] TexGen 3. 10. 0. December 2017. https://sourceforge.net/projects/texgen/#.

[56] ANSYS Workbench 19.1. April 2018. University of Ottawa, Canada. 2325@ansys.genie.uottawa.ca.

[57] F. Robitaille and R. Gauvin, Compaction of textile reinforcements for composites manufacturing. I: Review of experimental results. *Polymer Composites*. vol.19, no. 2, pp. 198-216, 1998